UNIVERSITY OF CALIFORNIA

Los Angeles

Ξ Hyperon Photoproduction from Threshold to 5.4 GeV with the CEBAF Large Acceptance Spectrometer

A dissertation submitted in partial satisfaction of the requirements for the degree Doctor of Philosophy in Physics

by

John Theodore Goetz

2010

The dissertation of John Theodore Goetz is approved.

James Ralston

David Saltzberg

Bernard M. K. Nefkens, Committee Chair

University of California, Los Angeles

2010

*This dissertation is dedicated to my wife Katherine,
who has been a constant source
of love, support and encouragement.*

Contents

List of Figures

List of Tables

ACKNOWLEDGMENTS

This dissertation is the product of a collaboration. Though only my name appears on the title page, this work would not be possible without the tireless effort put forth by the *g12* run-group at Jefferson Laboratory, which includes Drs. Paul Eugenio, Valery Kubarovsky, John Price and Dennis Weygand, as well as the exceptionally hard working graduate students: Craig Bookwalter, Mukesh Saini and Diane Schott. Major contributions to the calibration, simulation and analysis of the data presented in this work were also provided by Drs. Lei Guo, Mike Paolone, Carlos Salgado and Burnham Stokes. I would like to express my heart-felt gratitude to each of these individuals.

The largest influence I received throughout the years came from my excellent adviser, Prof. Bernard M.K. Nefkens, who guided my work toward a sound theoretical motivation and kept many aspects of my labor meaningful and timely. His support and patience helped me wade through deep and sometimes troubled waters to finish this dissertation. I am especially grateful to him for the many discussions that helped to improve the technical details of my work. I would like to thank Prof. Nefkens along with the Department of Energy for funding this research into the nature of particle interactions.

Over the course of my membership in the `CLAS` collaboration and involvement in the *g12* experiment I spent several months at the laboratory in Virginia. Throughout this time, Dr. Dennis Weygand provided me with invaluable guidance both in the details of analysis with `CLAS` and its physical interpretation. He has taught me most of what I know about programming which has culminated in over 45,000 lines of my own code, making up the core of my analysis. I am indebted to him for all the effort he put forth throughout my entire graduate career.

The previous work that motivated the cascade analysis for the *g12* experiment was conducted by Prof. John Price. As a post-doc at `UCLA` working with Prof. Nefkens, he introduced me to the `CLAS` collaboration and scientific environment at Jefferson Lab. I would like to express my deepest gratitude for his patience and understanding from a time when I was struggling to use the Linux operating system to when I helped him set up his computing farm at California State University Dominguez Hills.

Of the many people that worked with the `CLAS` detector, I would like to specifically thank Drs. Eugene Pasyuk, Stepan Stepanyan and Sergey Boyarinov. They were a constant source of knowledge on this extremely complex system, and their expertise was invaluable to the *g12* run-group as a whole. Dr. Stepanyan acted as the Physics Division Liaison (`PDL`) during the entire three months of running and spent many hours in the experimental hall making sure the detector and accelerator were working properly. In addition, Dr. Boyarinov's incomparable work on the data acquisition system allowed the experiment to run at an unprecedented rate. Finally, Dr. Pasyuk's guidance on everything from start-counter calibrations to event simulation was fundamental to our success. Furthermore, I would like to acknowledge all the members of the `CLAS` collaboration and the CEBAF accelerator group for keeping this sophisticated system operational and working so smoothly.

When we were ready to start processing the raw data, we were severely limited by computing resources at Jefferson Lab. The initial estimates put us at one year of running on the computing farm at full capacity. At this time, the computing center worked very hard, and very successfully, to increase the capacity of the farm allowing us to complete the reconstruction in just four months. I would like to thank the whole scientific computing group at JLab, and specifically Sandy Philpott and Michael Barnes for meeting with Dr. Weygand and me repeatedly as we worked out the kinks in switching the farm's architecture from 32-bit to 64-bit.

My fellow graduate students in the *g12* run-group, Craig Bookwalter, Mukesh Saini and Diane Schott, and then-recent post-doc Dr. Michael Paolone, became close friends of mine during the time I spent in Virginia. I know we have made life-long connections between each other and I personally cannot thank them enough for helping me keep sane through the years. Their expertise and professionalism has always been phenomenal and I would not have been able to accomplish all I have without them.

At UCLA, I worked beside Drs. Alexandr Starostin and Serguei Prakhov who were involved with the Crystal Ball experiment in Mainz, Germany. They provided me with fresh ideas and insightful critiques on the technical aspects of my analysis. I also had the pleasure of working with several fellow students who helped me in various aspects of this work. My office-mate before the *g12* experiment took place, Jason Brudvik, obtained his PhD. in 2007. He helped me come to grips with CERN's analysis framework: ROOT, and we had many discussions concerning computers and physics over the years. During this time, Indara Suarez, who is now in the graduate physics program at Texas A&M, helped me maintain the computing cluster I had set up for our group's Crystal Ball analyses. This cluster was later used for my final analysis of the cascades and iso-exotics with CLAS. As Indara became more involved with the Crystal Ball collaboration, we hired Chris Cesare who did an excellent job in keeping up with the increasing demands we put on our computers. In the last several months of my work on this dissertation, Sriteja Upadhyayula took over for Chris and assisted me in verifying the details of the results presented. I am thankful for each of these coworkers who all became good friends of mine and I only hope to work with people of the same caliber in my future career.

The friendships I have had outside the physics environment were crucial for my success, and I would like to thank my best-man Bryant Vo for always being a great friend since junior high school. I would also like to acknowledge Travis Purdy who I met as an undergraduate. We became close friends and shared an apartment in my first year of graduate school with several others including my fellow trombone player at UCLA, Clay McCarter. It was in that apartment complex where we went to a Christmas party hosted by the girls that lived below us, and this is where I met my wife Katherine for the first time. During these years, Katherine and I spent many memorable days with our friends, including Justin Casalegno, John Swartz and Chris Messett. We also have extremely fond memories visiting Travis' family in beautiful Solvang. In the last year of writing this dissertation, I played banjo in the Old-Time String Band at UCLA and met my fellow banjo player, Robert Denomme. We were fast friends and he, along with Bailey Scott, helped me survive in Los Angeles while Katherine was working for the city of Norfolk, Virginia. We spent many stress-relieving nights playing Euchre and Whist with Brian Leary and I would like to express my deepest gratitude for their friendship. Each of these people were indispensable to me and I hope that the connections we have made will endure for many years to come.

To my loving and encouraging family, I owe more than can I say. The support I received from my sister and brother-in-law, Mary and John Baum, was greatly appreciated, and I look forward to spending time with my brand new nephew John Henry! I would like to thank my parents, John and Linda Goetz, who provided a level of effort and assistance that helped make this work something of which I can be exceedingly proud. Their detailed notes through several drafts were invaluable and their continued commitment to my life and my well-being is something I cherish to no end. Finally, my wife Katherine, to whom this work is dedicated, has been my true inspiration and greatest joy since we first met. I cannot imagine life without her and I love her dearly.

VITA

1980	**Born July 27th**	Walnut Creek, CA
1995–1997	**Sales Clerk** Long's Drug Store	Yorba Linda, CA
1995–1999	**Diploma, High School**	
	Monte Vista HS (*1998–9*)	San Ramon, CA
	San Ramon HS (*1997–8*)	San Ramon, CA
	Esperanza HS (*1995–7*)	Anaheim, CA
1997–1998	**Inside Sales Associate** Kelly Moore Paints	San Ramon, CA
1999	**Inventory Management** Office Depot, Inc.	Dublin, CA
1999–2004	**B.S. Physics** `UCLA` Dept. of Physics & Astronomy	Los Angeles, CA
2000	**Librarian** East Asian Coll., UCLA Library	Los Angeles, CA
2002	**Control System Development** `WASA/TSL`	Uppsala, Sweden
2003	**Spheromak Research** `LLNL`	Livermore, CA
2005–2007	**Teaching Assistant** `UCLA` Dept. of Physics & Astronomy	Los Angeles, CA

2007 **Private Pilot Certification** Santa Monica, CA
American Flyers — Single Engine Land
Complex Endorsement Newport News, VA

PUBLICATIONS AND PRESENTATIONS

J. T. Goetz et al. Using controlled magnetic perturbations to study the plasma confinement in a spheromak. *Bull. Am. Phys. Soc.*, 48:150, 2003. Poster at APS meeting

J. W. Price et al. Exclusive photoproduction of the cascade (Ξ) hyperons. *Phys. Rev. C*, 71:058201, 2005

L. Morand, M. Garçon, et al. Deeply virtual and exclusive electroproduction of ω mesons. *Eur. Phys. J. A*, 24:445, 2005

K. Joo, L. C. Smith, et al. Measurement of the polarized structure function $\sigma_{LT'}$ for pion electroproduction in the roper resonance region. *Phys. Rev. C*, 72:058202, 2005

M. Osipenko et al. Measurement of the deuteron structure function F_2 in the resonance region and evaluation of its moments. *Phys. Rev. C*, 73:045205, 2006

S. Strauch et al. Beam-helicity asymmetries in double-charged-pion photoproduction on the proton. *Phys. Rev. Lett.*, 95:162003, 2006

A. Klimenko, S. Kuhn, et al. Electron electron scattering from high-momentum neutrons in deuterium. *Phys. Rev. C*, 73:035212, 2006

K. Egiyan et al. Measurement of 2- and 3-nucleon short range correlation probabilities in nuclei. *Phys. Rev. Lett.*, 96:082501, 2006

M. Battaglieri, R. De Vita, V. Kubarovsky, et al. Search for $\Theta^+(1540)$ pentaquark in high statistics measurement of $\gamma p \rightarrow \overline{K}^0 K^+ n$ at clas. *Phys. Rev. Lett.*, 96:042001, 2006

M. Dugger, B. Ritchie, et al. η' photoproduction on the proton for photon energies from 1.527 to 2.227 GeV. *Phys. Rev. Lett.*, 96:062001, 2006

R. Bradford, R. Schumacher, et al. Differential cross sections for $\gamma\ p \rightarrow K^+\ Y$ for Λ and Σ^0 hyperons. *Phys. Rev. C*, 73:035202, 2006

H. Egiyan, V. Burkert, et al. Single π^+ electroproduction on the proton in the first and second resonance regions at 0.25 GeV$^2 < Q^2 <$ 0.65 GeV^2 using `CLAS`. *Phys. Rev. C*, 73:025204, 2006

B. McKinnon, K. Hicks, et al. Search for the Θ^+ pentaquark in the reaction $\gamma d \to pK^-K^+n$. *Pys. Rev. Lett.*, 96:212001, 2006

S. Niccolai, M. Mirazita, P. Rossi, et al. Search for the Θ^+ pentaquark in the $\gamma d \to \Lambda nK^+$ reaction measured with CLAS. *Pys. Rev. Lett.*, 97:032001, 2006

V. Kubarovsky, P. Stoler, et al. Search for Θ^{++} pentaquarks in the exclusive reaction $\gamma p \to K^+K^-p$. *Pys. Rev. Lett.*, 97:102001, 2006

S. Chen, H. Avakian, V. Burkert, P. Eugenio, et al. Measurement of deeply virtual compton scattering with a polarized proton target. *Phys. Rev. Lett.*, 97:072002, 2006

K. V. Dharmawardane, P. Bosted, S. E. Kuhn, Y. Prok, et al. Measurement of the x- and Q^2-dependence of the spin asymmetry A1 of the nucleon. *Phys. Lett. B*, 641:11, 2006

M. Ungaro, P. Stoler, et al. Measurement of the N to $\Delta(1232)$ transition at high momentum transfer by π^0 electroproduction. *Phys. Rev. Lett.*, 97:112003, 2006

R. De Vita, M. Battaglieri, V. Kubarovski, et al. Search for the Θ^+ pentaquark in the reactions $\gamma p \to \overline{K}^0 K^+n$ and $\gamma p \to \overline{K}^0 K^0p$. *Phys. Rev. D*, 74:032001, 2006

P. E. Bosted, K. V. Dharmawardane, G. E. Dodge, T. A. Forest, S. E. Kuhn, Y. Prok, et al. Quark-hadron duality in spin structure functions g1p and g1d. *Phys. Rev. C*, 75:035203, 2007

P. Ambrozewicz, D. S. Carman, R. Feuerbach, M. D. Mestayer, B. A. Raue, R. Schumacher, A. Tkabladze, et al. Separated structure functions for the exclusive electroproduction of $K^+\Lambda$ and $K^+\Sigma^0$ final states. *Phys. Rev. C*, 75:045203, 2007

R. Bradford, R. Schumacher, et al. First measurement of beam-recoil observables C_X and C_Z in hyperon photoproduction. *Phys. Rev. C*, 75:035205, 2007

K. Sh. Egiyan, G. A. Asryan, N. B. Dashyan, N. G. Gevorgyan, J.-M. Laget, K. Griffioen, S. Kuhn, et al. Study of exclusive d(e,e'p)n reaction mechanism at high Q^2. *Phys. Rev. Lett.*, 98:262502, 2007

I. Hleiqawi, K. Hicks, D. Carman, T. Mibe, G. Niculescu, A. Tkabladze, et al. Cross sections for the $\gamma p \to K^{*\circ}\Sigma^+$ reaction at $E(\gamma) = 1.7 - 3.0$ GeV. *Phys. Rev. C*, 75:042201, 2007

L. Guo, D. P. Weygand, M. Battaglieri, R. De Vita, V. Kubarov sky, P. Stoler, et al. Cascade production in the reaction $\gamma p \to K^+K^+X$ and $\gamma p \to K^+K^+\pi^-X$. *Phys. Rev. C*, 76:025208, 2007

H. Denizli, S. Dytman, J. Mueller, et al. Q^2 dependence of the $S_{11}(1535)$ photocoupling and evidence for a P-wave resonance in η electroproduction. *Phys. Rev. C*, 76:015204, 2007

K. Park et al. Cross sections and beam asymmetries for $\vec{e}p \to en\pi^+$ in the nucleon resonance region for $1.7 \leq q^2 \leq 4.5(\mathrm{GeV})^2$

D. G. Ireland et al. Bayesian analysis of pentaquark signals from CLAS data. *Phys. Rev. Lett.*, 100(5):052001, Feb 2008

A. S. Biselli et al. First measurement of target and double spin asymmetries for $\vec{e}\vec{p} \to ep\pi^0$ in the nucleon resonance region above the $\Delta(1232)$. *Phys. Rev. C*, 78(4):045204, Oct 2008

I. G. Aznauryan et al. Electroexcitation of the roper resonance for $1.7 < q^2 < 4.5$ GeV^2 in $\vec{e}p \to en\pi^+$. *Phys. Rev. C*, 78(4):045209, Oct 2008

J. P. Santoro et al. Electroproduction of $\varphi(1020)$ mesons at $1.4 \leq q^2 \leq 3.8$ GeV^2 measured with the CLAS spectrometer. *Phys. Rev. C*, 78:025210, Aug 2008

M. H. Wood et al. Light vector mesons in the nuclear medium. *Phys. Rev. C*, 78(1):015201, Jul 2008

R. Nasseripour et al. Polarized structure function $\sigma_{LT'}$ for $^1\mathrm{H}\vec{e}'\mathrm{K}^+\Lambda$ in the nucleon resonance region. *Phys. Rev. C*, 77(6):065208, Jun 2008

P. E. Bosted et al. Ratios of $^{15}\mathrm{N}/^{12}\mathrm{C}$ and $^4\mathrm{He}/^{12}\mathrm{C}$ inclusive electroproduction cross sections in the nucleon resonance region. *Phys. Rev. C*, 78(1):015202, Jul 2008

R. De Masi et al. Measurement of $ep \to ep\pi^0$ beam spin asymmetries above the resonance region. *Phys. Rev. C*, 77(4):042201, Apr 2008

F. X. Girod et al. Measurement of deeply virtual compton scattering beam-spin asymmetries. *Phys. Rev. Lett.*, 100(16):162002, Apr 2008

I. G. Aznauryan et al. Electroexcitation of nucleon resonances from CLAS data on single pion electroproduction. *Phys. Rev. C*, 80(5):055203, Nov 2009

M. Battaglieri et al. Photoproduction of $\pi^+\pi^-$ meson pairs on the proton. *Phys. Rev. D*, 80(7):072005, Oct 2009

X. Qian et al. The extraction of ϕ-N total cross section from $d(\gamma,pK^+K^-)n$. *Physics Letters B*, 680(5):417 – 422, 2009

R. Nasseripour et al. Photodisintegration of ^{4}He into p + t. *Phys. Rev. C*, 80(4):044603, Oct 2009

G. Gavalian et al. Beam spin asymmetries in deeply virtual compton scattering (DVCS) with CLAS at 4.8 GeV. *Phys. Rev. C*, 80(3):035206, Sep 2009

M. Battaglieri et al. Measurement of direct $f_0(980)$ photoproduction on the proton. *Phys. Rev. Lett.*, 102(10):102001, Mar 2009

J. Lachniet et al. Precise measurement of the neutron magnetic form factor g_M^n in the few-GeV^2 region. *Phys. Rev. Lett.*, 102(19):192001, May 2009

G. V. Fedotov et al. Electroproduction of $p\pi^+\pi^-$ off protons at $0.2 < q^2 < 0.6$ GeV^2 and $1.3 < w < 1.57$ GeV with the CLAS detector. *Phys. Rev. C*, 79(1):015204, Jan 2009

M. Osipenko et al. Measurement of semi-inclusive π^+ electroproduction off the proton. *Phys. Rev. D*, 80(3):032004, Aug 2009

Y. Prok et al. Moments of the spin structure functions and for $0.05 < q2 < 3.0$ GeV^2. *Physics Letters B*, 672(1):12 – 16, 2009

S. Morrow et al. Exclusive ρ^0 electroproduction on the proton at CLAS. *Euro. Phys. J. A*, 39:5–31, 2009

M. Nozar et al. Search for the photoexcitation of exotic mesons in the $\pi^+\pi^+\pi^-$ system. *Phys. Rev. Lett.*, 102(10):102002, Mar 2009

Y. Ilieva et al. Evidence for a backward peak in the $\gamma d \rightarrow \pi^0 d$ cross section near the η threshold. *The European Physical Journal A - Hadrons and Nuclei*, 43:261–267, 2010. 10.1140/epja/i2010-10918-x

M. E. McCracken et al. Differential cross section and recoil polarization measurements for the $\gamma p \rightarrow K^+\Lambda$ reaction using CLAS at jefferson lab. *Phys. Rev. C*, 81(2):025201, Feb 2010

S. Anefalos Pereira et al. Differential cross section of $\gamma n \rightarrow K^+\Sigma^-$ on bound neutrons with incident photons from 1.1 to 3.6 GeV. *Physics Letters B*, 688(4-5):289 – 293, 2010

ABSTRACT OF THE DISSERTATION

Ξ Hyperon Photoproduction

from Threshold to 5.4 GeV

with the CEBAF Large Acceptance Spectrometer

by

John Theodore Goetz

Doctor of Philosophy in Physics

University of California, Los Angeles, 2010

Professor Bernard M. K. Nefkens, Chair

The cascade (Ξ) hyperons provide a unique method to study the flavor independence of quantum chromodynamic (strong force) interactions. By comparing the Ξ spectrum to the light-quark baryons (N's and Δ's), this symmetry can be investigated. Furthermore, a search for strange-quark resonances having quantum numbers not in the SU(3) ordering provides a test of the phenomenological model: the *eightfold way*.

The cascade spectrum is studied with the *g12* experiment which consisted of a bremsstrahlung photon beam from threshold to 5.4 GeV on a hydrogen target using the CLAS detector at Jefferson National Accelerator Facility. The excitation functions were measured for the $\Xi^-(1320)$ and $\Xi^{*-}(1530)$ in the reaction $\gamma p \to \Xi^- K^+ K^+$ and an order of magnitude improvement was obtained over previous CLAS experiments *g6* and *g11*. Photoproduction of both states plateau 1.7 GeV above the threshold beam energy and the total cross section remains constant at ~ 9 for the $\Xi^-(1320)$ and 2 nb for the $\Xi^{*-}(1530)$ up to the maximum beam energy measured. Our data supports the Nakayama et al. model[41] for Ξ^- photoproduction based on processes with several intermediate Y^* states.

Total cross section upper limits for photoproduction of Ξ^{*-} states at 1620, 1690 and 1820 MeV were found to be 0.78, 0.97 and 1.1 nb respectively, with a confidence level of 90%. This is found to be consistent with the vector-meson dominance model of the photon. In addition, several iso-exotic states — the often controversial Ξ^{--}, Ξ^{+}, Σ^{--} and Σ^{++} states — were qualitatively looked for in the data and no evidence was found with an estimated 100 nb sesitivity.

Introduction

The field of particle physics seeks to understand the nature of matter at a fundamental level. Physicists have always wished to know how mass and energy come about and how they interact with each other and the universe. Democritus' hypothesis of the atomic structure of matter, put forth over 2500 years ago, has prevailed as one of the most profound advancements in the natural sciences. Yet, only in the last two centuries have we made progress in identifying and categorizing the basic constituents that compose this universe.

Great progress has been made in our understanding of matter starting with the discovery of the atom as an electrically positive nucleus surrounded by negatively charged electrons as proposed by Rutherford and Bohr[1] in 1911 and depicted in Fig. 1(b). It was found by Chadwick[2] in 1932 that the nucleus consists of protons and neutrons, and in 1937, Stern et. al.[3] found evidence that protons were not point-like as electrons seemed to be, but had some internal structure. During the ensuing couple decades, cosmic-ray and collider experiments revealed new particles that did not fit the proton-neutron-electron scheme of matter, and several new classes of subatomic particles including K-mesons and hyperons were identified.

In 1964, Gell-Mann organized many of these experimentally seen particles into what he called the *eightfold way*. For the first time, subatomic particles were organized so that their properties and quite literally their very existence could be predicted. In fact, Gell-Mann's organizational model successfully predicted the existence[4] of an unknown particle known today as the Ω^- baryon. From all the known resonances that were observed (more than 20 at the time) Gell-Mann

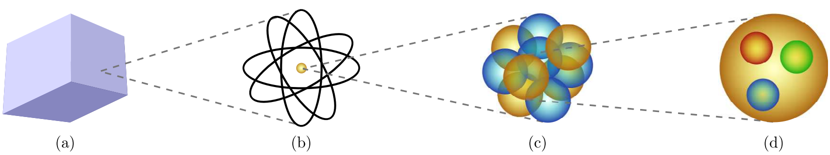

Figure 1: A block of matter (a) is made of atoms (b) which consist of electrons orbiting a positively charged nucleus (c). The nucleus is comprised of protons and neutrons which are each made of three *valence* quarks (d).

Table 2: The six *flavors* of quarks which make up all hadronic matter in the Standard Model. All have spin $\frac{1}{2}$. The *current-quark* mass is shown in MeV for each[8].

electric charge	Generation I	II	III
$\frac{2}{3}$	up (u) 3	charm (c) 1300	top (t) 171k
$-\frac{1}{3}$	down (d) 5	strange (s) 105	bottom (b) 4.2k

found that he could describe their properties quite naturally by the existence of three constituents — the up, down and strange *quarks* which have half-integer spin and fractional electric charge. Over the past 50 years, three additional, heavier quarks have been added for a total of six which are categorized into three (and likely not more than three[5, 6]) "generations" as shown in Table 2*.

This theory, for which Gell-Mann won the Nobel Prize, formed the basis for what is known as the Standard Model of particle physics. The ideas behind this model retained the atomic structure of matter, and extended it to the interacting forces between particles. Protons and neutrons became part of a family of particles called *hadrons*, while electrons became part of a family of particles called *leptons*. The forces between these particles were then mediated by exchange of other particles called *bosons*; the photon for example is the force carrier of the electromagnetic interaction.

Hadrons are complex particles making them difficult to understand. Unlike the simpler point-like leptons, they are composed of two or more quarks and/or anti-quarks. The quarks themselves carry a unique three dimensional charge called color. The color-charge for quarks can be one of three colors: red, blue or green. The color-charge for anti-quarks can be one of three colors: anti-red, anti-blue and anti-green.

Quarks and anti-quarks do not exist in isolation, but are found only in specific combinations. Experimental observation has shown these combination to be colorless. Three quarks in combination, whose colors are red, blue and green, are colorless. One quark and one anti-quark in combination with opposite colors, such as red and anti-red, is also colorless. The three-quark combination is called a *baryon* and the quark-anti-quark combination is called a *meson*.

This dissertation describes the work done to gain understanding of nucleon structure via measurement of the excitations of *baryons*, the lowest lying states (lowest in terms of mass) which can be organized by SU(3) symmetry[7], using the three lightest quarks: *up*, *down* and *strange*, as shown in Fig. 2. Quantum chromodynamics, or `QCD`, is the leading theory to describe the strong force or the interactions between quarks which give rise to the nucleon structure. However,

*In this work, we use units where the speed of light (c) and Planck's constant ($\hbar$) are equal to unity, making the units for mass, energy and momentum that of electron-volts (eV); the division by multiples of c is implied.

it is analytically insoluble and only recently have computing techniques with lattice QCD been able to produce reliable results.

The modern formalism used to describe mass and the forces governing the interaction between masses is not the familiar $F = ma$ of Newton, but what is known as Lagrangian formulation. This is a way of encoding the equations of motion so that symmetries that correspond to conservation laws become easily accessible. The formulation consists of a single function, called the Lagrangian, which contains all the fundamental particle interactions. It is an abstraction from which the equivalent of $F = ma$ may be derived — though generally this is not done directly. Furthermore, we currently lack the capability to do so analytically for the "strong" interactions between quarks. The Lagrangian of QCD ($\mathcal{L}_{\texttt{QCD}}$) which governs the interactions of quarks and their intermediary fields, gluons, is given as

$$\mathcal{L}_{\texttt{QCD}} = \overline{\psi}_i \left(i\gamma^\mu \left(D_\mu\right)_{ij} - m\delta_{ij} \right) \psi_j - \frac{1}{4} G^a_{\mu\nu} G^{\mu\nu}_a, \tag{1}$$

where ψ_i is the quark field of flavor i, $G^a_{\mu\nu}$ is the gluon field strength tensor for color-charge a:

$$G^a_{\mu\nu} = \partial_\mu G^a_\nu - \partial_\nu G^a_\mu - g f_{abc} G^b_\mu G^c_\nu, \tag{2}$$

and m is the mass of the quark. The term $\left(D_\mu\right)_{ij}$ consists of the self interaction for the quarks and the interaction between the quarks and the gluon fields:

$$\left(D_\mu\right)_{ij} = \partial_\mu \delta_{ij} - g G^a_\mu \gamma^\mu T^a_{ij}. \tag{3}$$

Inserting this into the Lagrangian yields

$$\mathcal{L}_{\texttt{QCD}} = i\overline{\psi}_i \gamma^\mu \partial_\mu \psi_i - \overline{\psi}_i m \psi_i - g\overline{\psi}_i G^a_\mu \gamma^\mu T^a_{ij} \psi_j - \frac{1}{4} G^a_{\mu\nu} G^{\mu\nu}_a, \tag{4}$$

where the first term is quark self interaction, the second term depends on the quark mass (a subtle issue that is discussed later), the third is the quark-gluon interaction, and the last term contains the gluon-gluon interaction. The T^a_{ij} are

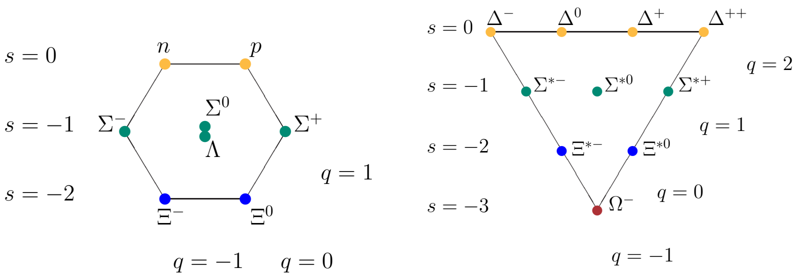

Figure 2: Organization of the lowest lying baryons in the octet and decuplet of Gell-Mann's *eightfold-way*.

the SU(3) generators which can be represented by the Gell-Mann matrices — these are the SU(3) analog of the Pauli matrices. In the quark-gluon interaction term, g is a constant and the same for all quarks. It may scale with the energy of the interaction, but is flavor independent. Therefore, this theory suggests all quark-gluon interactions are independent of quark flavor.

Notice, the mass term (second in Eq. 4) is the only one that is dependent on the quark flavor. Therefore, as far as QCD is concerned, the quark-quark interaction should manifest itself with a simple relation between the masses of particles made of QCD quarks. A direct consequence of this is that the excitation spectra of baryons, three quark states whose binding energy is dominated by QCD, should be independent of the flavor of the constituent quarks. Moreover, the light baryon resonances, those made from up and down quarks only, will be governed by the same interactions as the doubly-strange baryons (i.e. those with two strange quarks and one up or down quark). The result is that the spectra of these two will have nearly identical shapes. Each light octet (N^*) and decuplet (Δ^*) state will have a corresponding octet or decuplet Ξ^* state. This will also hold for singly-strange baryons as discussed in the following sections. The phrase "nearly identical" was used because the doubly-strange *cascade* states have two identical strange quarks and therefore their spectrum contains no singlets, so there are no Ξ^* analogs to the singlet Λ^* states for example.

A perfect one-to-one correlation should not be expected. There will be electro-weak corrections due to the charge of the quarks via quantum electrodynamics (QED). Furthermore, there are spin-spin and spin-orbit energies that can contribute a shift in the mass differences when a d quark is replaced by an s quark. Once all these effects are taken into account, mismatching states in the spectra can be interpreted as some new physics not included in $\mathcal{L}_{\texttt{QCD}}$ of Eq. 1.

The masses shown in Table 2 are what is known as the *bare* or *current*-quark masses. These are the best estimates of what the masses would be for free quarks — that is, outside the influence of an external QCD potential. These values are the quark masses that would be inserted into the QCD Lagrangian provided it was solvable analytically, but there are certain problems with these estimates.

Discussions on masses of particles that can not be measured directly become philosophic in nature quickly. However, a brief investigation into this subject is necessary at this point. In a naïve model, one could say that there are three quarks (uud) in a proton of mass 938 MeV and therefore they are approximately one third its mass which comes to 313 MeV. This is obviously much higher than the values given in Table 2. There are other particles we could look at besides the proton. For example, the pion is composed of two light quarks (up and down) and has a mass of 140 MeV which brings the mass of the up and down quarks to around 70 MeV. Still higher than quoted, but much closer.

So what might be going on here? The current-quark theory suggests these light quarks (a few MeV for the *up* and *down*) are surrounded by a "bubbling sea" of gluons and short-lived quark/anti-quark pairs. The interactions of these particles coming in and out of existence constantly on very short time scales effectively adds the mass that is "missing" to the hadronic particles. Even with all the calculations made and data collected on this subject[8], there is substantial controversy on these vital ingredients to the Standard Model and QCD and more data is needed.

The cascade states provide an accessible way to study the up/down quark mass difference. Since the two strange quarks are much more massive than the other light (up or down) quark, interchanging the light quark with another is a relatively small change on the whole system. Therefore, the effect of this switch is isolated.

This dissertation presents an analysis of the lowest lying doubly-strange baryons and the comparison to the known light and singly-strange baryon spectra. The goal is to show the extent to which the strong force is flavor independent. If the three spectra have a one-to-one correspondence where the differences can be fully explained (by mass differences, QED, etc.) then the QCD Lagrangian as written in Eq. 1 will have deeper experimental support. If a discrepancy can be identified, this will be an indication that a modification of the QCD Lagrangian would be required.

0.1 Cascade Hyperons

Listed in the *Review of Particle Properties*[8] by the PDG, are eleven cascade baryons. Only two of these have the highest (4-star) designation indicating nearly definitive proof of their existence. The spin and parity are known for only two more states and the others are tenuously identified by mass and width with little or no spin/parity information as shown in Table 3. The branching ratios of these states are still in the beginning stages of exploration and most measurements are only qualitative in nature — the PDG writes for the $\Xi(1820)$ that the ΛK branching ratio is "large" while the $\Xi\pi$ branching ratio is "small."

The N^* and Δ^* states, on the other hand, have many observed resonances. These states are much broader in width and many overlap and become difficult to separate. The Σ^* states suffer from the same problems, but to a lesser extent. The Ξ^* states are far narrower than their non-strange counterparts as shown in Fig. 3. This can be explained partially by considering the decay of an excited Ξ^* to the ground state plus a pion ($\Xi\pi$). The pion decay requires a light quark-anti-quark pair to form via the strong interaction. The anti-quark combines with the single light quark in the Ξ^* to form the pion, and the remaining quark joins the two strange quarks to form the ground state Ξ. The anti-quark combining with one of the strange quarks in the baryon is suppressed by phase space. In other words, the decay of the Ξ^* would be ΛK or ΣK, which requires approximately 150 MeV more mass than the $\Xi\pi$ decay. This suppression and the limited decay channels makes the cascade states narrow and allows them to be separated and identified without the use of techniques such as partial wave analysis.

There are several reasons the cascades are uniquely interesting in baryon spectroscopy and QCD in general. Because they contain two strange quarks and only a single light (up or down) quark, they can provide a straight forward measurement of isospin symmetry breaking. Where isospin can be thought

Table 3: All Ξ states listed in the *Review of Particle Properties* by the Particle Data Group (PDG) with masses and widths given in units of MeV. The width of the ground state is given as $c\tau$ in centimeters. Note that most of the spin and parity values are unknown.

mass (MeV)	width (MeV)	Spin$^{\text{parity}}$	rating (1–4)
1322	4.9 cm	$\frac{1}{2}^+$	****
1532	9 MeV	$\frac{3}{2}^+$	****
1620	30		*
1690	30	$\frac{1}{2}^-?$[a]	***
1820	24		***
1950	60		***
2025	20	$\geq \frac{5}{2}^?$	***
2120	20		*
2250	50		**
2370	80		**
2500	100		*

[a]See Sec. 0.3.2 concerning the spin and parity measurement of the $\Xi(1690)$.

of as the interchangeability of an *up* and *down* quark. There are only two cascade particles of any particular mass state with just this quark interchange: negatively charged made from the quarks *dss* and neutral made from *uss* quarks. For example, the mass difference between the ground state Ξ^- and the ground state Ξ^0 is a very direct way to observe this symmetry breaking. Moreover, they are narrower resonances which makes them relatively easy to identify and separate. Finally, The only QCD calculations being made today which are nearly model independent (lattice QCD) have only recently been able to approach the mass range of the heavier baryons, i.e. the Ξ^* states in particular.

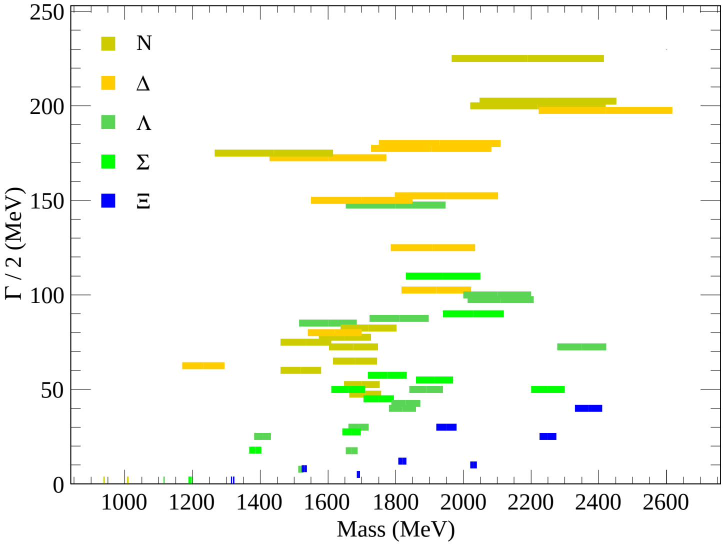

Figure 3: Plotted here are the 3 and 4-star light and singly-strange baryons along with the 2, 3 and 4-star cascade states. The y-axis is the half-width of the states and the full width is indicated by the horizontal extent of the bars.

0.2 Predicted Ξ States

The most referenced prediction of the Ξ spectrum comes from the work of Capstick et al.[9] using a relativistic quark model which is based on the previous non-relativistic work of Isgur and Karl[10]. The theoretical predictions indicate that there should be many more Ξ states than have been seen experimentally, as shown in Fig. 4, however, only limited information concerning relative branching ratios is available.

Fig. 5 shows the Ξ^* predictions for both the chiral-dynamic[11] and algebraic[12] models. The results shown in Figs. 4 and 5 are similar: there are many more states predicted than observed, and although the intensity of many of them may be small, their widths should be narrow enough, following the trend seen in Fig. 3, so they can be separately identified. It is interesting to note that the overall trends of these four predictions are similar. For a more detailed analysis of the relative merits of these models, see Ref. [13].

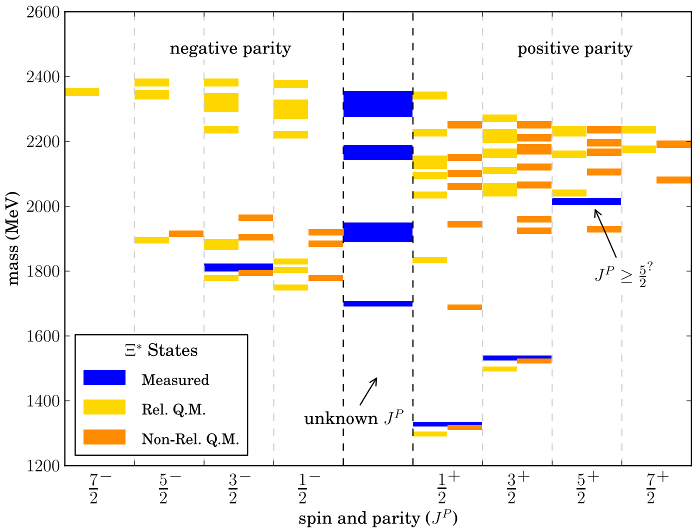

Figure 4: Non-relativistic and relativistic quark model predictions from Capstick et al. with observed Ξ^* resonances (2, 3 and 4-star states) in blue. The vertical extent of the *observed* states indicate their widths.

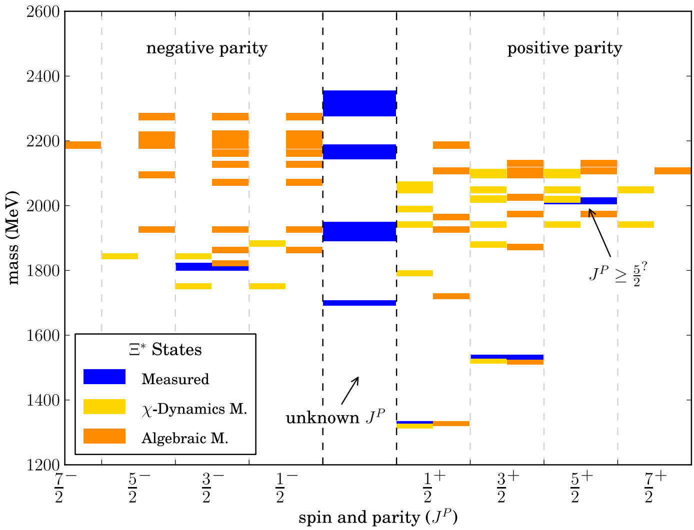

Figure 5: Chiral-dynamic and algebraic model predictions with observed Ξ^* resonances (2, 3 and 4-star states) in blue. The vertical extent of the *observed* states indicate their widths.

0.3 Existing Evidence for Ξ^* States

By comparing the Ξ states to the other known nucleon states with one or no strange quarks, the beginnings of the symmetry expected out of `QCD` can be observed. Figs. 6 and 8 demonstrate that the mass separation from the ground state to the first excited is roughly equivalent across the N's, Σ's and Ξ's. There also seems to be only a uniform shift of the entire spectra corresponding to the bare mass of the strange quark as listed in Table 2 on page 2.

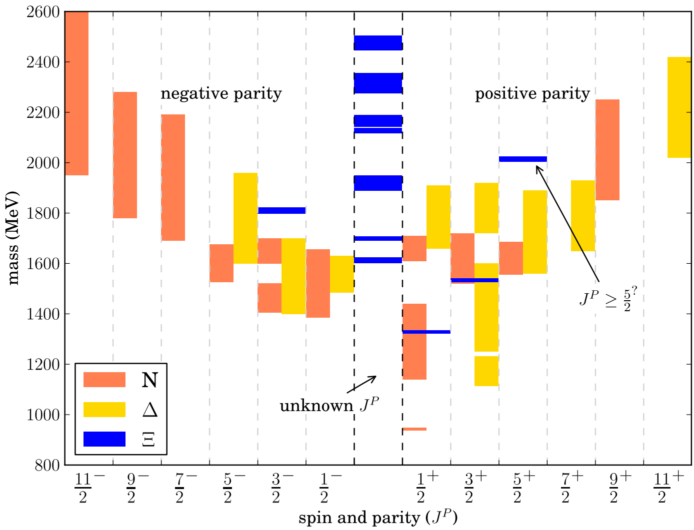

Figure 6: 3 and 4-star N* and Δ^* resonances in orange and yellow respectively, overlayed with Ξ^* resonances (1 through 4-star states) in blue. The vertical extent of the bars indicates the widths of the states.

By adjusting the spectra in these figures so that the masses are relative to the ground states — proton for the non-strange baryons, the $\Sigma(1190)$ for singly-strange, and the $\Xi(1320)$ for the cascades — Figs. 7 and 9 are obtained. This makes the comparison of the spectra easier to see and understood. So far, the data on the Ξ^* states show *no inconsistencies* with the flavor independence of the strong interaction. In other words, all the Ξ states with known spin and parity have a corresponding N/Δ resonance *and* a corresponding Σ resonance. The lack of data for the cascades means the inference of flavor independence is still unresolved and requires more experimental evidence.

The Ξ states shown in Figs. 6 and 8 include all those from Table 3 for completeness. As discussed later in this chapter, however, several reported states may be indistinguishable from background fluctuations and should not be considered for this comparison to the N* and Σ^* states. Note that virtually

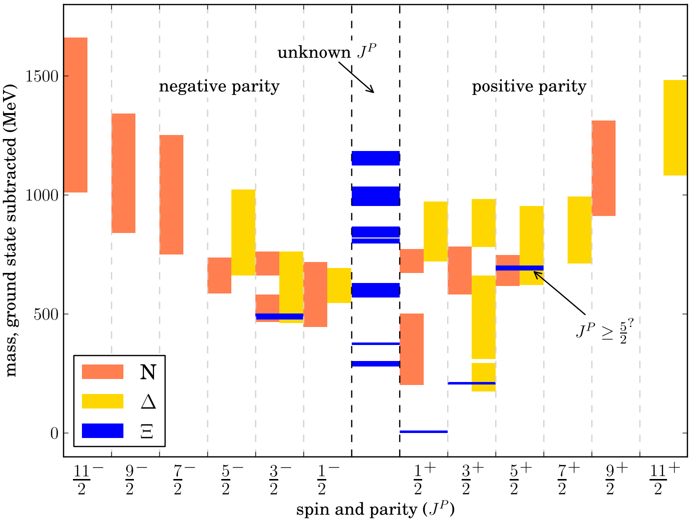

Figure 7: Same as Fig. 6 where the proton mass has been subtracted from the nucleon states and the ground state $\Xi(1320)$ mass has been subtracted from the cascade states.

all data on the cascade spectrum are from hadron interactions such as:

$$\mathrm{K}^-\mathrm{p} \to \Xi^{*-}\mathrm{K}^+, \tag{5}$$

$$\Sigma^-\mathrm{p} \to \Xi^{*-}\mathrm{K}^+, \tag{6}$$

and that the excited cascade is measured as the invariant mass of its decay particles — usually $\Xi\pi$ or ΛK.

In this section, I will evaluate the evidence for the states that are kinematically accessible with the 5.4 GeV photon beam used in the *g12* experiment discussed in the following chapters. The ground and first excited states are well measured by several experiments and therefore will not be discussed here.

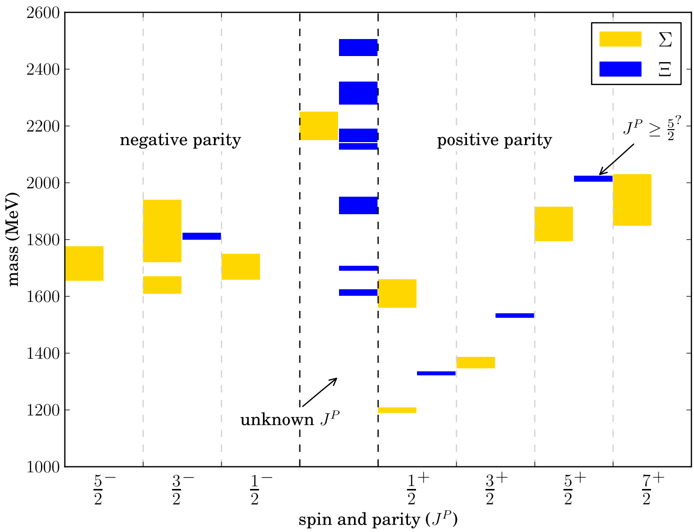

Figure 8: 3 and 4-star Σ^* resonances in yellow with Ξ^* resonances (1 through 4-star states) in blue. The vertical extent of the bars indicates the widths of the states.

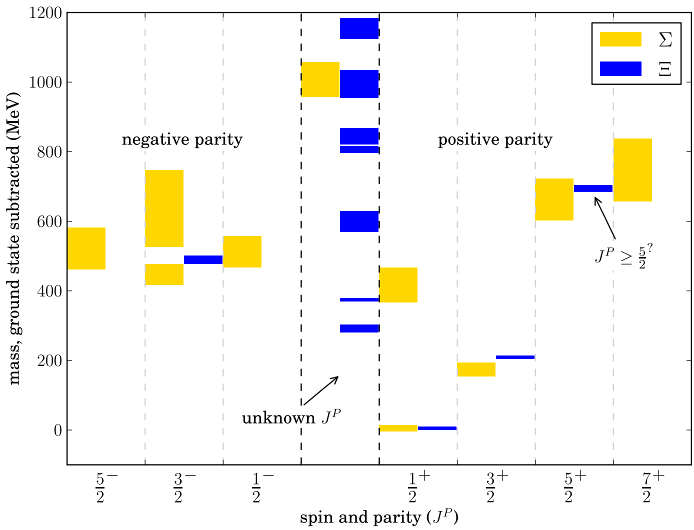

Figure 9: Same as Fig. 8 where the $\Sigma(1193)$ mass has been subtracted from the Σ states and the ground state $\Xi(1320)$ mass has been subtracted from the cascade states.

0.3.1 $\Xi(1620)$ Status

There is only suggestive evidence for the $\Xi(1620)$ state which is nearly indistinguishable from statistical fluctuations. It has been classified as a one-star state in the Review of Particle Properties[8] and so it is included in this report for completeness. The first indication was from Apsell et al.[95] in 1969 with a K^- beam at 2.87 GeV/c on the hydrogen bubble chamber at Brookhaven National Laboratory. The peak which was observed for the $\Xi(1630)$ consisted of 15 events with a signal to background ratio close to unity. Similar results were obtained in 1972 by Ross et al.[14] as shown in Fig. 10 and by Briefel et al.[15] in 1977 as shown in Figs. 11 and 12. All of these reported a state close to 1620 MeV mass in the same reaction:

$$K^-p \rightarrow \Xi^{*0}(1620)K^0, \tag{7}$$

where the excited cascade decays to the ground state via pion emission:

$$\Xi^{*0}(1620) \rightarrow \Xi^-(1320)\pi^+. \tag{8}$$

In these data, the charged state $\Xi^{*-}(1620)$ was not observed. This is surprising since the state only requires the interchange of an *up* quark with a *down* quark. Figs. 10(b) and 12 show the same data for the reaction

$$K^-p \rightarrow \Xi^{*-}(1620)K^+, \tag{9}$$

where the cascade decays to the ground state in the same manner as before via pion emission.

Later experiments produced much higher statistics and did not see any signal in the mass range around 1620 MeV, either for the neutral or the charged state. An example of this result is shown in Fig. 13 using the hyperon beam (Σ^-) at

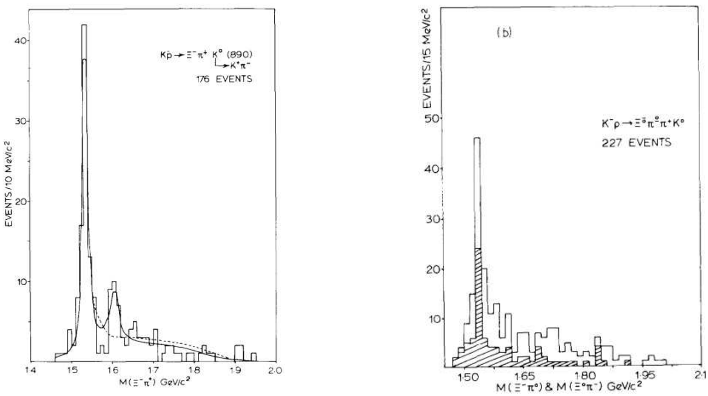

Figure 10: Evidence claimed for the processes $K^-p \rightarrow \Xi^{*0}(1620)K^0$ in the invariant mass of $\Xi^-(1320)\pi^+$ (left), along with the invariant mass of $(\Xi\pi)^-$ in the reaction $K^-p \rightarrow (\Xi\pi)^-\pi^+K^0$ (right) from Ross et al., 1972, Ref. [14].

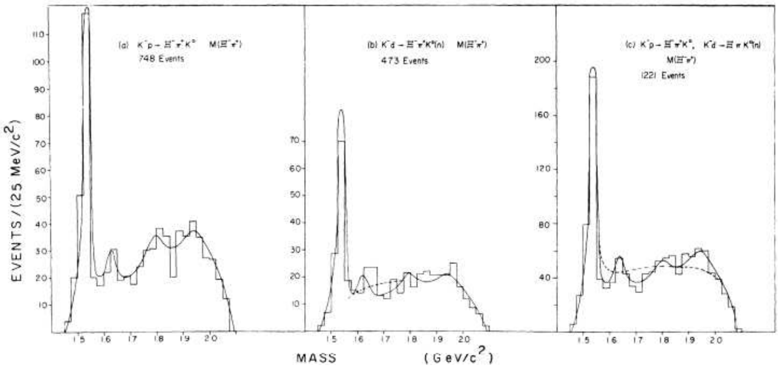

Figure 11: Evidence claimed for the process $\mathrm{K^-p} \to \Xi^{*0}(1620)\mathrm{K}^0$ in the invariant mass of $(\Xi\pi)^0$ from Briefel et al., 1977, Ref. [15].

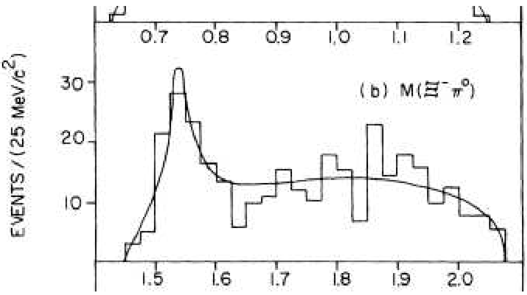

Figure 12: Invariant mass of $\Xi^-\pi^0$ in the process $\mathrm{K^-p} \to \Xi^-\pi^0\mathrm{K}^+$ from the same paper that claims evidence for the $\Xi^{*0}(1620)$, shown in Fig. 11 — Briefel et al., 1977, Ref. [15].

CERN, as contrasted to the kaon beam of the previous results. All other evidence from kaon beams have roughly the same amount of statistics and could not give definitive proof for the existence of the $\Xi(1620)$. It is not expected that Ξ production should differ significantly between kaon and hyperon beams since both are clearly dominated by *hadronic* interactions even though they do have significantly different reaction mechanisms, and these experiments produced an upper limit on the existence of this state low enough so as not to be considered a genuine Ξ^* resonance.

0.3.2 Ξ(1690) Status

The next cascade resonance above 1530 MeV with a clear signal is the $\Xi(1690)$ which is a three-star state in the Review of Particle Properties[8]. This is an interesting state because predictions for its properties are different for the different models. The non-relativistic quark model does predict a $J^P = \frac{1}{2}^+$

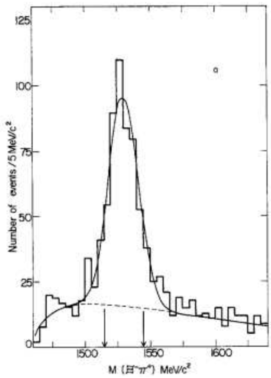

Figure 13: Invariant mass of $\Xi^-\pi^+$ in the reaction $\Sigma^- p \to \Xi^{*0} K^0$ from Briagi et al., 1981[16].

state around 1690 MeV, but the closest state in the relativistic model is around 1750 MeV. The algebraic model predicts a state around 1690 MeV but the chiral-dynamic model pushes the same state toward 1800 MeV. Therefore, an accurate measurement of the $\Xi(1690)$ can guide theory to a better model.

The experimental evidence for this low-lying state seems clear. The first of which came from the Dionisi et al.[17], shown in Fig. 14, but the signal was shown as the invariant mass of the Σ^+K^- which is right at threshold for the $\Xi(1690)$. This means the analysis was susceptible to threshold effects which are discussed in detail for the *g12* experiment in Chapter 3. To account for this, the authors showed a normalized invariant mass of the Σ^+K^+ as the dashed line in Fig. 14. Requiring two strange quarks in a baryon does not admit a charge of +2 and therefore this figure makes for compelling evidence the existence of the $\Xi(1690)$.

Further evidence of existence was obtained using the `SPS` Ξ^- hyperon beam at `CERN`, where Biagi et al.[16, 18] were able to measure the $\Xi(1690)$ state in ΛK^- and ΛK^0 events shown in Figs. 15 and 16. The state, being 100 MeV above the ΛK threshold, does not suffer from the same ambiguities of the ΣK data, and the evidence is quite conclusive. The $\Xi(1820)$ resonance seen in these figures are discussed in the following sections.

The $\Xi(1690)$ was seen first by a ΛK decay, but the $\Xi\pi$ is also kinematically accessible and provides approximately 100 MeV of additional phase space. The most convincing evidence for the $\Xi\pi$ decay came from the Σ^- beam at `CERN`[19] shown in Fig. 17. Here, the $\Xi(1690)$ is shown as a small bump on a very large background. Our estimate of the significance of this signal is 6σ, with approximately 1350 ± 230 events in the peak.

The spin and parity of the $\Xi(1690)$ were measured by Aubert et al.[20] via the decay

$$\Lambda_c \to \Xi^-\pi^+K^+. \tag{10}$$

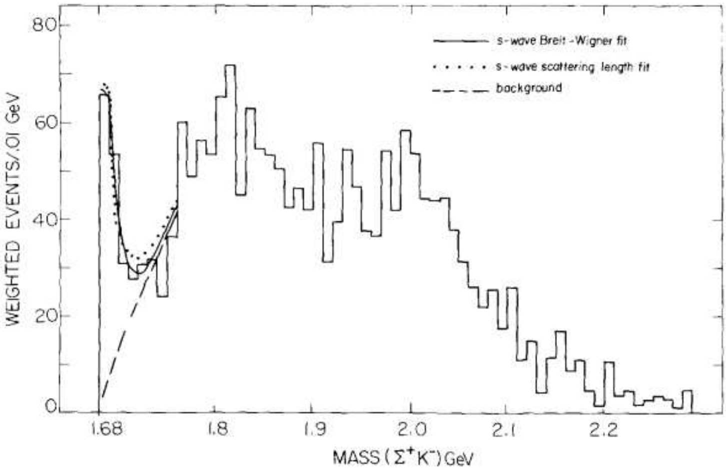

Figure 14: Invariant mass of Σ^+K^- from Dionisi et al., 1978, Ref. [17]. The dashed line is the background estimate and comes from the invariant mass of Σ^+K^+.

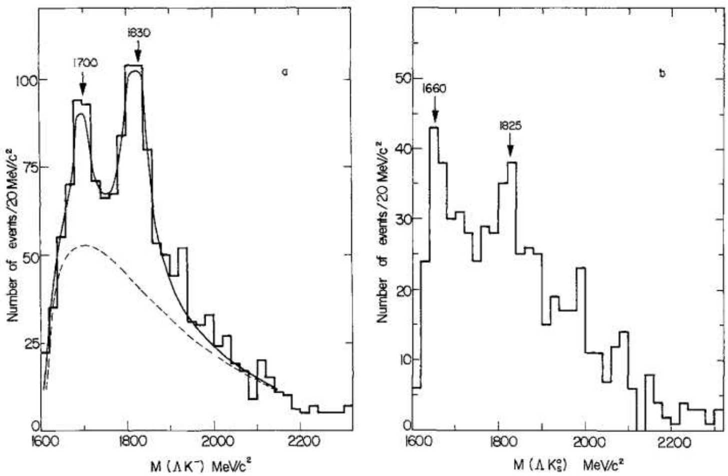

Figure 15: Invariant mass of ΛK using the Ξ^- hyperon beam at CERN from Biagi et al. 1981, Ref. [16].

The invariant mass of the $\Xi^-\pi^+$, shown in Fig. 18 of this work and Fig. 8 of Ref. [20], has "a dip in overall intensity in the Ξ(1690) region, with very little effect on the phase." The signal amplitude, combined with this dip, "suggests" a spin and parity of $\frac{1}{2}^-$. This is based on only a fraction of the data available from this BaBar experiment and more conclusive results are still forthcoming.

There is only suggestive evidence from the CLAS experiment *g6* that the

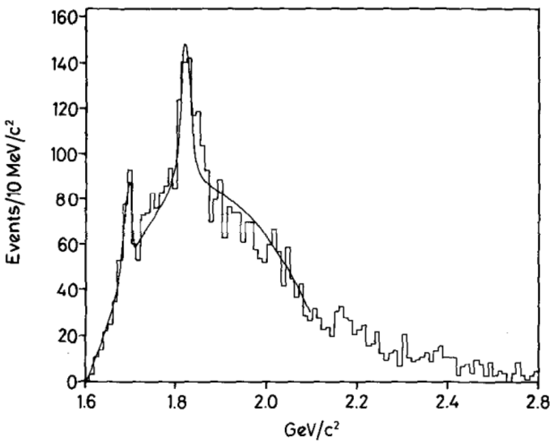

Figure 16: Invariant mass of ΛK^- using the Ξ^- hyperon beam at CERN from Biagi et al. 1987, Ref. [18].

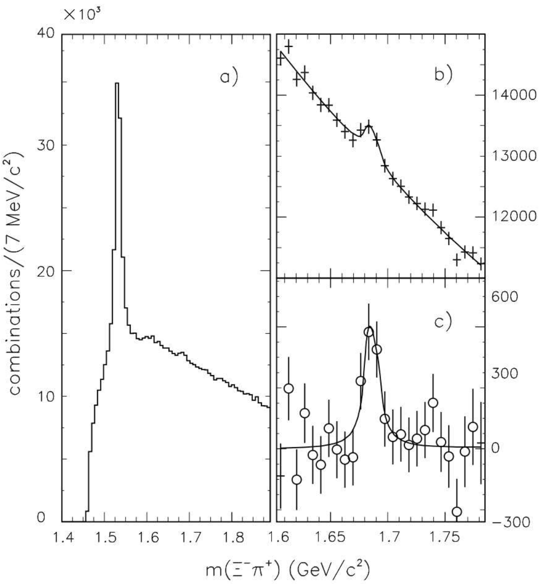

Figure 17: Invariant mass of $\Xi^-\pi^+$ using the Σ^- beam at CERN from Adamovich et al., 1997, Ref. [19].

photoproduction cross section for the $\Xi^-(1690)$ is large enough to make a spin and parity measurement feasible. The missing mass off K^+K^+ in the reaction $\gamma p \rightarrow K^+K^+X^-$, shown in Fig. 19, and the potential for the identification of several higher mass Ξ states motivated the SUPER-G proposal for the *g12* experiment discussed in the following chapters.

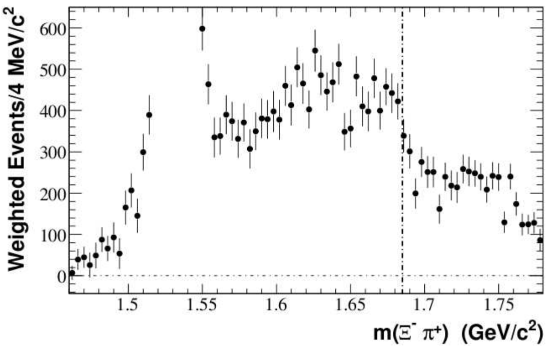

Figure 18: Invariant mass of $\Xi^-\pi^+$ from Λ_c decay from Aubert et al., 2008, Ref. [20].

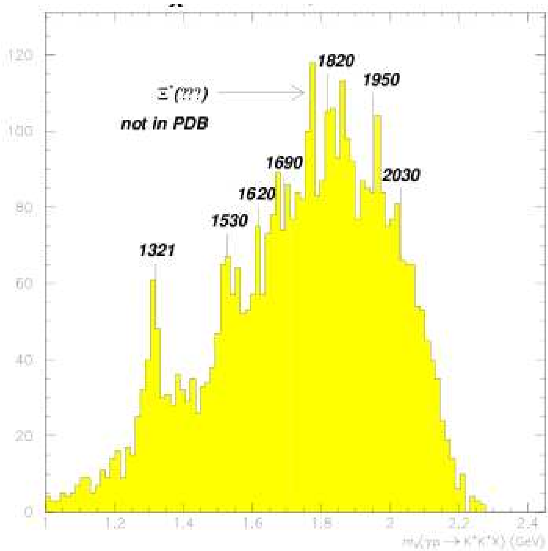

Figure 19: Missing mass of K^+K^+ in the reaction $\gamma p \rightarrow K^+K^+X^-$ from the *g6c* experiment with `CLAS`. Taken from Ref. [25].

0.3.3 $\Xi(1820)$ Status

The next state in the spectrum, the $\Xi(1820)$, is also clearly observed by Biagi et al. as shown in Figs. 15 and 16. These are ΛK events only and there is little or no apparent signal in $\Xi\pi$ decay data (see Fig. 17 for example). Alitti et al.[96] claim a $\Xi\pi$ signal was observed with K^-p interactions as shown in Fig. 20, however our estimate makes this indistinguishable from noise.

Even without the $\Xi\pi$ signal, the $\Xi(1820)$ is unique among the cascades since it is the only one with a measured spin and parity. The state is "consistent" with a $J = \frac{3}{2}$ state and the data "favors" negative parity from a *moments* analysis

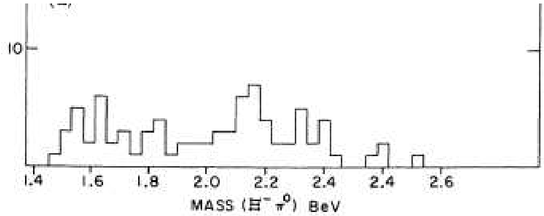

Figure 20: Invariant mass of $\Xi^-\pi^0$ from Alitti et al., 1969, Ref. [96].

done by Biagi et al.[97], though neither measurement was entirely conclusive.

0.3.4 Higher Mass Ξ States

There are few Ξ states above 1820 MeV that appear to be genuine resonances. Most of these were claimed as seen in the invariant mass of X from the reaction

$$\mathrm{K}^-\mathrm{p} \rightarrow \mathrm{K}^+\mathrm{p}X. \tag{11}$$

shown in Fig. 21 by Jenkins et al.[98]. In these two plots, the Ξ(1530) at 2340 GeV^2 and the Ξ(1820) at 3310 GeV^2 are strong resonant signals. In Fig. 21(b), the Ξ(1620) and the Ξ(1690) are indistinguishable from each other and the data is inconclusive. The two higher states at 4100 GeV^2 and 4950 GeV^2 which correspond to Ξ(2025) and Ξ(2250) respectively, consist of a single bin in (b). When combined with (c), these states have a significance of 3.3 σ and 2.8σ. The highest state claimed in this figure is the Ξ(2500), however this peak is separated from the phase-space peak by only a single bin in the histogram and the quality of the fit suffers, giving this state a one-star rating in the Review of Particle Properties[8].

There is little further data on these high-mass Ξ states, but the experimental signals are tantalizing indeed, and they all seem to be narrow enough to obviate separation techniques. Though they are rare and difficult to produce, the potential exists to make enough of them to measure other properties such as spin and parity.

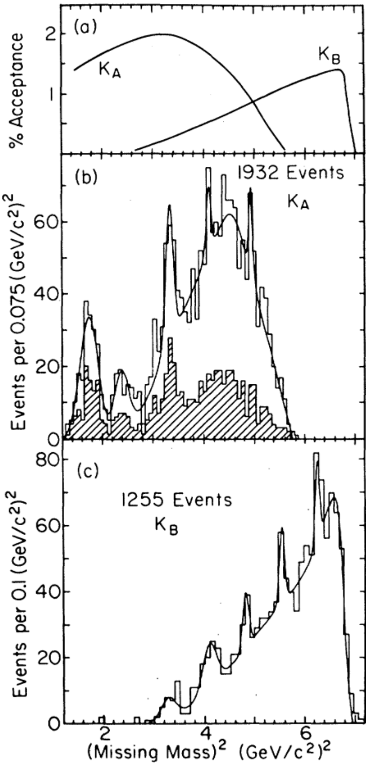

Figure 21: Invariant mass of ΛK and ΣK using the kaon beam at Brookhaven from Jenkins et al., 1983, Ref. [98].

0.4 Search for *Iso-exotic* States

There have been many recent experiments focused on baryon states with quantum numbers that can only be made from four quarks and an anti-quark. These would-be states are *patently exotic* since they do not fit into the baryon or meson groups of known and predicted particles in the Standard Model. There are three light baryon states with quantum numbers that require no less than five quarks, two of which have a strangeness -2 and usually labeled as Ξ^+ and Ξ^{--}.

There is evidence for and against all three of the penta-quark states. Recent high-statistics searches have yielded no signals and the excitement which drove many of these penta-quark experiments has all but died out. For a detailed examination of the various experiments associated with the penta-quark search, see Ref. [8]. In spite of the evidence against the penta-quarks, this work includes findings from the *g12* experiment on the search for doubly-strange *patented exotics*, the Ξ^+ and Ξ^{--}, as well as other exotic states such as Σ^{++} and Σ^{--}.

Chapter 1

The CLAS detector at JLab and the *g12* Experiment

The analysis described in this work uses data collected during the *g12* run period of the CLAS detector[21] at the Thomas Jefferson National Accelerator Facility (TJNAF) shown in Fig. 1.1, also called Jefferson Laboratory (JLab). The JLab site houses the Continuous Electron Beam Accelerator Facility[22] (CEBAF, Fig. 1.2) which provides an electron beam to three halls A, B and C. Each hall houses a particle detector with different strengths and weaknesses. These halls along with a free electron laser and associated research facilities provides JLab with a wide range of accessible particle experiments. Also, JLab's Theory Center is very active in the physics domain of the experimental halls and beyond, using an associated lattice-QCD computing cluster.

In Hall B of JLab, the CEBAF Large Acceptance Spectrometer (CLAS) is, in essence, a large acceptance multi-wire proportional drift-chamber (DC). The main purpose of the DC in conjunction with the toroidal magnetic field (see Sec. 1.7) is to measure the momentum of charged final-state particles that leave the target. For the most part, the rest of the CLAS detector is used to obtain accurate timing and particle identification. In particular, a photon tagger, specific to Hall B *photon runs* as discussed in Sec. 1.4, is used to measure the energy of photons incident on the target. In addition, there are several beam intensity and dispersion measuring devices used as described in Sec. 1.3.

The CLAS detector, shown in Figs. 1.3, 1.4 and 1.5, consists of six segments in ϕ (angle about the beam line) called *sectors*, each of which cover approximately $\frac{3}{4}\pi$ radians in θ (angle from beam line). Each of the six segments consists of a scintillator start counter (ST), three layers of drift chambers (DC), a gas Čerenkov counter (CC), a series of scintillator "time-of-flight" (TOF) counters and an electromagnetic calorimeter (EC). There is a toroidal magnetic field concentrated in the middle DC layer which bends charged particles toward or away from the beam line. This field geometry forces the particles to trace a path lying on a plane which allows for a simplified reconstruction algorithm. However, an

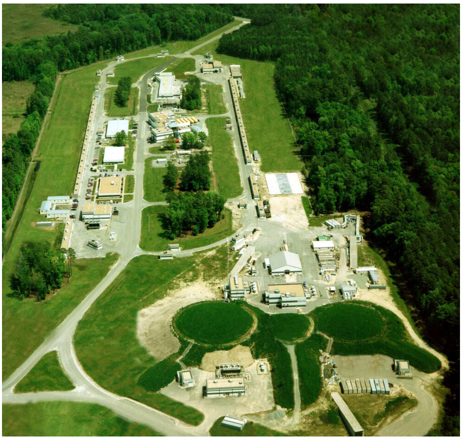

Figure 1.1: Aerial view of Jefferson Laboratory (JLAB) facing east. Image source: [23].

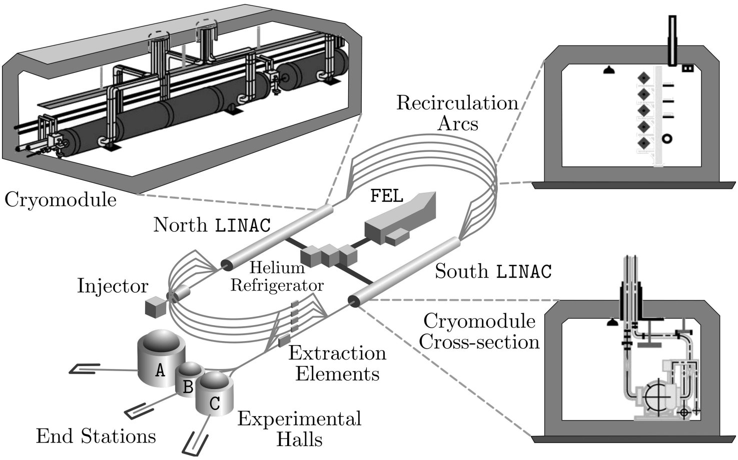

Figure 1.2: The Continuous Electron Beam Accelerator Facility[22] (CEBAF) at Jefferson Laboratory (JLAB) showing cross-sections of the linear accelerator (LINAC) halls and the recirculation arcs. Also depicted are the Free Electron Laser (FEL) and the helium refrigerator and distribution facility. Image source: [23].

asymmetry in the acceptance of oppositely charged particles is created.

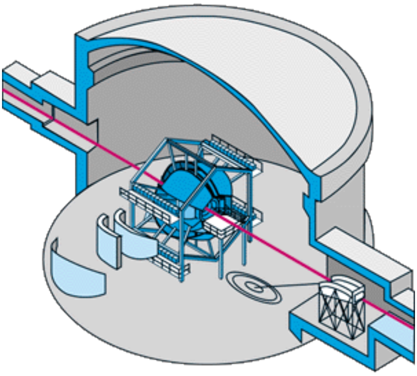

Figure 1.3: Schematic of the CLAS detector[21] in Hall B at JLab. The detector is approximately 8 meters in diameter. The beam, indicated by the red line, enters the hall from the lower right and passes through the tagger where the electrons are bent toward the beam dump in the floor and the photons continue to the target. Image source: [23].

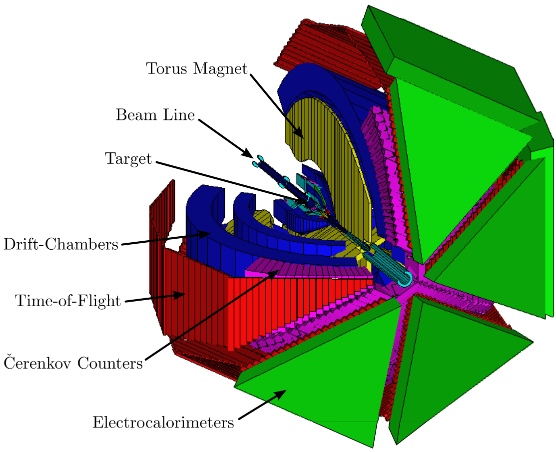

Figure 1.4: Schematic of the CLAS detector[21] with subsystems identified. This view is looking up-stream and the beam enters from the upper left. The detector is approximately 8 meters in diameter. Image source: [23].

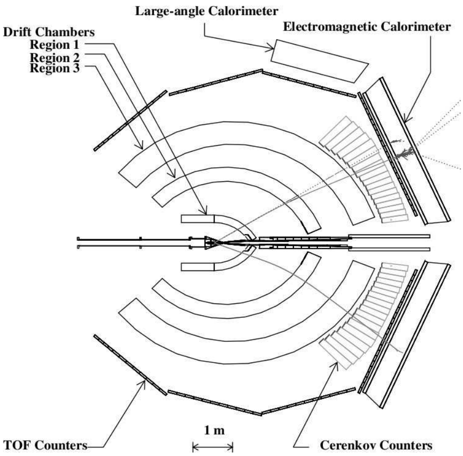

Figure 1.5: A cross section view of the CLAS detector showing an event with two tracks emanating from the target. Image source: [23].

1.1 *g12* Proposals and Running Conditions

Three CLAS analysis proposals (04-005[24], 04-017[25] and 08-003[26]) defined the experimental and theoretical basis for the *g12* running period. The 04-005 experiment, *Search for New Forms of Hadronic Matter in Photoproduction*, also called HyCLAS, had a meson spectroscopy focus with multiple charged particle final states such as

$$\begin{aligned}
\gamma p &\rightarrow p\pi^+\pi^-\pi^0, && (1.1)\\
\gamma p &\rightarrow n\pi^+\pi^+\pi^-, && (1.2)\\
\gamma p &\rightarrow pK^+K^-\eta, && (1.3)\\
\gamma p &\rightarrow nK^+K^+\pi^-, && (1.4)\\
\gamma p &\rightarrow \Delta^{++}\eta\pi^-, && (1.5)\\
\gamma p &\rightarrow pp\bar{p}. && (1.6)
\end{aligned}$$

The physics involved with HyCLAS required the configuration of CLAS to provide the largest acceptance for these multiple particle final states. Phase-space generated events of $\gamma p \rightarrow p\pi^+\pi^-\pi^0$ were simulated (see page 30 of [24]) with the t-slope obtained from the *g6c* experiment. The primary requirement for the greatest acceptance of such events was to have the target up-stream (see Sec. 1.5) of the normal position at the "center" of CLAS. This target placement gave better acceptance for particles close to the beam-line but sacrificed large momentum-transfer events where the final state particles were more than about 70° away from the beam-line.

The 04-017 experiment, *Study of Pentaquark States in Photoproduction off Protons*, also called Super-G, was founded on a search for the Θ^+ and Ξ^{--}, so-called *penta-quarks*, as well as a study of the "conventional" Ξ spectrum (see page 16 of [25].) This analysis is part of the latter topic. The running requirements were similar to that of HyCLAS with the need for a higher energy beam. An examination of the ground state Ξ^- reaction:

$$\gamma p \rightarrow \Xi^- K^+ K^+,$$

provides a starting point for this analysis. The threshold energy of the incident photon (E_γ) is given by

$$E_\gamma = \frac{m_\Xi^2 + 4m_K^2 + 4m_\Xi m_K - m_p^2}{2m_p}, \quad (1.7)$$

where m_Ξ is the mass of the Ξ, m_K is the mass of the K^+, and m_p is the proton (target particle) mass. For the ground state $\Xi(1320)$ which has a mass of 1.322 GeV, the threshold energy E_γ is 2.4 GeV. Since the beam (photon) and the target (proton) are both known quantities, we can measure the two kaons and calculate the Ξ^- through "missing mass" which is discussed in detail in Chapter 3. There is a minimum transverse momentum the final state particles must have to be measured by CLAS, otherwise they would travel right down the beam line. Therefore, in order to detect the two kaons with CLAS, a photon energy approximately 0.5 GeV above threshold is required. This corresponds to 2.9 GeV in the reaction for the ground state $\Xi(1320)$.

The third proposal, 08-003, titled *The* $\gamma p \to \pi^+ n$ *Single Charged Pion Photoproduction*, was approved just before the *g12* run period started. This was added onto *g12* as part of the physics to be done with the data collected. It required a single track trigger (see Sec. 2.2 on page 46) and lower current. This configuration allowed the data from these special runs to be included in analyses of the "production" *g12* data set.

At the beginning of *g12* run, approval came for purchasing gas for the Čerenkov subsystem of CLAS; see Sec. 1.8. The Čerenkov counters were filled and turned on two weeks into the running period enabling the separation of electrons from pions. As a result, a whole new set of leptonic physics became available in what was already a very rich data set.

1.2 Electron Accelerator

The CEBAF electron accelerator is able to deliver a 75% polarized electron beam of up to approximately 6 GeV to each of the three halls simultaneously. The beam as seen by each hall consists of clusters of electrons separated by approximately 2 ns. Typical intensities for halls A and C are 10–100 µA, however, due to the nature and sensitivity of the CLAS detector, beam currents to hall B are typically 10–100 nA.

Using a GaAs photocathode laser driven gun system, a highly polarized electron beam is produced and accelerated through a radio-frequency (RF) chopping system operating at 499 MHz. The three-beam, 1497 MHz "bunch train" at 100 keV is then longitudinally compressed and accelerated to just over 1% of the total machine energy before it is injected into the first main accelerator. This compression results in a beam of 2 ps bunches separated by 668 ps.

The main accelerator consists of a pair of linear accelerators (LINACs) which consists of twenty cryomodules each containing eight superconducting niobium cavities as shown in Fig. 1.6. This was the first use of superconducting cavities and marked a major advancement in the field of accelerators. Prior to the CEBAF breakthrough, typical accelerating cavities used non-superconducting metals like copper whose resistivity would cause a build up of heat. The niobium superconducting cavities are kept at 2 Kelvin and are non-resistive, eliminating the heating problems of copper. The significant cooling requirements are satisfied by the Lab's Central Helium Liquefier (CHL).

A standing electromagnetic wave is induced inside the niobium cavities as shown in Fig. 1.7 and the electrons passing through experience a continuous acceleration. Before CEBAF, the copper accelerating cavities used were tuned by adjusting the cooling system. The resistivity of the copper would cause the cavity to heat up and expand and the cooling system would be set so the desired length was obtained. The superconducting niobium cavities on the other hand

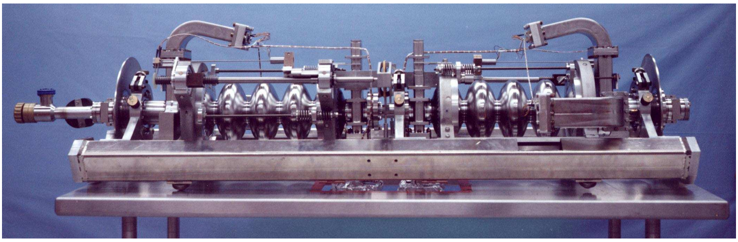

Figure 1.6: A superconducting niobium cavity pair. These devices are tuned for specific energy resonances by mechanically adjusting their lengths on the order of a few micrometers. Image source: [23].

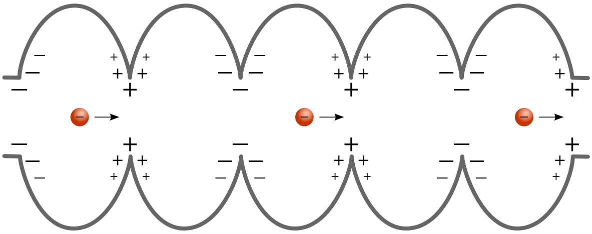

Figure 1.7: As the electron clusters travel through a superconducting niobium cavity, shown in Fig. 1.6, they experience a continuous acceleration due to a standing electromagnetic wave indicated by the positive and negative signs along the inner wall.

are non-resistive and do not heat up. Therefore, the cavities are lengthened or shortened mechanically (on the order of a few micrometers) to tune the wavelength and maximize the acceleration of the electrons.

The LINACs are connected by two sets of 180° magnetic-dipole bending arcs (see Fig. 1.2) with a radius of 80 meters. The beam is sent through both accelerators and is then *recirculated* up to four more times. Each LINAC is capable of accelerating the beam by up to 600 MeV giving approximately 1.2 GeV per pass. A plan to nearly double the energy of the beam was approved by DOE and the 12 GeV program started construction on September 15, 2008[27].

The beam is selectively extracted using RF cavities tuned to 499 MHz — the frequency dictated by the manufactured geometry. By slightly accelerating every third bunch, while not disturbing the other two, the electrons are bent out of the recirculating LINAC and sent to one of the halls. Each of the first four passes can be delivered to only one hall at a time, however the fifth (final) pass can be sent to all three halls simultaneously. The 499 MHz extraction creates the final beam as seen by the hall which consists of ~ 2 ps bunches separated by 2.004 ns. At the time of the *g12* experiment, the accelerator was capable of delivering a maximum electron beam energy of 5.7 GeV. The tagger subsystem (see Sec. 1.4) tagged photons of energies up to 95% of the delivered beam, and therefore the maximum energy photon seen in *g12* was 5.4 GeV.

1.3 Beam Measuring and Monitoring

There are several beam monitoring stations inside Hall B before and after the CLAS detector. Most of these are used by the accelerator group to steer the beam to the target as they control all magnets that can substantially move the beam. Other devices are used to measure the position, flux and dispersion of the beam. Upstream of CLAS there are two beam position monitors (BPMs) placed before the tagger. These are used to measure the transverse location of the electron beam and its intensity. This information is used as feed back for the steering mechanism.

There are also two *harp* devices located before the tagger that are used to measure the size of the electron beam; such a measurement for *g12* is shown in Fig. 1.8. The harp devices consist of fine wires (20 and 50 µm W and 100 µm Fe) that pass through the beam at specific orientations to obtain a horizontal (x) and vertical (y) profile. Since this process is invasive, it was only done when the drift-chambers and DAQ were turned off.

A few meters downstream of the target is the Total Absorption Shower Counter (TASC) which is used to measure the photon flux. The TASC, consists of four lead glass blocks, covering the entire beam, each instrumented by a photo-multiplier tube (PMT) and having approximately 100% photon detection efficiency at beam currents less than 100 pA[28, 29]. Using these counters, *normalization runs* of low current (50 pA, see Table 2.3) were taken several

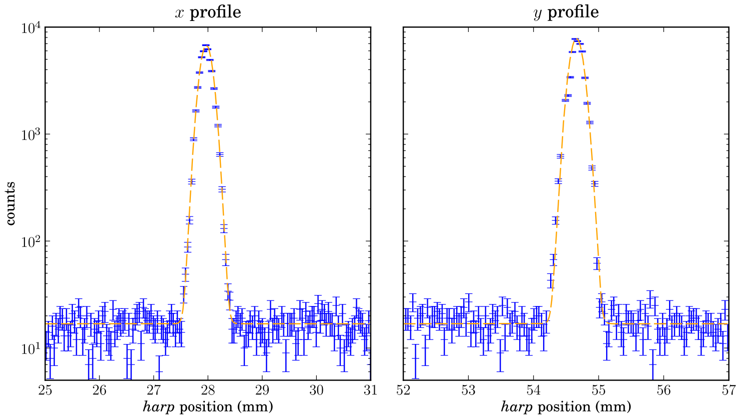

Figure 1.8: A typical *harp* scan done just prior to run 56426. Shown are the x and y profiles of the electron beam just before the tagger. The dashed orange line is a Gaussian fit to the data: $\sigma_x = 0.115$ mm and $\sigma_y = 0.105$ mm.

times throughout *g12*. In this way, the tagger was calibrated to measure the flux for the entire run period.

1.4 Radiator and Electron Tagger (TAG)

CLAS can use the electron beam as it is delivered from CEBAF by sending it directly to the target. There are a number of experiments which use the electron beam in this fashion. For example, a series of experiments called Deeply Virtual Compton Scattering (DVCS) is currently on-going[30], however, the detector is also capable of producing a beam of *real photons* by passing the electrons through a radiator. This causes the electron beam to emit photons via *bremsstrahlung* radiation. The electrons are subsequently bent out of the way by a dipole magnet and the photons continue on to the target. This is known as *photon running* with CLAS and a typical reaction studied looks like

$$\gamma p \to p\pi^{+}\pi^{-}. \tag{1.8}$$

Knowing the incoming electron's energy, the photon's energy can be determined by measuring the momentum of the electron after it has emitted the photon. The electrons are then bent by a dipole magnet and the energy and timing of individual electrons are recorded by the tagger counters[28] (TAG) while the photons continue to the target. In the *g12* experiment, there were usually many "hits" in the tagger for each event. Normally, the one associated with the photon that caused the event could be obtained by a timing coincidence with the tracks, though there are cases when this photon is ambiguous as discussed in Sec. 3.4.

The *g12* experiment was a *photon run* with an electron beam energy of 5.7 GeV meaning that the tagged photon energy ranged from 1.2 to 5.4 GeV. The radiator used was a gold foil 10^{-4} radiation lengths thick. The photons passed through a 6.2 mm diameter collimator 527 cm before they entered the target which had a radius of 2 cm.

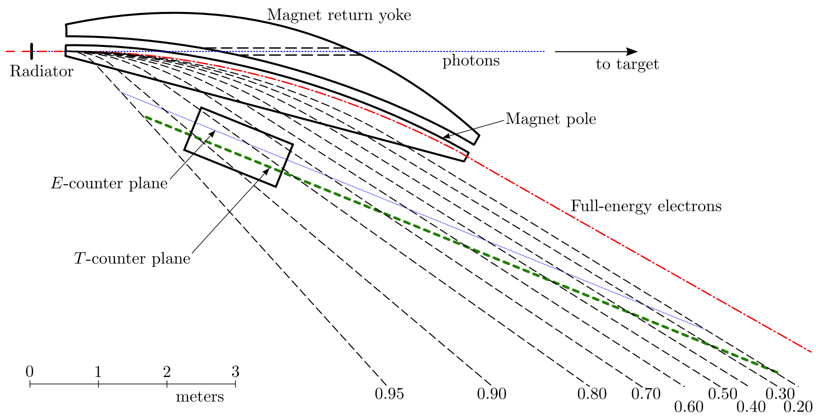

Figure 1.9: Scale drawing of the photon tagger system. The electron beam enters from the left and passes through the radiator where a few electrons emit photons via *bremsstrahlung*. The electrons that don't, follow the dash-dot red line to the tagger beam-dump. The electrons that lose energy (black dashed lines) get directed by the dipole magnet to the E-counter and T-counter planes and the photons continue to the target. The tagging range for the photons is 20% to 95% of the beam energy incident on the radiator. The rectangle around the E and T-counter planes outlines the expanded view shown in Fig. 1.10.

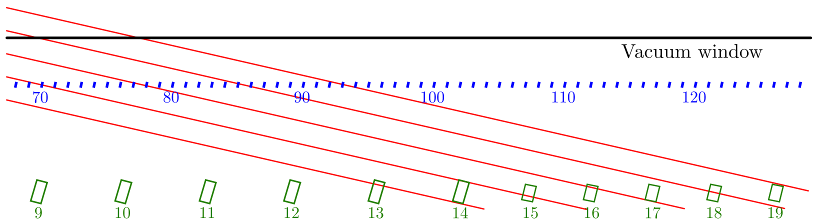

Figure 1.10: Scale drawing of the E-counters (upper plane of counters in blue) and the T-counters (lower plane of counters in green) showing examples of incident electrons (red lines) entering from the upper left. This view corresponds to the rectangle in Fig. 1.9. Notice how both sets of counters overlap, providing fine segmentation and hermetic coverage. The T-counters each consist of two PMTs (*left* and *right*) which are averaged together to obtain the time of the hit. The resolution produced by this setup, crucial for missing mass calculations, is determined by the size and overlap of the E-counters as discussed in Sec. 2.3.2.

1.5 Hydrogen Target

The target used by *g12* was a cylindrical liquid hydrogen (ℓH_2) cell made of Kapton 40 cm in length. The cell was 2 cm in radius while the photon beam had a radial size of approximately 1.5 cm as it *exited* the target. Several experiments prior to *g12* used this same target which could be filled with a number of different materials such as deuterium or helium. The target cell as shown in Fig. 1.11 is a simple container design and there is no polarization of the target material.

1.5.1 Position of the Target for *g12*

The typical position of the target for a given experiment with CLAS is at what was called the "center of CLAS." This is a well defined point inside region one of the drift-chambers. With the midpoint of the target cell placed at the center of CLAS, the geometric acceptance begins at about 8° from the beam-line in the lab frame. This configuration optimizes the detection of large angle tracks and is ideal for low energy runs at or below 4 GeV. As discussed on page 24, the target for *g12* was placed 90 cm upstream of CLAS center which yielded a geometric acceptance starting at approximately 6° from the beam-line. This enabled the optimization of CLAS for small angle track detection.

This placement was not without its drawbacks. Acceptance for large angle tracks was reduced from approximately 140° to 100° in the lab frame, and the drift-chamber resolution was decreased due to the oblique angle the tracks made with the detector planes. The geometric acceptances at large angles decreased in the same way for each subsystem, and the final acceptances in the laboratory frame are shown in the next few sections.

Figure 1.11: The 40 cm long cylindrical Kapton target cell used for *g12*. Image source: [23].

1.6 Start Counter (ST)

The first incarnation of CLAS in 1996 had a three segment start counter, each covering two sectors. The data acquisition (DAQ) system at that time had a maximum rate of less than 1 kHz which limited the beam current the detector could handle. Therefore, the hit rate in the start counter was low and the triggering was efficient enough to allow only a few false events. As time went by, the DAQ became more efficient and by 2005 the maximum handling rate was ~ 5 kHz. This rate was high enough to cause this start counter to act as an open gate in the trigger.

Youri Sharabian, a JLAB staff scientist with Hall B, designed and built a new 24-segment start counter[31] (ST) in 2006. It was first used with the *g10* experiment[32] and it provided better timing and spatial resolution (see Sec. 2.3.2) as well as the ability to handle much higher beam currents.

The new start counter, shown in Fig. 1.12, consists of 24 scintillation paddles which surrounds the 40 cm target hermetically within the acceptance of the drift-chambers. There are four paddles for each sector and two different paddle shapes. The start counter is capable of approximately 350 ps timing resolution making it useful to identify the hit in the tagger associated with the event. The segmentation allows for event rates that approach the tagger and DAQ limits.

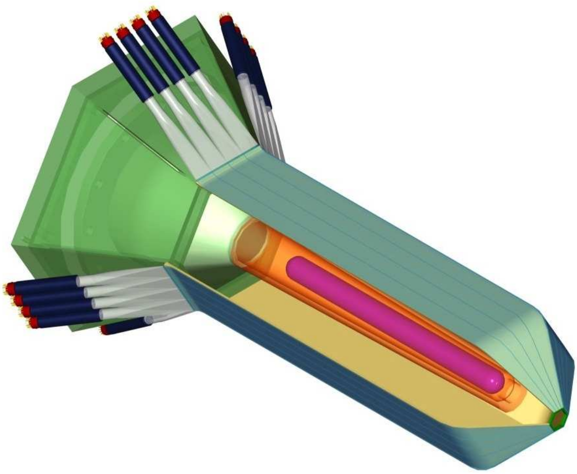

Figure 1.12: Schematic of the start counter (ST) with the 40 cm long target cell (purple) at the center. The beam enters from the upper left of the figure. Image source: [23].

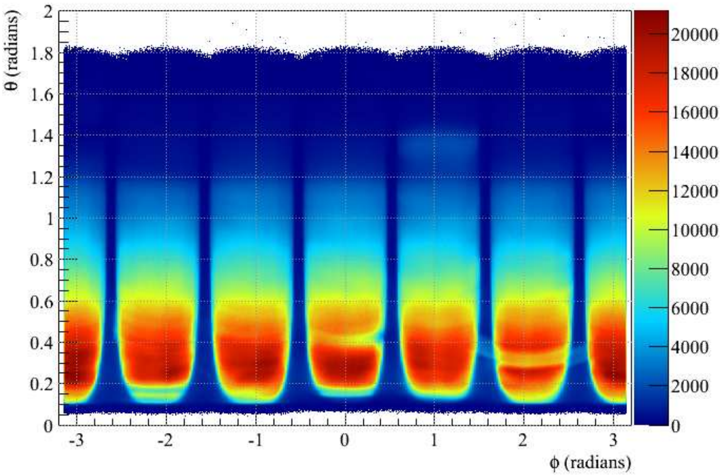

Figure 1.13: Angular coverage in the lab frame of the tracks that had an associated start counter hit showing that the ST covered the entire DC/TOF acceptance region which is shown in Fig. 1.22.

1.7 Drift Chambers (DC)

The primary subsystem of the CLAS detector is a collection of multi-wire proportional drift-chambers[33] (DC) consisting of three layers in each of six sectors as shown in Fig. 1.4. There is a toroidal magnetic field encompassing the middle layer which causes the charged particles to bend either directly toward or away from the beam-line. The magnetic field at regions 1 and 3 (inner and outer layers respectively) is relatively weak compared to region 2 as shown in Fig. 1.14. Therefore, the bending of the tracks is concentrated inside region 2 of the DC and the charge and momenta of the particles are determined by measuring the deflection angle of the tracks.

Each region of the DC consists of two *superlayers* which contain six layers of evenly spaced 20 μm gold-plated tungsten *sense wires* each surrounded by six 140 μm gold-plated aluminum alloy *field wires*. The very first superlayer (region 1, superlayer 1) has only 4 layers due to space constraints. The field wires were kept at a high negative voltage (approximately -1.5 kV) while the sense wires were kept at a moderate positive voltage.

The gas used in the DC is 90% argon and 10% carbon-dioxide which is a non-flammable mixture that ionizes easily when charged particles above a certain energy pass through it. The ionized electrons cascade and drift toward the sense wires creating a signal that is amplified and passed through amplifier-discriminator boards (ADBs) and recorded by time-to-digital converters (TDCs). Due to budget considerations, there were no analog-to-digital (ADC) signals recorded from the DC. This could have provided information on the par-

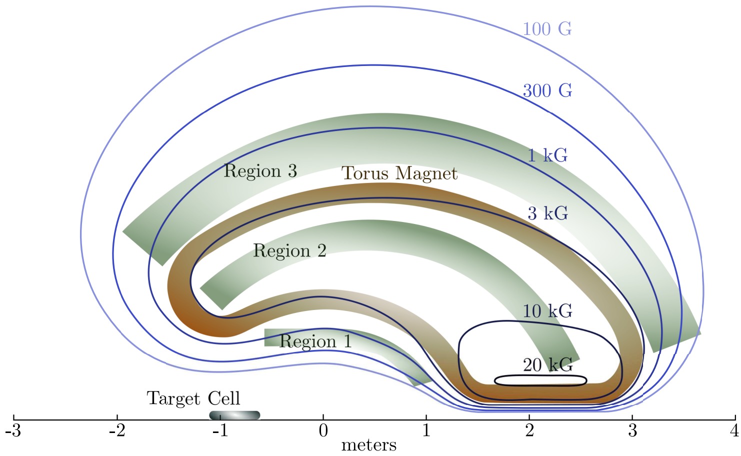

Figure 1.14: Cross-section of the toroidal magnetic field at half current (1930 A). For *g12*, the direction of the field was into the page and the 40 cm target center was placed at -90 cm from the CLAS center. Region 2 of the DC is located inside the region of the coils shown as the kidney shaped loop at about 3 kG.

ticles' energy loss as it traveled through the chambers, however, energy loss through other systems such as the TOF was available and used in this analysis, as discussed in Chapter 3.

1.7.1 Superconducting Toroidal Magnet

The toroidal magnetic field used in CLAS is created by six kidney-shaped superconducting current loops[21] which are placed between the six sectors of the drift-chamber (DC) as shown in Fig. 1.4. They each consist of 4 layers of 54 windings of aluminum-stabilized NbTi/Cu superconductor.

During the *g12* experiment, the magnets operated at a half-capacity current of 1930 A corresponding to a maximum field of about 20 kG. The magnetic field around the target area was low enough to allow for polarizing the target material though the *g12* target was unpolarized. The field was oriented such that positively charged particles bent away from the beam line, maximizing acceptance for these tracks. Increasing the current would improve the resolution of the detector, but sacrifice the acceptance for negatively charged particles. Since the physics goals of the *g12* proposals (see page 24) involved many final state particles, both positive and negative, this balance of resolution and acceptance was used.

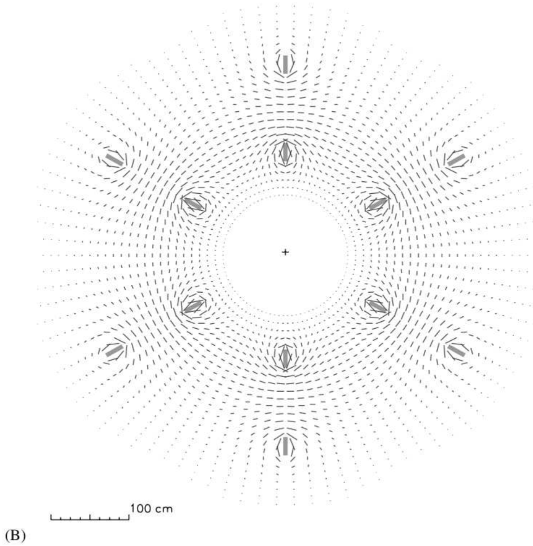

Figure 1.15: Toroidal magnetic field line diagram looking down-stream toward the CLAS detector. The field inside the windings indicated by the gray rectangles is in the counter-clockwise direction, and the field strength is concentrated in the region between the coils, see Fig. 1.14. Image source: [23].

1.8 Čerenkov Counters (CC)

The *gas* Čerenkov counters (CC), indicated in Fig. 1.4, occupies the space between the drift-chambers and the time-of-flight counters in each of the six sectors. They are divided into 18 segments (shown in Fig. 1.16) in the polar angle, θ, away from the beam line. These segments are designed to focus Čerenkov-light emitted from particles originating from the center of CLAS. The coverage in θ is approximately 8° to 45° for tracks originating from the center of CLAS. Because the target was placed 90 cm upstream, the polar coverage was in the range from 6° to 35° in the lab frame.

The gas used in the CC is perfluorobutane (C_4F_{10}) with an index of refraction of 1.00153. The charged pion threshold for this detector is approximately 2.7 GeV, while the threshold for electrons is 9 MeV. Thresholds for kaons and protons are much higher than the maximum beam energy for *g12* and were therefore not detected in the CC. The detecting efficiency for electrons is $> 97\%$ and this detector enabled the distinction between pions and electrons below approximately 2.5 GeV.

The use of the CC was not included in the original proposals, however a significant drop in price on C_4F_{10} just prior to the start of *g12* allowed the gas to be added at the last minute. The price drop was due to the recent availability

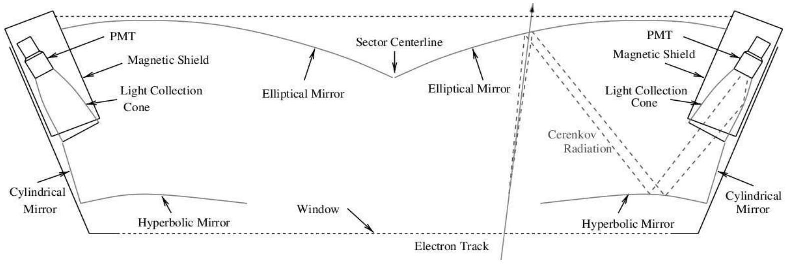

Figure 1.16: Diagram of one segment of the Čerenkov counters with an electron entering from the bottom. Image source: [23].

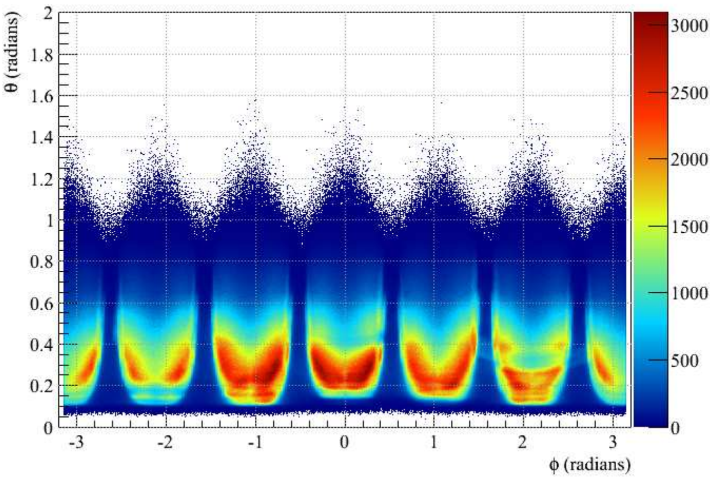

Figure 1.17: Angular coverage in the lab frame of the tracks that had an associated Čerenkov counter hit.

of another, much cheaper gas that was demonstrated to have the same general properties as C_4F_{10}.

1.9 Electromagnetic Calorimeters (EC)

The final layer of CLAS is the electromagnetic calorimeter (EC)[34], shown in Fig. 1.4. It consists of alternating layers of lead and scintillator. The overall shape is an equilateral triangle and each layer of scintillator consists of 36 strips as shown in Fig. 1.18. The EC is divided into an *inner* and *outer* section where the energy deposited from incident tracks is recorded separately.

The *inner* layer consists of 8 *logical* layers of lead and scintillator while the

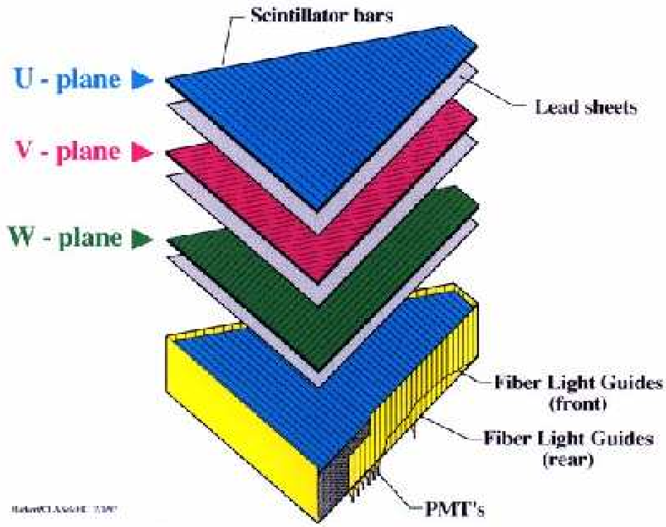

Figure 1.18: Separated view of one sector of the forward electromagnetic calorimeter (EC) showing the three planes (u, v, w) of scintillator-lead pairs which make up one of the 13 *logical* layers. Image source: [23].

outer layer consists of 5. Each *logical* layer is made of three scintillator-lead layer pairs where the scintillator strips are turned 120° from each other, labeled u, v and w. There are a total of 39 scintillator-lead layer pairs in each sector of the EC. The angular acceptance of the EC is shown in Fig. 1.19. Notice that it covers the entire Čerenkov (Fig. 1.17) acceptance region.

The lead to scintillator thickness ratio (0.2) was chosen so one third of the showering particle's energy is deposited into the scintillator. Using the three layers in each *logical* layer to provide pixel-like information, the transverse shower development for a given particle can be determined. The difference in energy deposit between the *inner* and *outer* layers provides separation of electrons from pions in the reconstructed data. For this analysis, the EC was used as a secondary time-of-flight measurement as well as an energy loss determination which provided additional information on particle identification. Furthermore, all final-state photons were identified in the EC by a signature that consisted of a hit only in the first layer of scintillators since the photons are absorbed in the leading sheet of lead.

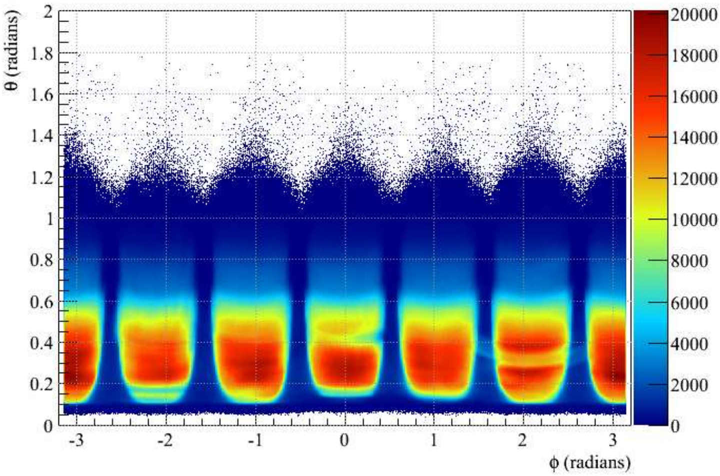

Figure 1.19: Angular coverage in the lab frame of the tracks that had an associated electromagnetic calorimeter hit.

1.10 Time-of-Flight Detectors (TOF)

Accurate measurement of the speed of the final state particles, as discussed in Sec. 2.3.2, is challenging. Because of their relatively low momentum, typically 1–2 GeV, the particles travel slow enough that the time it takes them to reach the time-of-flight[35] (TOF) counters is significant. It is thanks to the fine timing resolution of CLAS that enables the TOF to provide the particle identification used in this analysis.

The TOF consists of six outer shells, one of which is shown in Fig. 1.20, of 57 scintillator paddles. The paddles are grouped physically into four *panels*. The paddles are all 5.08 cm (2 inches) thick but are of varying lengths and each has a PMT attached to both ends. This provides close to 100% efficiency of minimum ionizing particles and a timing resolution of 150–200 ps as discussed in Sec. 2.3.2. The TOF detector was used in the level 1 trigger (see Sec. 2.2) for *g12* to identify “prongs” or track candidates. Also, the ADC signals from the TOF were used to measure the energy deposit of the tracks to assist in particle identification in Sec. 3.5.

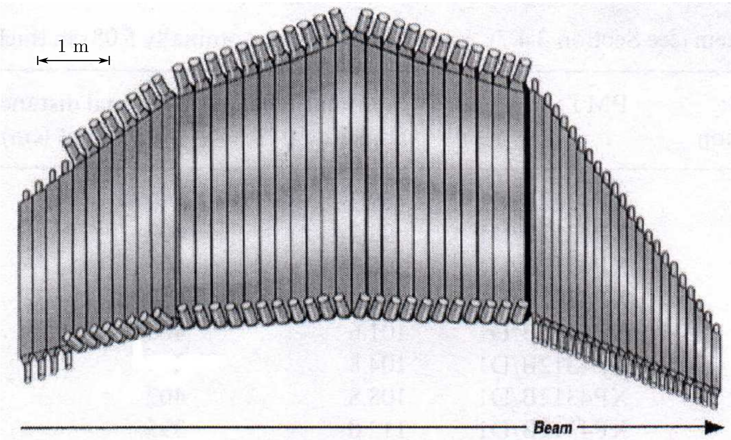

Figure 1.20: Diagram of one sector of the time-of-flight (TOF) paddles. There are 57 scintillator paddles covering the entire acceptance region of the drift-chambers for each sector. Image source: [23].

Figure 1.21: The CLAS detector during a maintenance period where the time-of-flight "shell" (left) was pulled back from the drift-chambers (DC, right). The beam line enters from the lower right on the other side of the DC. The TOF paddles seen are the two center *panels* shown in Fig. 1.20 for three of the CLAS sectors. Image source: [23].

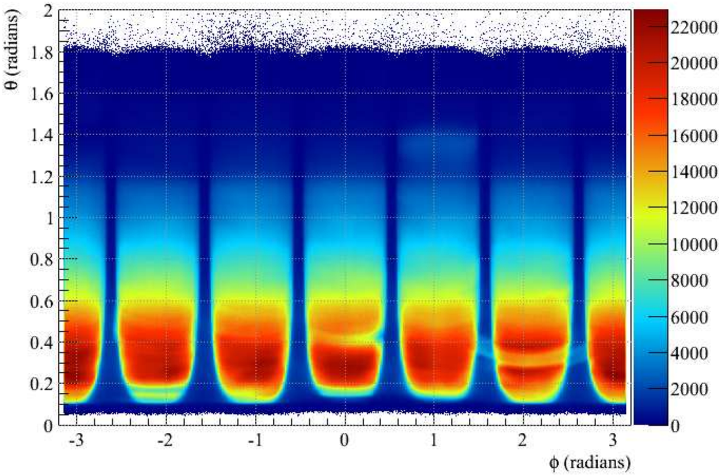

Figure 1.22: Angular coverage in the lab frame of the tracks that had an associated time-of-flight hit. This can be interpreted as the total drift-chamber coverage of the CLAS detector.

1.11 Data Aquisition System

The data acquisition system for the CLAS detector is composed of several layers of electronics. The amplified signals from the various wires and photo-multiplier tubes are received by the TDC and ADC counters. A certain set of these signals are used in the *trigger* to determine if an event of interest has occurred. If it has, then all the signals are sent to the "event builder" via CAMAC[21] crates and recorded as a single event.

The controlling program makes use of the CEBAF On-line Data Acquisition System (CODA)[21]. At the time of the *g12* experiment, the DAQ was capable of over 10 kHz. This high rate was due in part to a new field-programmable gate array FPGA logic control processor that was integrated into the trigger system for CLAS[36].

The input components to the triggering system of CLAS are obtained from the tagger, time-of-flight, start counter, electromagnetic calorimeter and Čerenkov counters. The TOF and ST are used to identify "prongs," or charged tracks, at the trigger level. These composed by a coincidence of any one TOF hit in a given sector with any one ST hit in the same sector. Additionally, a coincidence between the EC and CC above certain thresholds was included as a lepton trigger. The various trigger *bits* used by the system are discussed in Sec. 2.2.

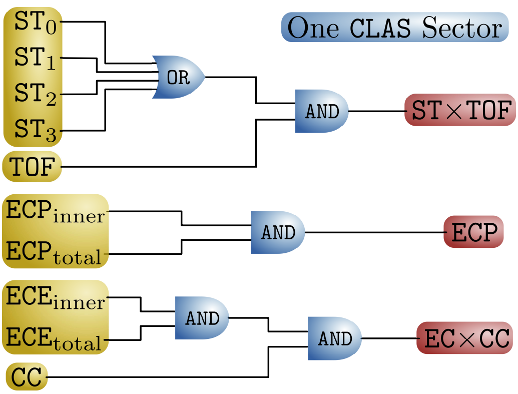

Figure 1.23: Trigger logic for one of the six sectors of CLAS. The ST×TOF signal is a coincidence between any of the four start counter TDC signals (numbered from 0 to 3) and any of the 57 TOF TDC signals. The ECE$_{\text{inner}}$ and ECE$_{\text{total}}$ are the *electron*-threshold EC signals for the energy deposited in the *inner* layer and in *all* layers. These are combined with a CC signal to produce the EC×CC trigger for this sector. The ECP trigger signal is the *photon*-threshold EC signal. These trigger signals are discussed further in Sec. 2.2.

Chapter 2

g12 Data Acquisition & Reconstruction

A raw event collected by the data acquisition (DAQ, see Sec. 1.11) consisted of many hundreds of "hits" corresponding to signals from the detector that were strong enough to be recorded, that is, above a certain threshold. The hits paired detector element identification numbers with either an ADC or TDC value. These were converted to manageable units in energy for ADCs, time for TDCs and sector/wire number for the element IDs. After that, these hits were grouped into "clusters" which eventually represented measured particles that had traveled through the detector. This process, called *reconstruction*, is detailed in the following sections and starts with the definition of the "trigger" that told the DAQ to record an event.

The *main production trigger* used by the *g12* experiment was a coincidence of two charged tracks in different sectors and at the same time as a tagged photon above 4.4 GeV. These tracks were identified at the trigger level by the coincidence of a start counter hit and a time-of-flight hit in the same sector as identified by "ST$\times$TOF" in Fig. 1.23. With an electron beam current of 60–65 nA, the DAQ rate was approximately 8 kHz with the two-track trigger contributing approximately 5.5 kHz to this total. All trigger *bits* used during *g12*, numbered 1–12, can be found in Tables 2.4, 2.5 and 2.6.

Several lower-rate triggers were used in addition to the main production trigger. Of special note was bit 6: a single lepton in coincidence with a single charged track. This trigger matched hits in the electromagnetic calorimeter with the Čerenkov counter, both above certain thresholds as discussed below. It is designated by "EC$\times$CC" in Table 2.5, and overlapped with the production trigger adding approximately 1 kHz to the DAQ rate. Also of note, bit 12 was a three-track coincidence without requiring an in-time tagger hit (see Sec. 1.4) contributing an additional 1 kHz.

The *g12* experiment incorporated several runs which consisted of lower current ($\sim$ 24 nA), single track triggers. These were part of a late proposal led by the Duke University group[26] as discussed in Sec. 1.1 on page 24. Also, Several calibration and normalization runs were taken throughout the experiment as shown in Table 2.3. For this analysis, these were used largely for alignment corrections and the total photon flux determination.

The raw data recorded from the `CLAS` detector consisted of `ADC` and `TDC` signals from the individual elements of each subsystem. The data also included scalar values from the accelerator such as the `RF` clock, which had the best timing resolution of all signals. Reconstruction of tracks from these element hits started by spatially grouping the drift-chamber (`DC`) hits into *hit-based* candidate tracks and then refining these using the timing from the start (`ST`) and time-of-flight (`TOF`) counters. Particle identification was then done on these tracks by several means including mass determination and energy deposit as discussed later in this chapter. Neutral particles that did not fire the `DC` (photons, for example) were identified by certain signatures in the electromagnetic calorimeter (`EC`), though the efficiency for detecting neutral particles was much lower than for charged particles.

The tracks which were the result of reconstruction consisted primarily of momentum and vertex information. Timing from the `TOF` and `ST` were used during analysis to fine-tune the particle identification. This chapter discusses the reconstruction of tracks from raw data, the resolution of the momenta and timing information, and finally, a technical itemization of the variables used in the analysis of this work, and their inter-relationships.

2.1 Run Summary

The *g12* experiment is divided into several "runs," each consisting of approximately 50 million triggers. Calibrations were largely determined and applied based on run number or a specific range of runs. Table 2.1 contains a list of the runs that had at least 1M triggers and were reconstructed successfully, along with the current of the beam for these runs. Table 2.2 shows a list of the single-sector runs taken throughout the *g12* running period. Data from these runs represent approximately 97% of the production running period of *g12*. There were many diagnostic runs that were not recorded. Most of these involved testing the `DAQ` system, however, the run number still incremented for each of these. Further complicating matters, several files did not have adequate information for the reconstruction process due to hardware failures during periods where the `DAQ` was active and data was being written to disk — wire tripping in the `DC`, for example. In the end, the *g12* experiment consisted of 622 "good" runs starting with 56363 and ending with 57317.

Table 2.1: List of successfully reconstructed production runs and their beam currents in nA.

runs	current (nA)	runs	current (nA)	runs	current (nA)
56363	20	56605	60	56900-56908	60
56365	30	56608-56612	60	56914-56919	60
56369	30	56614-56618	60	56921-56922	60
56384	5	56620-56628	60	56923	65
56386	20	56630-56636	60	56924	70
56401	50	56638-56644	60	56925	80
56403	70	56646	60	56926-56930	60
56404	60	56653-56656	60	56932	60
56405	50	56660-56661	60	56935-56940	60
56406	40	56665-56670	60	56948-56956	60
56408	80	56673-56675	60	56958	60
56410	90	56679-56681	60	56960-56975	60
56420-56422	5	56683	60	56977-56980	60
56435	5	56685-56696	60	56992-56994	60
56436	15	56700-56708	60	56996-57006	60
56441	35	56710-56724	60	57008-57017	60
56442	30	56726-56744	60	57021-57023	60
56443	20	56748-56750	60	57025-57027	60
56445-56450	60	56751-56768	65	57030-57032	60
56453-56459	60	56770-56772	65	57036-57039	60
56460-56462	70	56774-56778	65	57062-57069	60
56465	70	56780-56784	65	57071-57073	60
56467-56472	70	56787-56788	65	57075-57080	60
56478-56483	70	56791-56794	65	57095-57097	60
56485-56487	70	56798-56802	65	57100-57103	60
56489-56490	70	56805-56815	65	57106-57108	60
56499	70	56821-56827	65	57114-57128	60
56501	60	56831-56834	65	57130-57152	60
56503	57	56838-56839	65	57159-57168	60
56504	56	56841-56845	65	57170-57185	60
56505-56506	40	56849	65	57189-57229	60
56508-56510	60	56853-56862	65	57233-57236	60
56513-56517	60	56864	65	57249-57253	60
56519	60	56865-56866	60	57255-57258	60
56521-56542	60	56870	65	57260-57268	60
56545-56550	60	56874-56875	60	57270-57288	60
56555-56556	60	56877	60	57290-57291	60
56561-56564	60	56879	60	57293-57312	60
56573-56583	60	56897-56898	60	57317	60
56586-56593	60	56899	65		

Table 2.2: A list of the single-sector runs using the trigger configuration described in Table 2.6.

run	current (nA)	run	current (nA)
56476	24	56910	35
56502	24	56911	30
56520	24	56912	25
56544	24	56913	24
56559	24	56933-4	24
56585	24	56981-3[a]	24
56619	24	56985[a]	15
56637	24	56986	15
56663-4	24	56989	24
56697	24	57028	24
56725	24	57061	24
56747	24	57094[b]	24
56769	24	57129	24
56804	24	57155-6	24
56835	24	57237-8	24
56869	5		

[a]No Level-2 trigger was used for runs 56981-56985
[b]A shorter `ST ADC` gate was implemented starting with run 57094.

In addition to the production data taken, there were several special *calibration* runs which are listed in Table 2.3. These consisted of normalization, zero-field, and empty-target data. The normalization runs were used to calibrate the tagger for the measurement of the total photon flux and there were two specific runs for the left and right `TDC` signals of the tagger to check for consistency. The zero-field data was taken with the main torus magnet off. This meant that the particles traveled in straight lines through the drift-chamber which made track reconstruction simple and accurate. Though their momenta were unknown, these tracks were used to account for the position and orientation of the drift-cambers in the reconstruction. Finally, the empty target run was used to investigate the contributions of the target wall to the data sample.

Table 2.3: List of special calibration runs done during the *g12* experiment.

run	current (nA)	description
56397	0.05	normalization
56475	10	zero-field

continued on next page.

continued from previous page.

run	current (nA)	description
56511	0.05	normalization, tagger TDC-left
56512	0.05	normalization, tagger TDC-right
56584	0.05	normalization
56682	0.05	normalization
56790	0.05	normalization
56931	0.05	normalization
56947	0.05	normalization
57169	0.05	normalization
57239	24	empty-target, single-sector
57241	80	empty-target, production
57248	0.05	normalization

2.2 Trigger Configuration

The *g12* experiment was the first Hall B run-period to implement field programmable gate array (FPGA) processors to handle the trigger logic of the CLAS detector (see Sec. 1.11). With this new FPGA-powered triggering system, came the ability to modify the trigger quickly during the experiment. While potentially dangerous — these changes must be accounted for in total-cross-sectional analyses for example — this allowed the group to tune the trigger to get the highest possible rate of physical events.

The trigger bits used during the *g12* running period are defined in Tables 2.4, 2.5 and 2.6. They generally consisted of a number of tracks which were the coincidence of any one of the four start counter paddles and any of the 57 time-of-flight paddles in a given sector as discussed in Sec. 1.11. The hardware and configuration did not allow triggering on two tracks in the same sector because there were only six signals coming from the TOF — one for each sector. The coincidence of these tracks with the photon tagger, called the "Master-OR," is defined in Table 2.7.

There were two sets of thresholds for the EC labeled *photon* and *electron*. These labels did not mean photon or electron specifically, but were considered a first-order approximation. The actual particle identification was done much later in the analysis of the reconstructed data. The thresholds for the CC and EC during the *g12* running period are shown in Table 2.8.

Table 2.4: Trigger configuration for *g12* runs from 56363 to 56594 and 56608 to 56647. $(\texttt{ST}\times\texttt{TOF})_i$ indicates a single *prong* which is a trigger-level track defined as a coincidence between a start counter and time-of-flight hit in the i^{th} sector or any sector if the subscript index, i, is not specified. An added $\times 2$ or $\times 3$ indicates the coincidence of multiple *prongs* which are not in the same sector. `MORA` and `MORB` represent coincidences with tagger hits within a certain energy range as specified in Table 2.7.

g12 runs 56363–56594, 56608–56647			
bit	definition	L2 multiplicity	prescale
1	$\texttt{MORA}\cdot(\texttt{ST}\times\texttt{TOF})_1\cdot(\texttt{ST}\times\texttt{TOF})$	–	1
2	$\texttt{MORA}\cdot(\texttt{ST}\times\texttt{TOF})_2\cdot(\texttt{ST}\times\texttt{TOF})$	–	1
3	$\texttt{MORA}\cdot(\texttt{ST}\times\texttt{TOF})_3\cdot(\texttt{ST}\times\texttt{TOF})$	–	1
4	$\texttt{MORA}\cdot(\texttt{ST}\times\texttt{TOF})_4\cdot(\texttt{ST}\times\texttt{TOF})$	–	1
5	$\texttt{MORA}\cdot(\texttt{ST}\times\texttt{TOF})_5\cdot(\texttt{ST}\times\texttt{TOF})$	–	1
6	$\texttt{MORA}\cdot(\texttt{ST}\times\texttt{TOF})_6\cdot(\texttt{ST}\times\texttt{TOF})$	–	1
7	$\texttt{ST}\times\texttt{TOF}$	–	1
8	$\texttt{MORA}\cdot(\texttt{ST}\times\texttt{TOF})\times 2$	–	1
11[a]	$\texttt{MORB}\cdot(\texttt{ST}\times\texttt{TOF})\times 2$	–	1
12	$(\texttt{ST}\times\texttt{TOF})\times 3$	–	1

[a] bit 11 and `MORB` were included in the trigger starting with run 56519.

Table 2.5: Trigger configuration for *g12* runs from 56595 to 56607 and 56648 to 57323. (EC×CC) represents a coincidence between the electromagnetic calorimeter and the Čerenkov subsystems within a single sector using the thresholds as described in Table 2.8. ECP represents the *photon* threshold trigger from the EC as detailed in Fig. 1.23. See Table 2.4 for other explanatory details.

g12 runs 56595–56607, 56648–57323			
bit	definition	L2 multiplicity[a]	prescale
1	MORA·(ST×TOF)	1	1000/300[b]
2	MORA·(ST×TOF)×2	2/–[c]	1
3	MORB·(ST×TOF)×2	2	1
4	ST×TOF	1	1000/300
5	(ST×TOF)·ECP×2	1	1
6	(ST×TOF)·(EC×CC)	2	1
7	MORA·(ST×TOF)·(EC×CC)	–	1
8	MORA·(ST×TOF)×2	–	1
11	(EC×CC)×2	–	1
12	(ST×TOF)×3	–	1

[a] Level 2 triggering was turned off on all bits for runs 56605, 56607 and 56647.

[b] Prescaling for bits 1 and 2 were 1000 for runs prior to 56668 at which point they both were changed to 300.

[c] Level 2 triggering of bit 2 was set to 2 for runs prior to 56665 at which point it was turned off.

Table 2.6: Trigger configuration for the single-sector runs of *g12*. Trigger bits 7–12 were not used for these runs. See Table 2.4 for explanatory details.

bit	definition	L2 multiplicity	prescale
1	MORA·$(\texttt{ST}\times\texttt{TOF})_1$	sector 1	1
2	MORA·$(\texttt{ST}\times\texttt{TOF})_2$	sector 2	1
3	MORA·$(\texttt{ST}\times\texttt{TOF})_3$	sector 3	1
4	MORA·$(\texttt{ST}\times\texttt{TOF})_4$	sector 4	1
5	MORA·$(\texttt{ST}\times\texttt{TOF})_5$	sector 5	1
6	MORA·$(\texttt{ST}\times\texttt{TOF})_6$	sector 6	1

Table 2.7: Master-`OR` definitions for *g12*. The `TDC` counters were used in the trigger and since each of these corresponds to several energy paddles, the energies given here are approximate. T-counter number 1 corresponds to the highest energy photon of approximately 5.4 GeV. Both `MORA` and `MORB` are referenced in terms of the trigger logic in Tables 2.4, 2.5 and 2.6. The *single-sector* runs are listed in Table 2.2.

	`MORA`		`MORB`	
run range	T-counters	energy (GeV)	T-counters	energy (GeV)
56363–56400	1–47	1.7–5.4	–	–
56401–56518	1–25	3.6–5.4	–	–
56519–57323	1–19	4.4–5.4	20–25	3.6–4.4
single-sector	1–31	3.0–5.4	–	–

Table 2.8: Threshold values for the electromagnetic calorimeter (`EC`) and Čerenkov counter (`CC`) during the *g12* running period. `EC` thresholds are shown as *inner/total*, and `CC` thresholds are shown as *left/right*.

`EC`		`CC`
photon	*electron*	
50/100 mV	60/80 mV	20/20 mV
150/300 MeV	180/240 MeV	∼0.4 photo-electrons

2.2.1 Trigger Efficiency Study

In the first few weeks of *g12*, during "commissioning," an attempt to determine the efficiency of the two-track trigger (bit 8 in Tables. 2.4 and 2.5) was made. The rate of this main production trigger rose quadratically with the beam current while the physical event rate increased linearly. The number of accidentals, which must be cut from any analysis, increased with increasing current and at a certain point, the majority of the events taken were accidentals. The trigger rate as a function of the beam current is shown in Fig. 2.1. An estimate of the linear part of the trigger rate shows that approximately 60% of the events recorded during the *g12* experiment (which ran at 60–65 nA beam current) were accidentals.

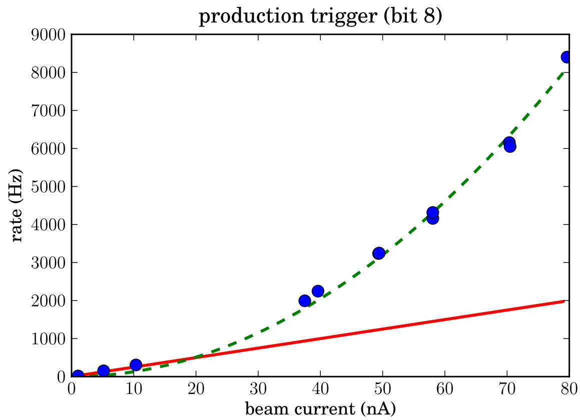

Figure 2.1: The production trigger rate (bit 8 in Tables 2.4 and 2.5) was measured for various beam currents shown by the blue dots. The rates below 10 nA are roughly linear and are extrapolated via the red solid line to show an estimate of the physical event rate. The actual trigger rate is fitted with a quadratic shown by the green dashed line. By this estimate, the accidental rate is shown to equal the physical event rate at approximately 40 nA. The *g12* experiment was done at 60–65 nA.

2.3 Calibrations

The raw data recorded from the CLAS detector consisted of timing and pulse-height information from the drift-chambers and counters. Timing from all the elements such as wires and PMTs were initially offset from each other. The alignment of these times was accomplished during the reconstruction (see Sec. 2.4) using a database that stored the corrections needed to produce timings that were relative to each other. The ADC pulse height was used by the start counter and time-of-flight to account for the propagation time of the signal, in this case light from the scintillator, to the PMT. Determining these corrections took us a year and three months with a team consisting of two JLAB staff scientists, three university professors, two post-docs and four graduate students as listed in Table 2.9. This huge amount effort was necessary due to the large extent of timing information from such a complex detector.

The general calibration procedure began by determining the timing offset of the systems associated with the event trigger which were the start counter, time-of-flight and tagger. Then, the drift chambers were calibrated for physical alignment and TDC alignment using the zero-field run. The tracks obtained from the DC, along with the ADC signals from the ST and TOF could then be combined

Table 2.9: The principal calibrators of the *g12* data set.

name	institution	position	systems and responsibilities
C. Bookwalter	FSU[a]	graduate student	TOF
P. Eugenio	FSU	professor	coordination
J. Goetz	UCLA[b]	graduate student	reconstruction
L. Guo	JLAB	post-doc	coordination
V. Kubarovsky	JLAB	staff scientist	coordination
M. Paolone	USC[c]	post-doc	EC, CC
J. Price	CSUDH[d]	professor	coordination
M. Saini	FSU	graduate student	RF, ST, TAG
D. Schott	FIU[e]	graduate student	DC
B. Stokes	GWU[f]	post-doc	DC
A. Vlassov	ITEP[g]	professor	CC
D. Weygand	JLAB	staff scientist	coordination
M. Wood	Canisius College	professor	EC

[a]Florida State Univ.
[b]Univ. of California Los Angeles
[c]Univ. of South Carolina
[d]California State Univ., Dominguez Hills
[e]Florida International Univ.
[f]George Washington Univ.
[g]Alikhanov Inst. for Theoretical and Experimental Physics

to determine the time-walk corrections which were used in subsequent iterations. This process would then be repeated several times until adequate resolutions in the various subsystems were achieved.

We started by aligning all the `TDC` signals from the scintillators "paddle to paddle" in the start counter, tagger and time-of-flight systems. Then, the timings of these systems as a whole were aligned to the radio-frequency time (`RF`) from the accelerator beam. This `RF` clock provided the most accurate timing information (approximately 50 ps resolution), and as a result, the likely-hood of choosing the electron in the tagger associated with the photon that interacted in the target to create the event was much greater.

After this initial calibration, several things took place in parallel. First, we determined the positions of the drift-chambers using the zero-field run where all tracks in the `DC` were straight. Secondly, the start counter and time-of-flight timings were corrected for *time-walk*. This accounted for the time it took from the physical passing of the particle through the scintillator to the final `TDC` signal that was recorded in the data stream. We used the magnitude of the `ADC` signal to determine the position of the track inside the scintillator paddle and obtained a correction to the `TDC` signal. Finally, the electromagnetic calorimeter and the Čerenkov detector signals were aligned in time.

Once this was accomplished, we went back to the alignment of the `TDC`s in the start counter, tagger and time-of-flight which led to another pass of the calibrations. Each of the steps above contained several iterations themselves. We performed four complete passes, as well as several others where only some systems were corrected, before the data were calibrated well enough to use for physics analysis.

2.3.1 Organization of Calibration Procedure

During the *g12* run, there were several hardware and software changes which required recalibration of the affected systems. These included changes such as the event trigger or cable lengths from the start counter. Each time a change was made, the subsequent runs were treated separately from the previous runs. A list of runs where such changes were made are listed in Table 2.10.

Table 2.10: A list of the runs which were calibrated for the subsystems: tagger (`TAG`), start counter (`ST`), and time-of-flight (`TOF`). The calibrations were committed into the database for the range starting with the run shown and ending with the run just prior to the next listed run. A brief reason for calibration is given in the last column.

run	systems affected	reason
56363	`TAG, ST, TOF`	start of run
56503	`ST`	`ST` adjustment
56508	"	" "

continued on next page.

continued from previous page.

run	systems affected	reason
56661	TAG, ST, TOF	trigger and ST changes
56663	"	" "
56665	"	" "
56666	"	" "
56670	TAG	vacuum problem in tagger fixed
56673	TAG, ST, TOF	trigger change
56732	"	RF related problems fixed by Accelerator group
56765	TAG	T20 left HV problem
56766	"	T20 left HV adjusted
56782	TAG, ST, TOF	changes in calibration database
56855	"	" "
56923	"	start of intensity studies
57094	"	changes in calibration database
57154	ST	adjusted ST ADC timing in gate

2.3.2 Subsystem Calibrations

The raw TDC time ($t_{\mathtt{TDC}}$) from any particular element in the detector is related to the event start time (t_{start}) by the equation:

$$t_{\mathtt{TDC}} = t_{\mathrm{start}} + t_{\mathrm{flight}} + t_{\mathrm{prop}} + t_{\mathrm{walk}} + t_{\mathrm{elec}}, \tag{2.1}$$

where t_{flight} is the flight time of the particle from the reaction vertex to the element such as a scintillator paddle or layer in the drift chamber, t_{prop} is the propagation time of the signal from the track to the detection electronics (PMTs or readouts at the ends of the wires in the DC), t_{walk} (called the *time walk*) is the time it takes the discriminator to recognize the signal as a "hit," and t_{elec} is the final electronics delay due to cable lengths and signal relays and is generally a constant for all particles at all momenta. The term of interest, t_{start}, is by definition the same for all hits in an event, however, it contains an arbitrary offset because it is a function of the trigger and therefore varies from event to event. The three times: t_{flight}, t_{prop} and t_{walk} are all functions of the momenta and masses of the particles passing through the detector elements. The approximate magnitudes of each term in Eq. 2.1 is shown in Table 2.11.

Table 2.11: Relative timing relationships for the terms of Eq.2.1. The time ranges are the approximate correction amplitudes applied to the data. The column "fn. of PID" indicates if the time is dependent on the particle mass or momentum.

term	approx. range	fn. of PID?	description
$t_{\mathtt{TDC}}$	0–400 ns	no	recorded time by the electronics
t_{start}	0–400 ns	no	event start time
t_{flight}	20–50 ns	yes	particle flight time from vertex
t_{prop}	0.1–10 ns	yes	signal propagation time *to* electronics
t_{walk}	100–400 ps	yes	discriminator response time
t_{elec}	0.1–10 ns	no	signal propagation time *in* electronics

The goal of the timing calibrations was to determine all the values in Eq. 2.1 for each detector element as a function of particle momentum, charge and/or mass when necessary. The actual value of interest is always the flight time of the particles from the reaction vertex to the detector element (t_{flight}) but the trigger offset inherent in t_{start} requires the use of the sum: $t_{\text{flight}} + t_{\text{start}}$. Only differences in these times (i.e. between two hits in the detector) were used in this analysis so that the trigger offset could be subtracted.

The two times in Eq. 2.1 that are the most difficult to determine were t_{prop} and t_{walk}. The first of these, the propagation time of the signal from the track to the electronics interface, is a property of the medium such as the gas or scintillator material. For double-ended paddles like in the TOF, this term was eliminated by taking the average of the TDC times from the two sides. The start counter which has PMTs on only one side of the scintillator paddles uses the intersection of the track from the DC information to determine this correction. The *time walk* term (t_{walk}) is a small ($< 5\%$) correction which represents the electronic's interface response time to a physical signal and is a function of the ADC pulse height as discussed below.

Energy calibrations are generally determined using a known event sample within the data. The tagger energy, for example, was calibrated using the exclusive reaction:

$$\gamma p \to p\pi^+\pi^-, \tag{2.2}$$

where the exclusivity was determined via missing momentum and missing mass cuts using the energy of the tagger hit associated with the event. The photon energy was then adjusted by taking the total energy of the $p\pi^+\pi^-$ system using

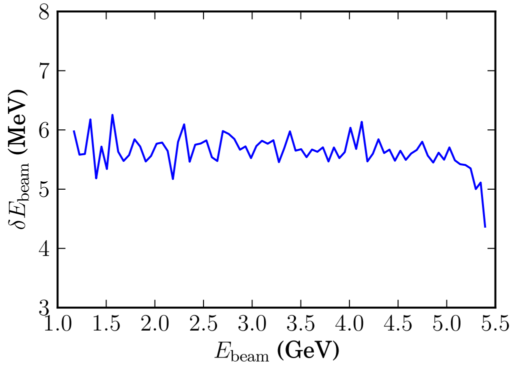

Figure 2.2: Resolution of the *logical* energy paddles in the tagger. The values were obtained by taking the difference in reported energy between two adjacent paddles. The unevenness can be attributed to overlapping regions of energy counters varying in size and the sagging of the E-counter plane[37]. An average resolution of 5.6 MeV is indicated by this plot.

the equation:

$$E'_{\text{beam}} = E_{\text{p}} + E_{\pi^+} + E_{\pi^-} - m_{\text{p}}, \tag{2.3}$$

where E_{p}, E_{π^+} and E_{π^-} are the energies of the outgoing particles, and m_{p} is the proton (target) mass. The average of at least 10k events per *logical* tagger energy paddle (see Sec. 1.4) was used for this correction and the results as a function of the beam energy is shown in Fig. 2.2. The inherent resolution of the tagger paddles for *g12* was approximately 5.6 MeV.

Results from the tagger energy calibration were used to calculate corrections to the momenta of the tracks, the energy corrections were subsequently recalculated. This iterative process was employed several times until the values obtained for both corrections converged. The energy difference between E'_{beam} in Eq. 2.3 and the energy reported by the tagger is shown in Fig. 2.3.

The resolution of the tagger time is approximately 130 ps as shown in Fig. 2.4 and this value is used to identify the `RF` beam-bucket associated with the event. The `RF` provides the best timing resolution, on the order of a few picoseconds, in `CLAS` and it is used to calibrate the other systems as described in the sections below.

The timing of the start counter (`ST`) was of critical importance for this analysis because it helped determine the tagger hit associated with the physical event. Here again, exclusive $\text{p}\pi^+\pi^-$ events were used and the tagger hit was matched to the average vertex time measured from these final state particles. The time walk (t_{walk}) of the signal from the track to the `PMT` is determined by the equation:

$$t_{\text{walk}} = t_0 + \frac{t_1}{a - a_0}, \tag{2.4}$$

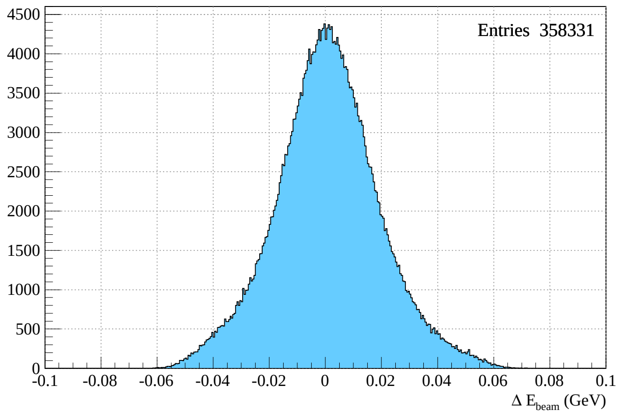

Figure 2.3: The energy difference in GeV, between $E_{\text{beam,corrected}}$ in Eq. 2.3, using the exclusive reaction (2.2) and the energy reported by the tagger. A Gaussian fit from -0.02 to 0.02 GeV gives a width of 16 MeV.

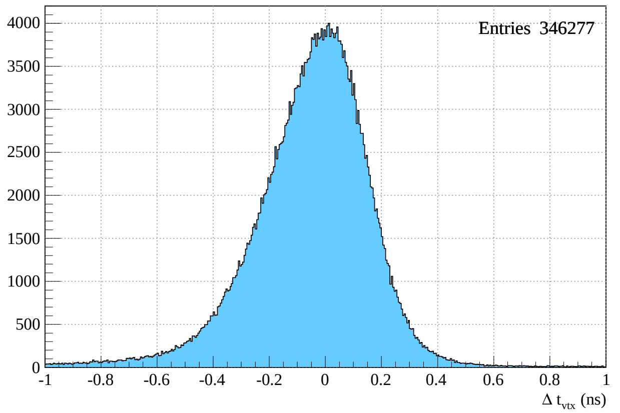

Figure 2.4: The difference in time between the tagger hit and the nearest `RF` clock tick using the exclusive reaction (2.2). A Gaussian fit from -0.2 to 0.2 ns gives a width of 130 ps.

where t_0 and t_1 were determined for each paddle from the data. Here, a is the `ADC` signal and a_0 is the `ADC` pedestal value. The difference in `ST` vertex time for the tracks and the tagger hit is shown in Fig. 2.5 and the final resolution of the `ST` was approximately 370 ps.

The method for determining the `TOF` resolution is identical to that of the start counter. However, the time walk correction is more sophisticated owing

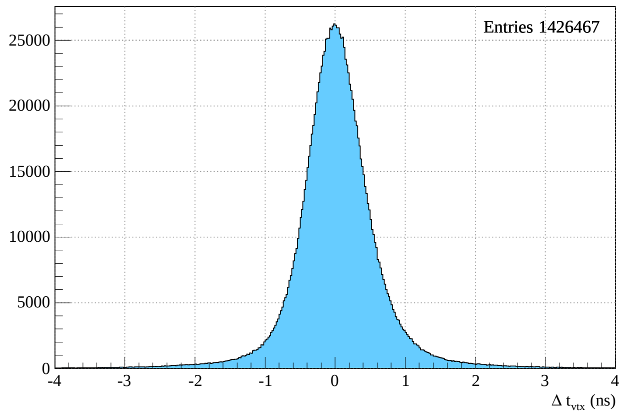

Figure 2.5: The difference in ST vertex time according to each of the tracks in the exclusive reaction (2.2) and the tagger hit. A Gaussian fit from -0.5 to 0.5 ns gives a width of 370 ps.

to the finer resolution of the TOF:

$$t_{\text{walk}} = \begin{cases} bx^{-c} & : a < a_1 \\ \frac{b}{a_1^c}\left(b + c\left[1 - \frac{(a-a_0)}{a_1 V_T}\right]\right) & : a \geq a_1 \end{cases}, \tag{2.5}$$

where t_0, b and c are constants determined for each TOF paddle and for each calibration run range (see Table 2.10), a is the TOF ADC signal, a_0 is the ADC pedestal value and V_T is the discriminator threshold value. This equation is essentially a power law below some ADC value a_1 and a linear function above, and it has the property of being smooth at this transition point. The difference in vertex times (TOF and TAG) for the (exclusive) $p\pi^+\pi^-$ tracks is shown in Fig. 2.6. The TOF had a timing resolution of approximately 230 ps after all calibrations were completed.

The drift-chamber was calibrated to first-order by aligning the data using the zero-field run where the particles traced a straight line. Once corrected for alignment, fixed delays and track dependent flight times were calculated to obtain the drift time of the signal from the track to each wire, given by[38]:

$$t_{\text{drift}} = t_{\text{prop}} - t_{\text{wire}} \tag{2.6}$$

where t_{prop} is the signal propagation time from Eq. 2.1 and t_{wire} is the time the signal took to propagate along the wire from the point of interaction to the electronics. The drift times (t_{drift} in Eq. 2.6) to each wire from the passing particle was then converted to a drift distance and the final tracks were determined by minimizing the absolute value of the residuals, shown in Fig. 2.7.

The mean of the residuals is shown in Fig. 2.9. The spread from -50 to

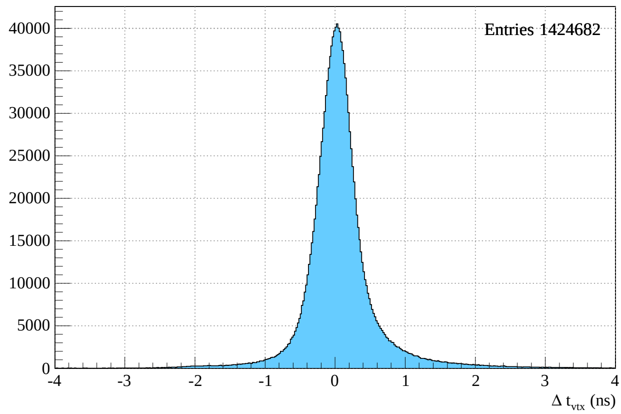

Figure 2.6: The difference in `TOF` vertex time according to each of the tracks in the exclusive reaction (2.2) and the tagger hit. A Gaussian fit from -0.5 to 0.5 ns gives a width of 230 ps.

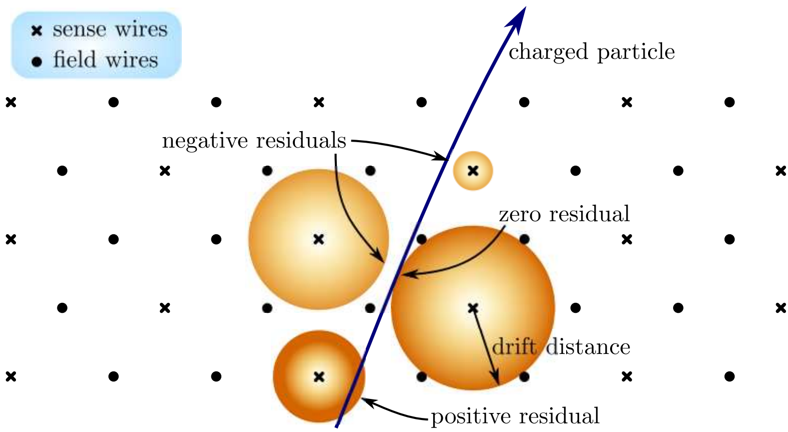

Figure 2.7: Schematic of a track going through five layers of the drift chamber looking down the sense and field wires of the `DC`. Shown are the residuals obtained from the calculated drift distance, t_{drift} in Eq. 2.6.

50 µm in the mean contributes to the overall resolution in the drift chambers. The standard deviation of the residuals in the `DC`, shown in Fig. 2.10, was no greater than 380 µm for superlayer 6 — the farthest from the target. These values combine to give a resolution of approximately 430 µm.

The maximum error of the momentum from the `DC` can be estimated by considering the constant magnetic field approximation where the particle traces

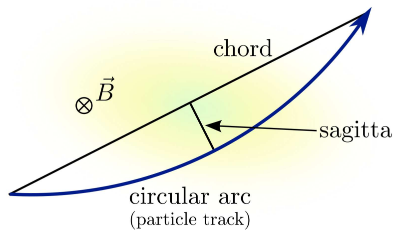

Figure 2.8: The sagitta of a circular arc is the maximum distance between the arc and a given chord. Since charged particles traveling perpendicular to a uniform magnetic field trace a circular path, this is used as an approximation for determining the maximum error of the measured momentum. Shown here is a positively charged particle moving through a uniform magnetic field ($\vec{B}$) going into the page.

a circular arc in region 2. The momentum (p) can be calculated from the sagitta (s), which is described in Fig.2.8, of the track in this region by

$$p = \frac{\ell^2 qB}{8s}, \tag{2.7}$$

where ℓ is the length of the cord defined by the arc, q is the charge, and B is the magnetic field. The cord length was approximately 1.5 m, the charge was $\pm e$ and the magnetic field was ~ 1 T. If we take the resolution of the sagitta (δs) to be the resolution of the residuals, then the error of the momentum (δp), which is momentum-dependent, becomes

$$\delta p = \frac{8p^2}{\ell^2 qB}\delta s. \tag{2.8}$$

This gives an approximate resolution of:

$$\delta p = 0.002 \text{ GeV}^{-1} \times p^2. \tag{2.9}$$

Therefore, a 2 GeV particle going through the drift chamber should have an approximate resolution of 8 MeV. It is useful to note that this is an estimate on the *maximum* error and that final momentum corrections, which are discussed in Sec. 3.1, were done based on particle identification to further improve the resolution in the data.

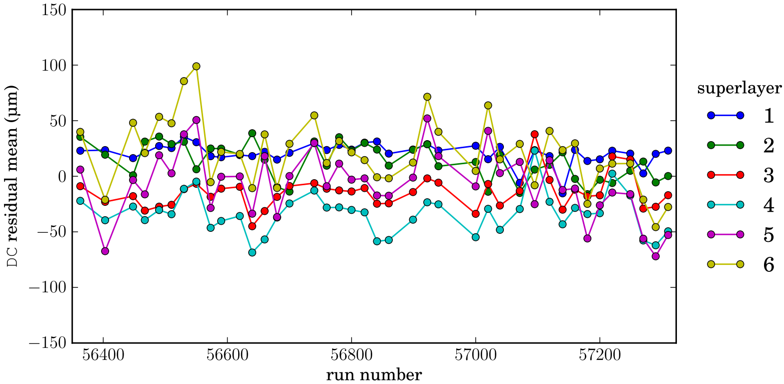

Figure 2.9: Mean of residuals in the drift-chamber for each of the six superlayers. A characteristic subset of the good runs listed in Table 2.1 were used.

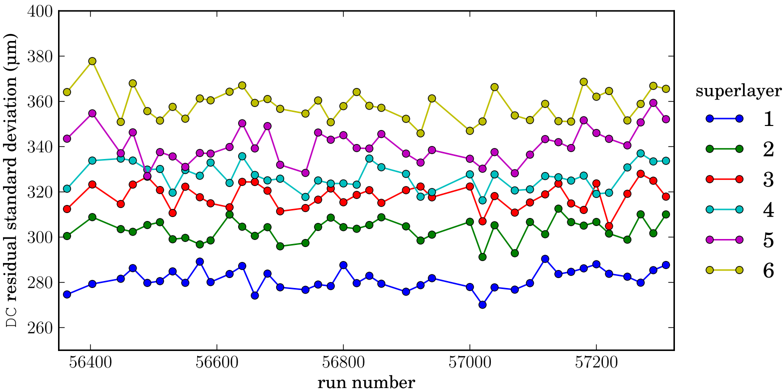

Figure 2.10: Standard deviation of residuals in the drift-chamber for each of the six superlayers. A characteristic subset of the good runs listed in Table 2.1 were used.

2.4 Raw Data Reconstruction

The process of reconstructing tracks and their subsequent particle identification from raw data, done by the program `a1c` and outlined in Fig. 2.11, began with the drift-chamber. The wires triggered by the charged particles propagating through the DC provided the basis for identifying tracks. The first step used all the activated wires in the DC while disregarding the timing of the hits. The "hit-based" reconstruction flowchart is shown in Fig. 2.12. The DC hits were filtered for noise in the form of isolated hits and the rest were grouped into clusters in each of the *superlayers*. The hits inside each cluster were then linked

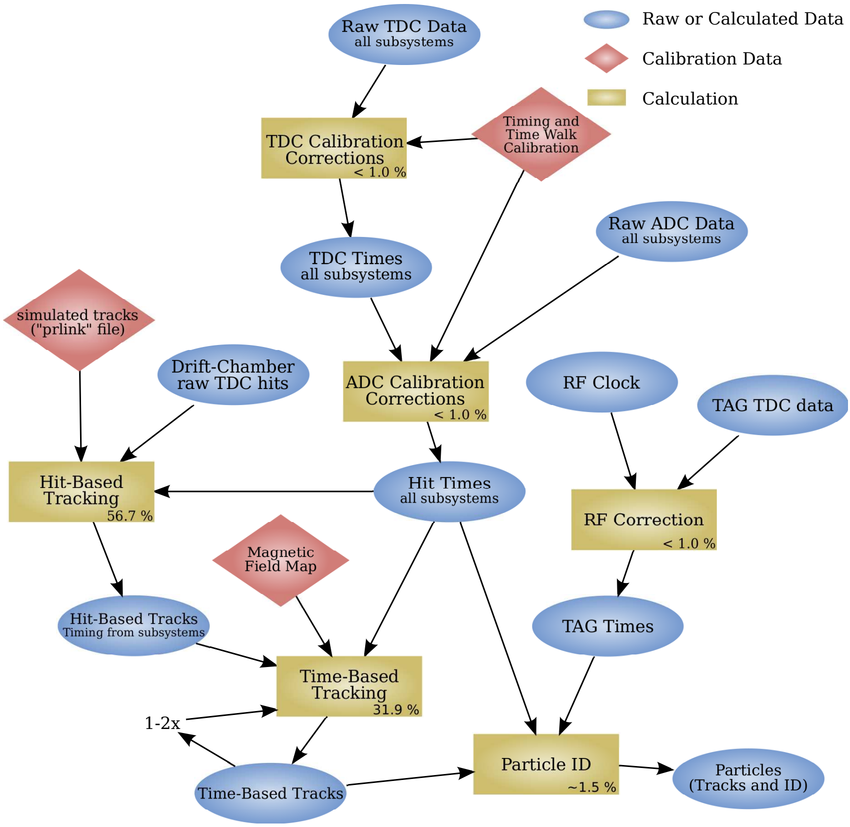

Figure 2.11: Flow chart of the reconstruction process from raw data to identified tracks with momentum. "Subsystems" refers to the start counter, Čerenkov counter, electromagnetic calorimeter and the time-of-flight detectors. Percentages shown indicate the relative time taken to do the calculations.

to form track segments which were then linked from *superlayer* to *superlayer* to create track candidates.

The midpoints and local angles for each of the three *superlayers* of the resulting tracks were recorded. These (six) numbers were used to look up a first-approximation of the initial vertex and momentum in a "roads-map" table — also called the "prlink" table. The roads-map was a random sampling of simulated tracks of varying momenta and vertex positions from inside the target and traveling through the magnetic field. The field used for *g12* was the "half-field," where the current in the coils was 1930 A.

At this point in the reconstruction, a track was defined as a vertex and 3-momentum with charge $\pm 1\ e$ where e is the absolute value of the charge of the

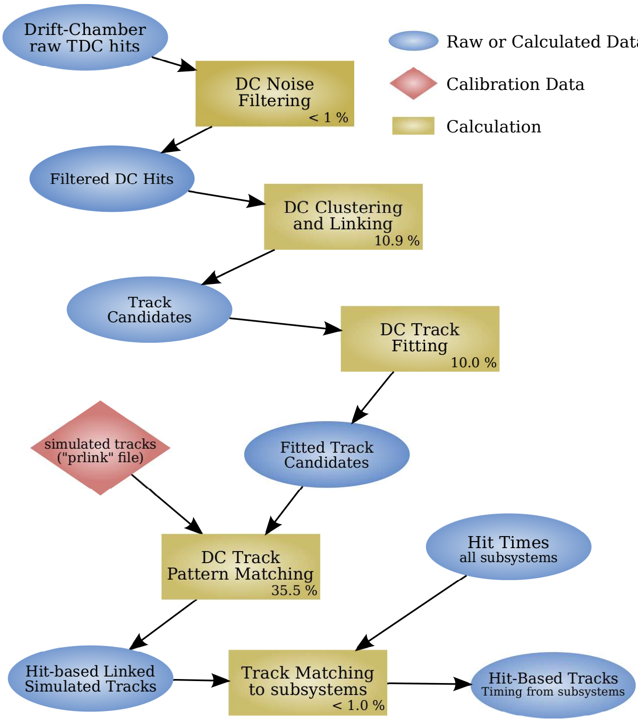

Figure 2.12: Flow chart of the hit-based tracking part of the reconstruction shown in Fig. 2.11. "Subsystems" refers to the start counter, Čerenkov counter, electromagnetic calorimeter and the time-of-flight detectors. Percentages shown indicate the relative time taken to do the calculations with respect to the full reconstruction.

electron. However, no timing had been used so the speed of the track could not be calculated and therefore the particle identification was still ambiguous. Furthermore, it was often the case that there were several track candidates matched from a large contiguous grouping of hits, however these were filtered out based on timing information in the next step of the reconstruction.

To get the needed timing information, each hit-based track was associated with a hit in a time-of-flight counter as shown in Fig. 2.13. The tracks were then fitted to the in-time wire hits in the `DC` in a process called "track-swimming." This process reduced the clusters in the `DC` that gave multiple hit-based tracks to one time-based track, and provided more accurate momentum and vertex information for the particle. After this first fit, the initial parameters of these tracks were used to re-swim the particle through the `DC` for the final momentum and vertex calculation. The track was then matched to the start counter, electromagnetic calorimeter and Čerenkov counter when these subsystems had a hit that was in-time.

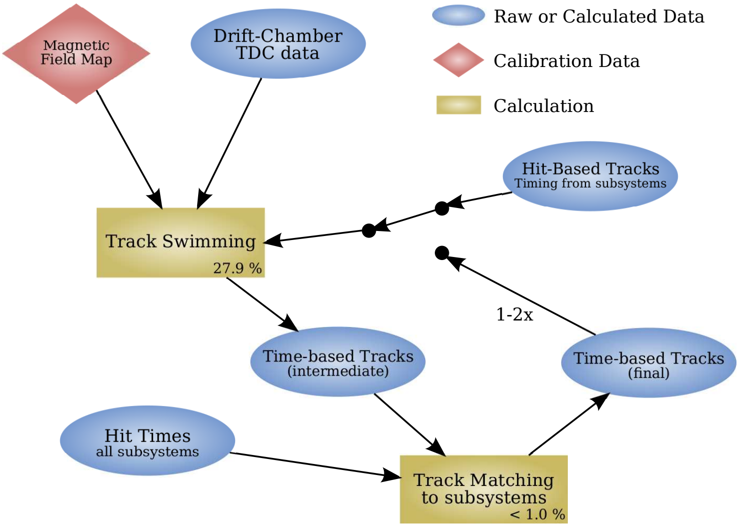

Figure 2.13: Flow chart of the time-based tracking part of the reconstruction shown in Fig. 2.11. "Subsystems" refers to the start counter, Čerenkov counter, electromagnetic calorimeter and the time-of-flight detectors. The switch indicates that hit-based tracks are input into the swimming calculation, after which the time-based tracks are used creating a feed-back loop. Percentages shown indicate the relative time taken to do the calculations with respect to the full reconstruction.

Using the difference of the times from the time-of-flight ($t_{\texttt{TOF}}$) and start counter ($t_{\texttt{ST}}$), along with the path length from the `ST` to the `TOF` ($\ell_{\texttt{ST}-\texttt{TOF}}$), the speed of each particle was determined:

$$\beta_{\texttt{ST}-\texttt{TOF}} = \frac{t_{\texttt{TOF}} - t_{\texttt{ST}}}{c\ell_{\texttt{ST}-\texttt{TOF}}}, \tag{2.10}$$

where c is the speed of light. In the case where a start counter time could not be associated with the track, β was obtained from the tagger hit of the event:

$$\beta_{\text{vtx}-\texttt{TOF}} = \frac{t_{\texttt{TOF}} - t_{\text{vtx}}(\texttt{TAG}_{\texttt{RF}})}{c\ell_{\texttt{TOF}}}, \tag{2.11}$$

where $t_{\text{vtx}}(\texttt{TAG}_{\texttt{RF}})$ is the `RF`-corrected tagger vertex time. The tagger hit is the one that is closest to the *average* time of the tracks in the event. With β and the momentum (p) in hand, we could then calculate the mass of the particle:

$$m = \frac{cp^2}{\beta^2} \tag{2.12}$$

The particle identification is done based on the mass from Eq. 2.12. For

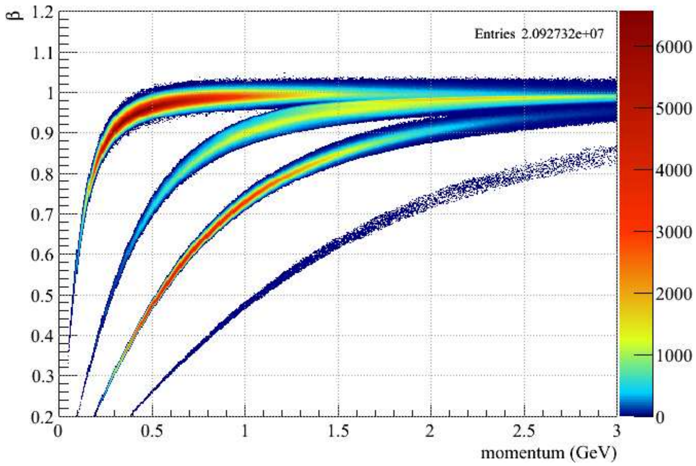

Figure 2.14: Speed (β) versus momentum of final state particles detected by CLAS after vertex-timing cuts which are detailed in Chapter 3. The bands shown follow the curve given by Eq. 2.12 and are identified from top to bottom as pions, kaons, protons and deuterons.

the *g12* experiment, all final state charged particles are one of the following: electron, pion, muon, kaon, proton, or deuteron. The initial identification only considers pions, kaons, protons and deuterons. Leptons (electrons and muons) are filtered out based on the signals from the EC and CC later in the analysis. The major difficulty comes from separating pions and kaons which merge at momenta above 1.5 GeV as shown in Fig. 2.14 making identification ambiguous. Methods used to deal with this ambiguity are discussed in Chapter 3.

After the particles were identified, the four momentum was determined by calculating the energy from the mass found in the literature (m_{book}) and the momentum ($\vec{p}$) from the drift-chamber:

$$E^2 = m_{\text{book}}^2 c^4 + |\vec{p}|^2 c^2. \tag{2.13}$$

The vertex was taken as the point along the track that came closest to the center of the beam line. The basic vertex timing cuts are detailed in Sec. 3.3, along with a discussion about the effects of the 2 ns beam structure.

This is not the end of the story for track measurement and identification. Since tracking began at region 1 of the DC, after the particle had already gone through the target and start counter, the effects were taken into account as part of the "energy-loss" correction during the analysis phase as discussed in Chapter 3. Small corrections to the momentum and beam energy were also done as part of the final analysis. These accounted for unknown factors which affected the particles.

2.4.1 Data Reconstruction on the JLab Computing Farm

Reconstruction of the entire *g12* data set was a major undertaking due to the size of the collected data. Furthermore, the relatively high efficiency of the trigger ($> 80\%$ is typical for photon runs at JLab) added to the reconstruction time as most of the events recorded may have been "good" events. The computing farm at JLab, as it stood at the end of the experiment in 2008, was estimated to take approximately 12 months to process all 126 Terabytes (TB) which consisted of 26 billion triggers.

Fortunately for us, there were several major upgrades to the computing farm that occurred during the time *g12* was doing the final reconstruction which started in late August of 2009 as shown in Fig. 2.15. We worked closely with the administrators of the computing farm to work out the appropriate queuing algorithm so that our jobs would get a certain priority. This resulted in an increase in throughput within the first week of running. In mid-September, the "cache" disk, which was used to hold the raw data as it was read from tape, was doubled in size which allowed us to run almost twice as many jobs at a time.

In early October, ten new compute nodes were installed which ran on new processors that promised a one to two-fold increase in processing speed. These were dual, quad-core, hyper-threaded, 64-bit nodes, each of which could handle up to 16 simultaneous jobs. We were the first Hall B run-group to utilize these computers and our throughput was a consistent 500 files per day for the last half of *pass 1* which ended just before the new year in 2009. The reconstructed data was twice the size of the raw data with only a minimal amount of redundancy kept for convenience, and we were reading 1 TB and writing 2 TB per day on average.

With all of these upgrades, The full data reconstruction of over 60,000 files took four months (see Fig. 2.15) and we paved the way for subsequent experiments to switch to 64-bit compatible reconstruction code.

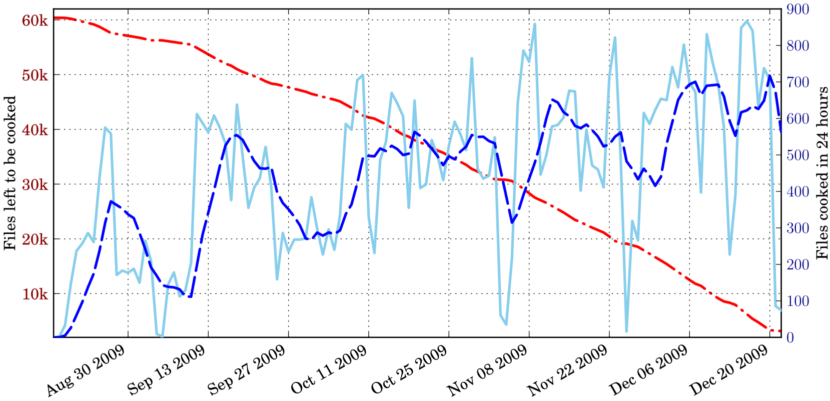

Figure 2.15: *g12* final reconstruction (*pass 1*) timeline. This figure shows the number of files, each approximately 2 GB with about 450k events, that were cooked every 24 hours starting late August, 2009 by the solid light-blue line. The weekly average is indicated by the dashed dark-blue line, while the total files left to be cooked, out of over 60k, is indicated by the dash-dot red line.

Chapter 3

Analysis

The analysis of CLAS data begins with reconstructed events (see Sec. 2.4), the essential parts of which are the identified particle and its momentum. The rudimentary particle identification schemes associated with the reconstruction program (A1C) are extremely loose for most kaon analyses. That is, more than half the tracks labeled as kaons are in fact misidentified pions and this is the primary source of background “noise” in kaon analyses done with CLAS. However, it is an excellent starting point for the analysis that follows, and virtually all event selections criteria are chosen so as to minimize this pion-contamination without destroying the targeted resonances.

The first step of this analysis identifies the beam photon that triggered the event. All the tracks are then matched to this photon and out-of-time tracks are thrown out. The particles are identified based on their momentum measured in the DC and speed obtained from the TOF. The energy of each is then recalculated using the mass of the particle as found in the literature. With the four-momenta of the tracks in hand, the data are explored for resonances, cross sections and other trends. These steps are described in detail in the next few sections as a setup for the final results presented in the following chapter which include the excitation function for the photoproduction of the $\Xi^-(1320)$ and $\Xi^-(1530)$ states as well as total cross section upper limits of higher-mass cascades and iso-exotic states.

3.1 Particle Identification

Particle identification of the measured tracks in CLAS uses the momentum ($\vec{p}$) from the DC. Vertex times for each track are measured by the TOF and the average is used to determine the photon hit in the tagger. The speed of each particle (β)* is then determined by the time difference from the vertex as measured by the photon tagger, to the time-of-flight counter. The β versus momentum for all charged tracks with a rough particle identification from early on in the

*In this work, all speeds are given as fractions of the speed of light: $\beta = v/c$.

reconstruction process is depicted in Fig. 3.1. The major bands correspond to pions, kaons and protons just as in Fig. 2.14 on page 64. The secondary bands come from tracks where the timing information is off by multiples of two nanoseconds due to the beam structure. At this point, there is no way to differentiate a kaon from a pion that came from a previous beam bucket where the secondary pion bands overlap the kaon band, eg. at a momentum of 1 GeV for example.

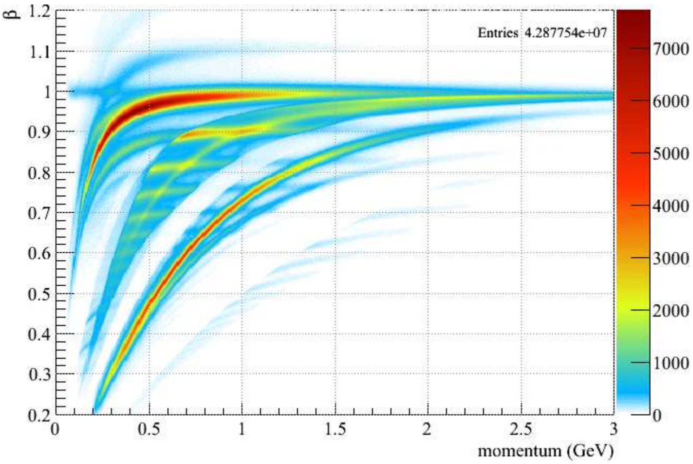

Figure 3.1: Speed (β) versus Momentum of final state particles detected by CLAS without vertex or timing cuts.

Once the momentum and speed is obtained, the mass of the particle is calculated:

$$m = \left(\frac{1}{\beta^2 p^2} - 1 \right)^{\frac{1}{2}}, \tag{3.1}$$

and it is identified as either a pion, kaon or proton. Since these particles have well defined masses, and because the momentum as measured by CLAS is known to better accuracy than β, the energy is recalculated using the mass (m_{book}) as found in the literature[8]:

$$E = \left(p^2 + m_{\text{book}}^2 \right)^{\frac{1}{2}}. \tag{3.2}$$

This energy, plus the momentum from the DC make up the four-momenta of the detected tracks for a given event. Requirements made on this data sample, based on timing, vertex positions or other aspects as discussed in the following sections, are all done in an effort to enhance the signal to background ratios for the resonant states. Most of these requirements are then used to determine the upper limits on states which are not seen in the data.

3.2 General Features of Kaon Data in *g12*

In this section, the various features of the kaon data from the *g12* experiment are explored. Known states such as the $\Lambda(1115)$, $\Sigma(1198)$ and $\varphi(1020)$ are measured and compared to the values found in the literature. This analysis is concerned primarily with doubly-strange baryon resonances. The jumping-off point is the missing mass off K^+K^+ (shown in Fig. 3.2) in the reaction:

$$\gamma p \to K^+K^+X^-. \tag{3.3}$$

In this figure, there are three major peaks on a fairly smooth background. The peak at 1.1 GeV is the $\Sigma^-(1198)$ and is discussed later in this section. The middle peak at 1.3 GeV is the well known $\Xi^-(1320)$ state in the reaction:

$$\gamma p \to \Xi^-(1320)K^+K^+. \tag{3.4}$$

As discussed in Sec. 3.3, this is the signal on which the timing and vertex cuts were based. The third signal, at 1.53 GeV, is the $\Xi^-(1530)$ state — the doubly-strange baryon in the decuplet of Gell-Mann's eight-fold way as shown in Fig. 2 on page 3.

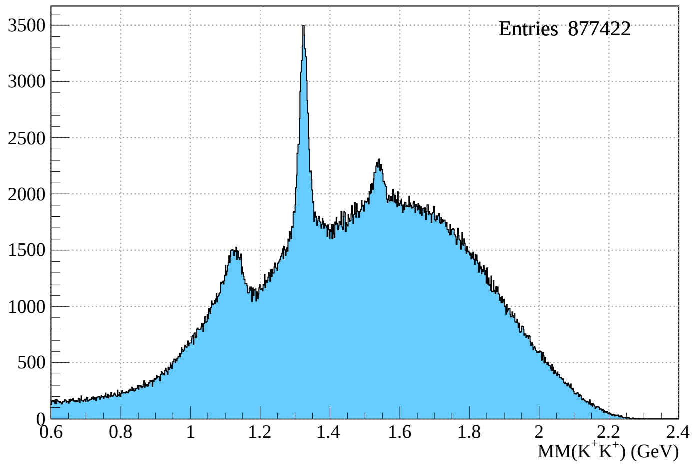

Figure 3.2: Missing mass off K^+K^+ in the reacton $\gamma p \to K^+K^+X^-$ with cuts on the vertex time for both K^+'s as described in Table 3.2 on page 81. The three peaks at 1.1, 1.32 and 1.53 GeV correspond to the $\Sigma^-(1198)$ where a π^+ was misidentified as a K^+, the $\Xi^-(1320)$ and the $\Xi^-(1530)$ respectively.

The momentum vs. K^+K^+ missing mass for each of the K^+'s is shown in Figs. 3.3 and 3.4. There are three horizontal bands corresponding to the three

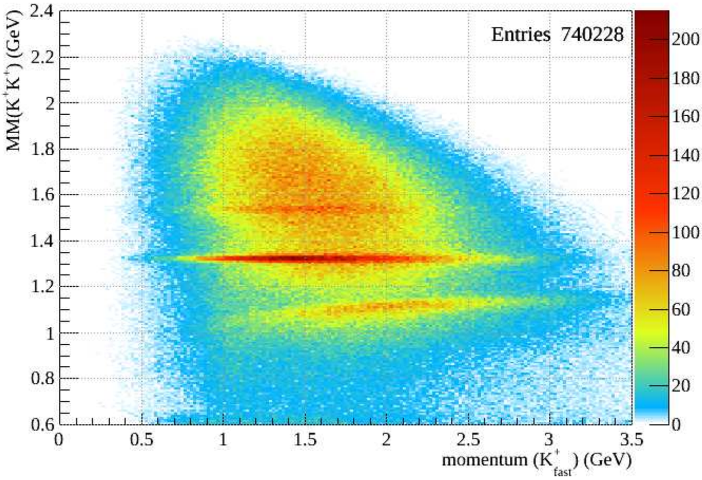

Figure 3.3: Missing mass off K^+K^+ vs. the K^+_{fast} momentum in the reaction $\gamma p \rightarrow K^+K^+X^-$ with cuts on the vertex time for both K^+'s as described in Table 3.2 on page 81. The three horizontal bands correspond, low to high, to the $\Sigma^-(1198)$, $\Xi^-(1320)$ and the $\Xi^-(1530)$.

peaks in Fig. 3.2. The vertical band in Fig. 3.4 at 0.2 GeV represents noise at the detection threshold. These events were cut from the data, indicated by the dashed line and the cut is listed in Table 3.3 on page 88.

A negative consequence of recalculating the energy of the detected particles based on particle identification is that the tracks with a *measured* mass lower than the book value are adjusted to become stationary in the laboratory frame; that is, they have zero momentum. This cannot be the case since the particle had to have enough energy to reach to the detector. In this analysis, these events are cut from the data to avoid false signals which would show up as peaks at *threshold* in the invariant mass distributions. The vertical band at 1 GeV in Fig. 3.5, and the spike at threshold in the projection of this data on the x-axis, the invariant mass of K^+K^+, Fig. 3.6 shows this effect. The dashed line indicates the cut made to remove these events from the K^+K^+ data and is listed in Table 3.3.

As mentioned before, in kaon analyses using the `CLAS` detector, pions are often misidentified as kaons. In the reaction $\gamma p \rightarrow K^+K^+X^-$, if one of the kaons is actually a pion from a previous beam bucket, it will show up as a baryon resonance in the reaction: $\gamma p \rightarrow K^+X$. The missing mass off each K^+ is plotted against each other in Fig. 3.7. The horizontal and vertical bands correspond to the singly-strange baryons resonances. For these events, the other particle identified as a kaon is actually a pion, though it is uncertain whether it was involved in the event, and the baryon is either a Λ or Σ^0.

The peaks in the missing mass off K^+_{fast} in the reaction $\gamma p \rightarrow K^+K^+X^-$

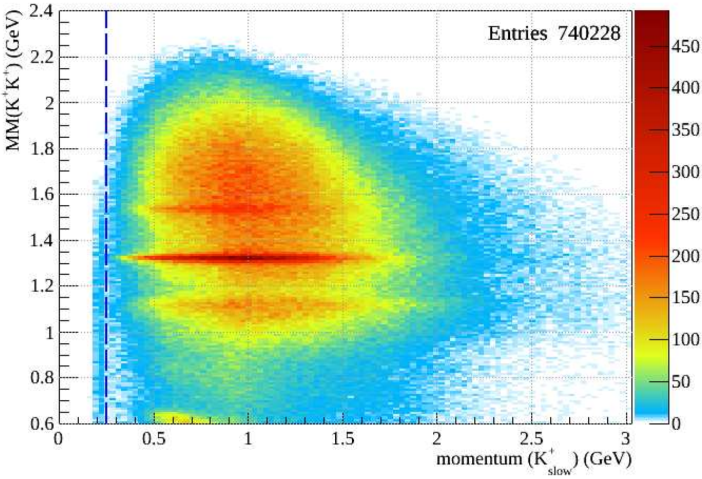

Figure 3.4: Missing mass off K^+K^+ vs. the K^+_{slow} momentum in the reacton $\gamma p \rightarrow K^+K^+X^-$. The three horizontal bands correspond, low to high, to the $\Sigma^-(1198)$, $\Xi^-(1320)$ and the $\Xi^-(1530)$. The vertical band at 0.2 GeV corresponds to "noise" events at detection threshold and were cut from the data indicated by the blue dashed line.

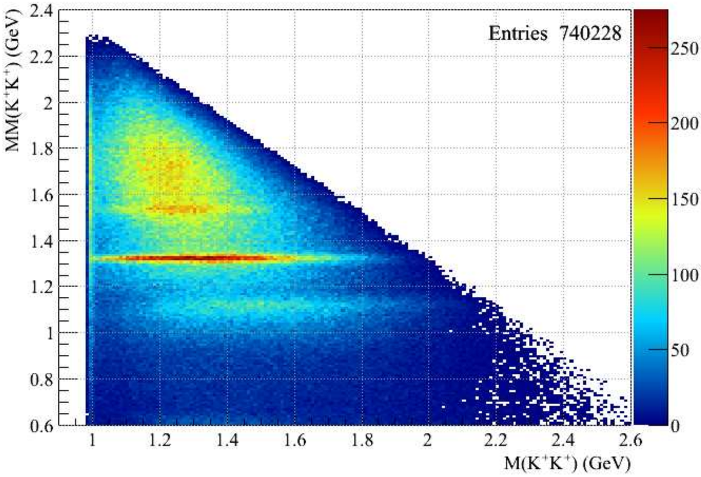

Figure 3.5: Missing mass off K^+K^+ vs. the invariant mass of K^+K^+ in the reaction $\gamma p \rightarrow K^+K^+X^-$. The three horizontal bands correspond, low to high, to the $\Sigma^-(1198)$, $\Xi^-(1320)$ and the $\Xi^-(1530)$. The vertical band at 1 GeV corresponds to events where the *measured* mass of the kaons were below that found in the literature and were artificially adjusted up to threshold.

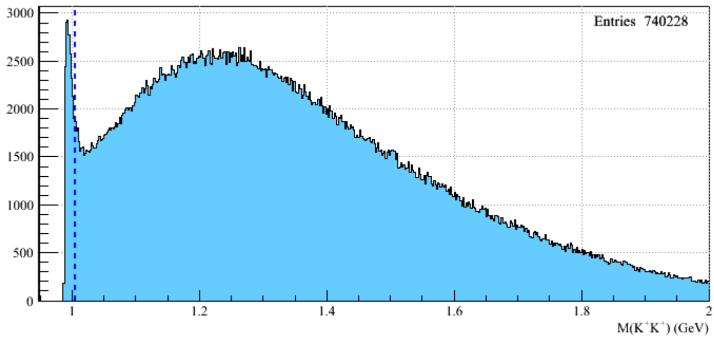

Figure 3.6: The invariant mass of K^+K^+ in the reaction $\gamma p \to K^+K^+X^-$. This is the projection of Fig. 3.5 onto the x-axis. The blue dashed line indicates the cut made on the data and is listed in Table 3.3 on page 88.

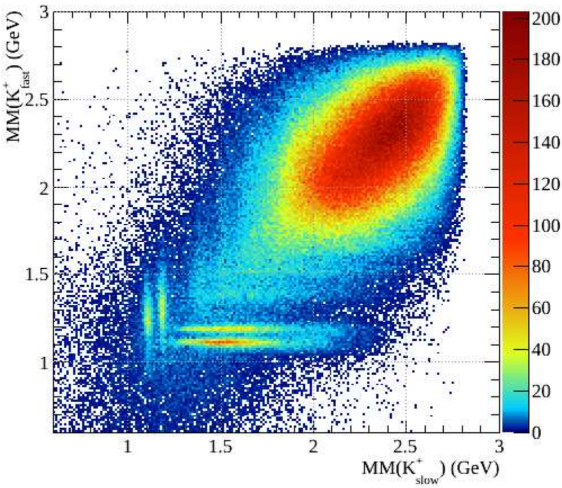

Figure 3.7: Missing mass off K^+_{fast} vs. the missing mass off K^+_{slow} in the reaction $\gamma p \to K^+K^+X^-$. The bands are identified in Fig. 3.8 which is the projection of this data on the y-axis where the missing mass off the K^+_{slow} is greater than 1.3 GeV.

shown in Fig. 3.8 correspond to the horizontal bands in Fig. 3.7. This data

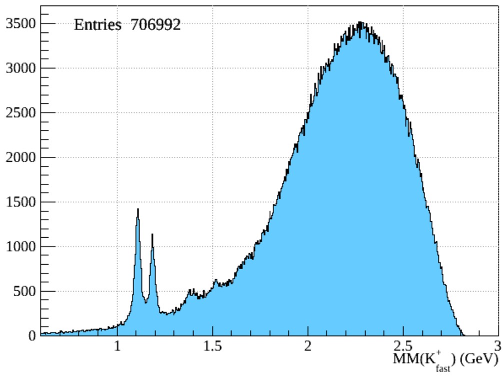

Figure 3.8: Missing mass off K^+_{fast} in the reaction $\gamma p \to K^+K^+X^-$. The peaks correspond, from left to right, to the $\Lambda(1115)$, $\Sigma^0(1198)$, $\Sigma^0(1385)$ which is together with the $\Lambda(1405)$, $\Lambda(1520)$ and a slight enhancement indicative of the $\Sigma^0(1660)$. The shape of the data above 1.7 GeV is dominated by phase-space.

consist of events that are one of

$$\gamma p \rightarrow K^+K^+X^- \tag{3.5}$$
$$\gamma p \rightarrow K^+\pi^+X^- \tag{3.6}$$
$$\gamma p \rightarrow K^+X^0 \tag{3.7}$$

where both kaons were actually kaons. The π^+ was misidentified as a K^+ and was part of the event, or the the π^+ was misidentified as a K^+ and was not part of the event. The peaks in Fig. 3.8 correspond, from left to right, to the $\Lambda(1115)$, $\Sigma^0(1198)$, $\Sigma^0(1385)$ which is together with the $\Lambda(1405)$, $\Lambda(1520)$ and a slight enhancement indicative of the $\Sigma^0(1660)$. The measured masses and widths of several of these states are listed in Table 3.1.

To produce the cascades, the missing mass off each K^+ must be greater than 1.8 GeV ($\Xi^-(1320)$ mass plus 494 MeV for the other K^+) and so these singly-strange baryon resonances do not interfere with the Ξ states. Furthermore, the smoothness of the missing mass off each K^+ above 1.7 GeV indicates phase-space dominance since there are no apparent resonant structures. This suggests that the higher singly-strange resonances are broad enough to "blend in" with the background in the missing mass off K^+K^+. While effort in removing or accounting for this background is done in this analysis, the anticipation that the Ξ^* states are narrow (30–50 MeV widths as discussed in Sec. 0.1 on page 5) means that the cascades should show up as narrow bumps on a smooth background.

The neutral cascade ground state, $\Xi^0(1315)$, can be seen in the missing mass off $K^+K^+\pi^-$ in the reaction $\gamma p \to K^+K^+\pi^-X^0$. It shows up as the vertical band

Table 3.1: Masses and widths of known states seen in the K^+K^+ data of the *g12* experiment. Width measurements are found from a Breit-Wigner convoluted with a Gaussian peak where the Gaussian has fixed width obtained from the $\Lambda(1115)$ resolution. These fits were obtained using the data shown in several figures shown later in this section and the next as indicated.

resonance	mass (MeV)	width (MeV)
from $MM(K^+_{fast})$, Fig. 3.8		
$\Lambda(1115)$	1109.4 ± 0.25	–
$\Sigma^0(1193)$	1186.6 ± 0.4	–
$\Sigma^0(1383)$	1385 ± 7	31 ± 3
$\Lambda(1520)$	1518 ± 3	16 ± 3
from $M(K^+K^-)$, Fig. 3.13		
$\varphi(1020)$	1019.5 ± 0.2	–
from $MM(K^+K^+\pi^-)$, Fig. 3.38		
$\Lambda(1115)$	1113.2 ± 0.5	–
$\Xi^0(1315)$	1313.8 ± 0.4	–
from $MM(K^+\pi^+\pi^-\pi^-)$, Fig. 4.28		
proton	936.5 ± 0.2	–
$\Sigma^+(1189)$	1186.8 ± 1.8	–

at 1.3 GeV in Fig. 3.9(a). The events at 1.53 GeV of the y-axis (missing mass off K^+K^+) correspond to the decay: $\Xi^-(1530) \to \Xi^0(1315)\pi^-$. In this figure at (b), the $\Lambda\pi^-$ decay of the ground state Ξ^- is seen, and misidentified pion data from the Σ events are at (c). There were events where both kaons were in-fact pions at (d), in the reaction $\gamma p \to \pi^+\pi^+\pi^- p$. These events do not contribute to the background in the missing mass off K^+K^+ above 0.7 GeV and were therefore ignored.

Fig. 3.10 shows the invariant mass of $p\pi^-$ vs. the missing mass off $K^+K^+\pi^-$ in the reaction $\gamma p \to K^+K^+p\pi^-X^-$. The $\Xi^0(1315)$ state can be seen again as the vertical band at 1.3 GeV, while the horizontal band at 1.1 GeV corresponds to the $\Lambda(1115)$. The two enhancements at

$$M(p\pi^-) = MM(K^+K^+\pi^-) = 1.1 \text{ GeV} \tag{3.8}$$

correspond to the exclusive reaction:

$$\begin{aligned}\gamma p \to \Xi^- & K^+K^+ \\ \hookrightarrow & \Lambda\pi^- \\ & \hookrightarrow p\pi^-,\end{aligned} \tag{3.9}$$

where only one of the pions was detected.

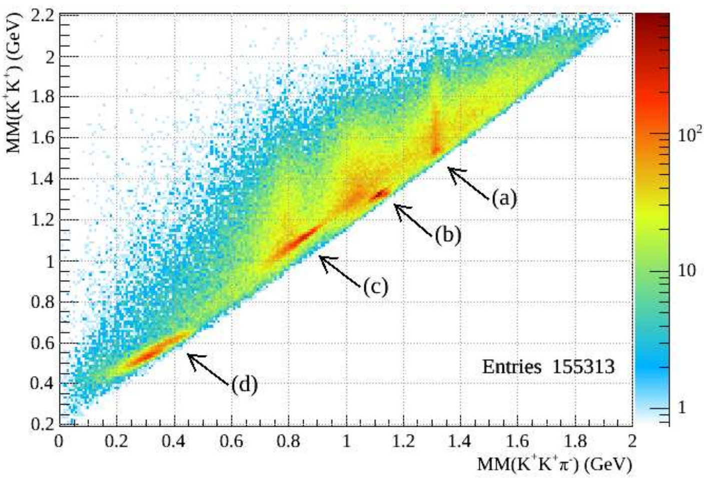

Figure 3.9: Missing mass off K^+K^+ vs. the missing mass off $K^+K^+\pi^-$ for the reaction $\gamma p \rightarrow K^+K^+\pi^- X^0$. The vertical band at (a) is the ground state $\Xi^0(1315)$, the peak at 1.53 GeV on the y-axis of which indicates the Ξ^0-decay of the $\Xi^{*-}(1530)$. The events at (b) correspond to the $\Lambda\pi^-$ decay of the ground state Ξ. The diagonal band at (c) are the events where a π^+ was misidentified as a kaon and corresponds to the enhancement at Fig. 3.11(a). The events in the band at (d) are where both kaons were actually pions.

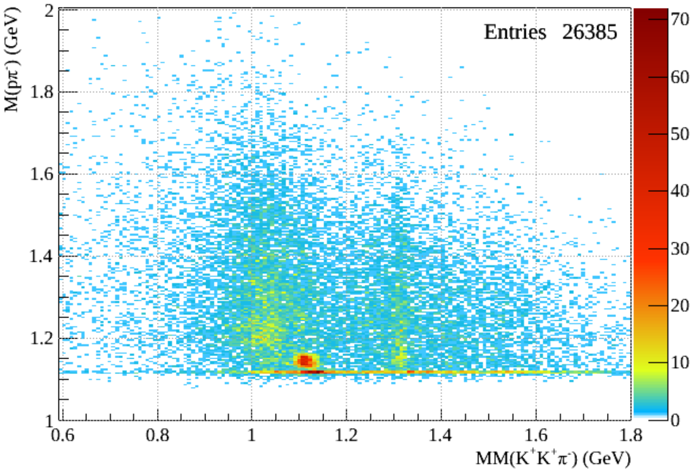

Figure 3.10: Invariant mass of $p\pi^-$ vs. the missing mass off $K^+K^+\pi^-$ in the reaction $\gamma p \to K^+K^+p\pi^-X^-$. The narrow horizontal band at 1.1 GeV corresponds to the $\Lambda(1115)$ and the vertical band at 1.3 GeV is the $\Xi^0(1315)$. The enhancements at (1.1, 1.1) GeV correspond to the exclusive reaction (3.9) where only one of the pions was detected.

The peak at 1.1 GeV in Fig. 3.2 and most MM(K^+K^+) plots can be explained by recalculating the missing mass off $K^+\pi^+$ where the π^+ was originally identified as a kaon. This is shown vs. the missing mass off K^+K^+ in Fig. 3.11. Here, the higher momentum, which is the one more likely to be misidentified as a kaon, is recalculated as the π. The *vertical* band right at 1.19 GeV (a) indicates that this peak corresponds to the reaction:

$$\gamma p \rightarrow \Sigma^-(1198)K^+\pi^+ \tag{3.10}$$

where the π^+ was identified as a K^+. These events to not overlap with the Ξ^- states, shown as the horizontal bands at 1.32 GeV (b) and 1.53 GeV (c) in the same plot, and thus do not contribute directly to the background of the Ξ signals. This is indicative of the primary difficulty with kaon analyses with `CLAS`: the misidentification of pions as kaons. Therefore, the pion contamination due to misidentification could be monitored, at least qualitatively, by the size of this peak.

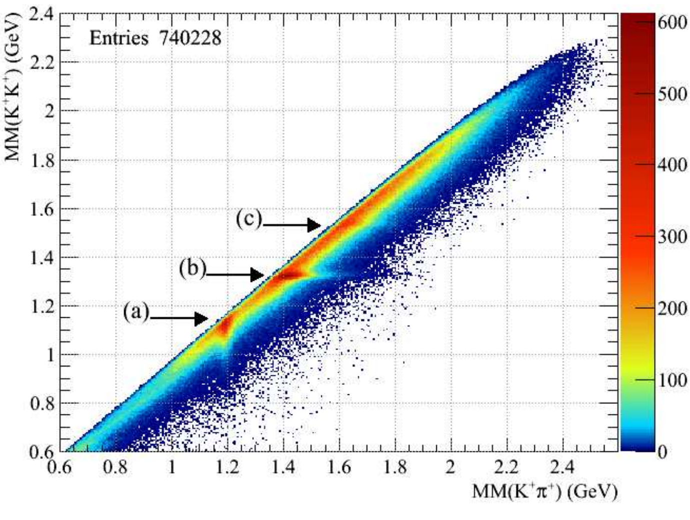

Figure 3.11: Missing mass off K^+K^+ where the K^+_{fast} was recalculated as π^+. The vertical band at (a) verifies that these are $\Sigma^-(1189)$ events where the π^+ was identified as a kaon. The horizontal bands at (b) and (c) correspond to the $\Xi^-(1320)$ and $\Xi^-(1530)$ respectively.

Fig. 3.12 shows the same data as in Fig. 3.11 however with the higher momentum K^+ recalculated as a proton instead of a π^+. The purpose was to investigate the possibility of a misidentified proton in the events. Again, the horizontal bands at 1.32 and 1.53 GeV are the cascade signals, but there is a lot more going on below a MM(K^+K^+) of 1.2 GeV. The curved horizontal band around 1.1 GeV is the reflection of the $\Sigma^-(1198)$ state seen in Fig. 3.11. The horizontal band at about 0.55 GeV is another reflection of the events where a π^+ was misidentified as a K^+. Finally, the events with missing mass off K^+p at the pion mass of 1.45 GeV indicates that these are:

$$\gamma p \to pK^+\pi^-, \tag{3.11}$$

where the proton and π^- possibly come from a $\Lambda(1115)$ decay.

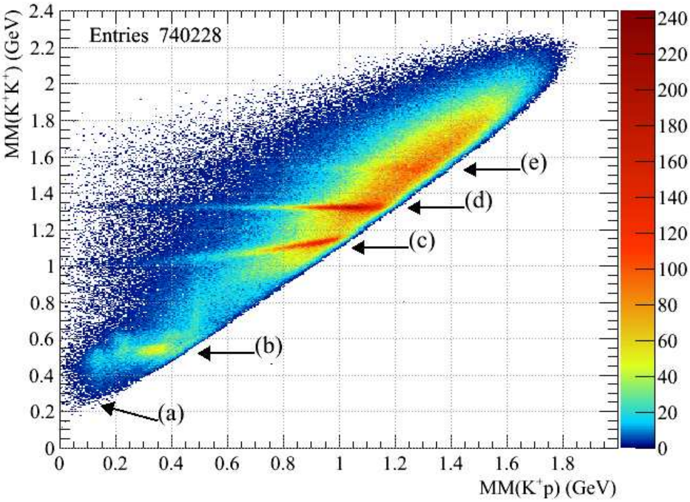

Figure 3.12: Missing mass off K^+K^+ where the K^+_{fast} was recalculated as a proton. The lack of events at (a) ($MM(pK^+) \approx$ pion mass) indicate that protons are not being identified as kaons. The events at (b) correspond to the enhancements seen in Fig. 3.9(d). The bands at (c), (d) and (e) correspond to the events in Fig. 3.11 at (a), (b) and (c) respectively.

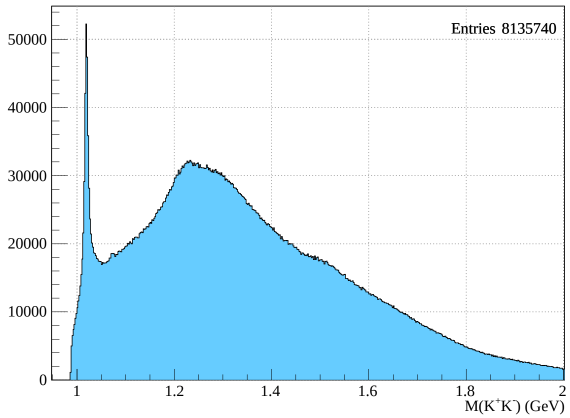

Figure 3.13: Invariant mass of K^+K^- in the reaction $\gamma p \to K^+K^-X^+$ with basic timing cuts on both kaons. The narrow peak at 1 GeV corresponds to the $\varphi(1020)$ which has decayed to K^+K^-.

3.3 Vertexing and Timing

Since the position of the tracks in CLAS are known to a relatively high accuracy (see the drift-chamber calibration Sec. 2.3.2 on page 53), the path lengths traveled from the vertex can be measured. This is defined as the distance between the point of closest approach (DOCA) to the beam line and the interaction point at the various subsystems such as the start counter or time-of-flight. The vertex time is calculated from the interaction time at one of the subsystems and subtracting the travel time along the path from the vertex. This requires a measurement of the speed of the particle (β).

The speed can be calculated between each subsystem, but only the start and time-of-flight counters provide sufficient timing accuracy to be used this way. For each track:

$$\beta_{\mathtt{ST-TOF}} = \frac{\ell_{\mathtt{TOF}} - \ell_{\mathtt{ST}}}{c\,(t_{\mathtt{TOF}} - t_{\mathtt{ST}})}, \tag{3.12}$$

$$\beta_{\text{vtx}-\mathtt{TOF}} = \frac{\ell_{\mathtt{TOF}}}{c\,(t_{\mathtt{TOF}} - t_{\text{vtx}}(\mathtt{TAG}_{\mathtt{RF}}))}, \tag{3.13}$$

where $\ell_{\mathtt{ST}}$ and $\ell_{\mathtt{TOF}}$ are the path lengths of the track from the vertex to the start counter and time-of-flight counter respectively, $t_{\mathtt{ST}}$ and $t_{\mathtt{TOF}}$ are the times of the hits in the counters and $t_{\text{vtx}}(\mathtt{TAG}_{\mathtt{RF}})$ is the RF-corrected vertex interaction time according to the chosen tagger hit. These times are relative to a trigger time for the event and therefore to each other. However, the trigger time has an inherent *jitter* with a sigma on the order of 20 ns and the times from event to event are *not* adjusted to account for this. The particle's mass, once determined by identification, can be calculated from the momentum:

$$\beta_p^2 = \frac{p^2}{m^2 + p^2}. \tag{3.14}$$

Given these different measurements of β, the vertex times of the tracks (t_{vtx}) can be calculated several ways:

$$t_{\text{vtx}}(\texttt{TOF}, \beta_p) = t_{\texttt{TOF}} - \frac{\ell_{\texttt{TOF}}}{c\beta_p}, \tag{3.15}$$

$$t_{\text{vtx}}(\texttt{TOF}, \beta_{\texttt{ST-TOF}}) = t_{\texttt{TOF}} - \frac{\ell_{\texttt{TOF}}}{c\beta_{\texttt{ST-TOF}}}, \tag{3.16}$$

$$t_{\text{vtx}}(\texttt{ST}, \beta_p) = t_{\texttt{ST}} - \frac{\ell_{\texttt{TOF}}}{c\beta_p}, \tag{3.17}$$

$$t_{\text{vtx}}(\texttt{ST}, \beta_{\text{vtx}-\texttt{TOF}}) = t_{\texttt{ST}} - \frac{\ell_{\texttt{ST}}}{c\beta_{\text{vtx}-\texttt{TOF}}}, \tag{3.18}$$

$$t_{\text{vtx}}(\texttt{ST}, \beta_{\texttt{ST-TOF}}) = t_{\texttt{ST}} - \frac{\ell_{\texttt{TOF}}}{c\beta_{\texttt{ST-TOF}}}. \tag{3.19}$$

These are highly correlated and selections based on three of these are enough. One could also calculate the vertex time from other subsystems such as the `EC` in this way, but again, the `ST` and `TOF` scintillating paddles provide the best timing resolution in the detector.

From the tagger hit, one can calculate the vertex time for each track. In all cases, the `RF`-corrected tagger time was used (see the tagger calibration Sec. 2.3.2 on page 53).

$$t_{\text{vtx}}(\texttt{TAG}_{\texttt{RF}}) = t_{\texttt{TAG,RF}} + t_{\text{prop}}, \tag{3.20}$$

where $t_{\texttt{TAG,RF}}$ is the `RF`-corrected time that the photon crossed the center of the target and t_{prop} is the propagation time from the center of the target to the track's vertex z-coordinate. This is the vertex time used to test against the times calculated from the start and time-of-flight counters.

The vertex timing cuts, illustrated in Figs. 3.14–3.19, are determined by the yield of the ground state $\Xi^-(1320)$ which is shown as the overlayed 1-dimensional histogram. A Gaussian curve is fitted to the yield distribution giving a mean (μ) and standard deviation (σ). The cut to be made in each case is

$$|t_{\text{vtx}}| < 3\sigma + |\mu| \tag{3.21}$$

so that the efficiency of the cut is always greater than 95% for the ground state $\Xi^-(1320)$. A summary of all the cuts are given in Table 3.2.

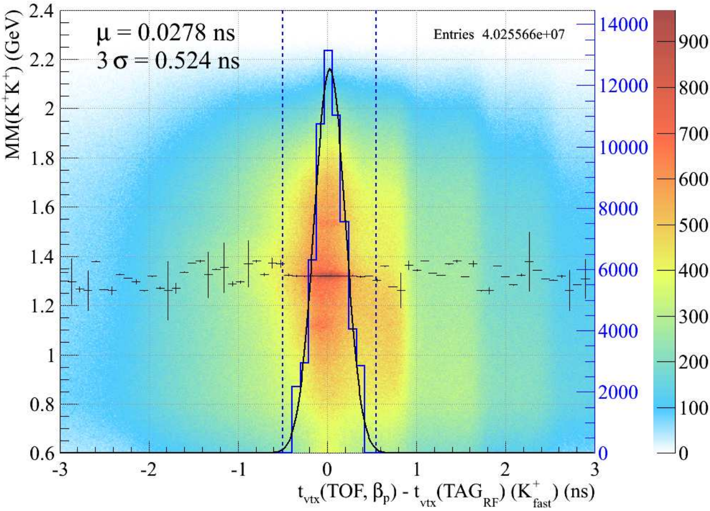

Figure 3.14: Missing mass off K^+ K^+ in reaction (3.23) on page 97 versus the difference in vertex time from the tagger and the time-of-flight counter for the faster K^+. The 2D histogram is sliced in x and each slice is projected onto the y-axis. A Breit-Wigner plus a 3^{rd}-order polynomial is fit around the mass of the ground state $\Xi^-(1320)$. The plotted positions in black are the mean of the signal peak with bars indicating the statistical error. The integral of the signal peak is overlayed as a 1D histogram with counts indicated on the right side y-axis. This is then fitted with a Gaussian, the mean and 3σ of which is printed in the upper left corner. The 3σ positions in x are illustrated by the dashed vertical lines.

Table 3.2: Cuts based on measured vertex times. Collectively, these cuts constitute the *vertex timing cut* for an individual track given a specific tagger hit. Times are in nanoseconds and the last column indicates the cuts used on K^-'s, pions and protons.

quantity	selections (ns)		
	fast K^+	slow K^+	other
$\lvert t_{vtx}(\texttt{TOF}, \beta_p) - t_{vtx}(\texttt{TAG}_{\texttt{RF}})\rvert$	< 0.55	< 0.69	< 0.7
$\lvert t_{vtx}(\texttt{ST}, \beta_{vtx-\texttt{TOF}}) - t_{vtx}(\texttt{TAG}_{\texttt{RF}})\rvert$	< 1.29	< 1.24	< 1.25
$\lvert t_{vtx}(\texttt{TOF}, \beta_{\texttt{ST}-\texttt{TOF}}) - t_{vtx}(\texttt{TAG}_{\texttt{RF}})\rvert$	< 1.35	< 1.29	< 1.33

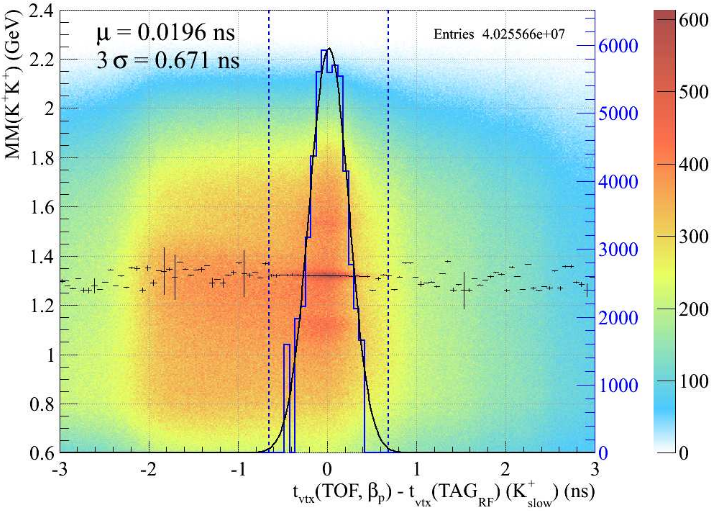

Figure 3.15: Missing mass off K^+ K^+ versus the difference in vertex time from the tagger and the time-of-flight counter for the slower K^+. See Fig. 3.14 for a detailed explanation of this plot.

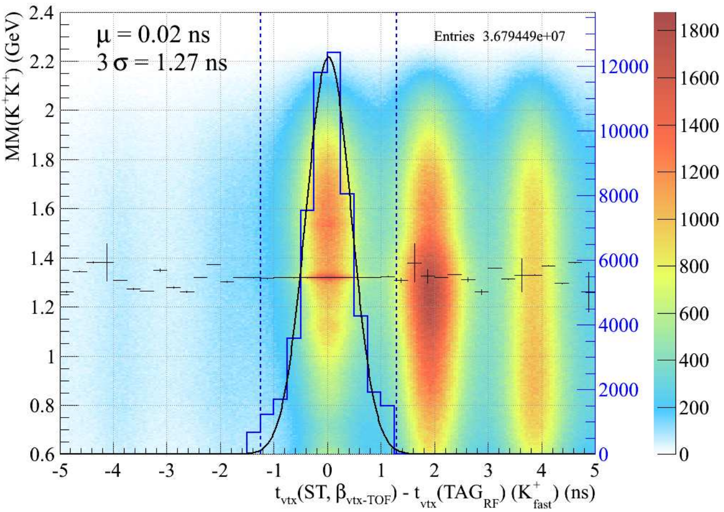

Figure 3.16: Missing mass off K^+ K^+ versus the difference in vertex time from the tagger and the start counter for the faster K^+. See Fig. 3.14 for a detailed explanation of this plot.

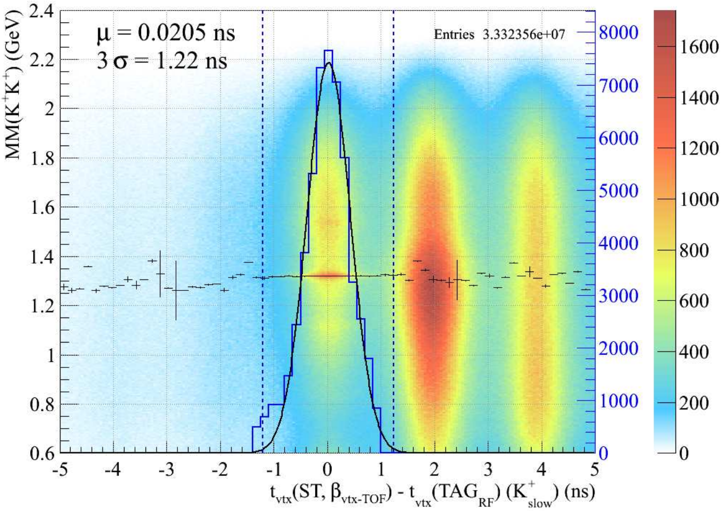

Figure 3.17: Missing mass off K^+ K^+ versus the difference in vertex time from the tagger and the start counter for the slower K^+. See Fig. 3.14 for a detailed explanation of this plot.

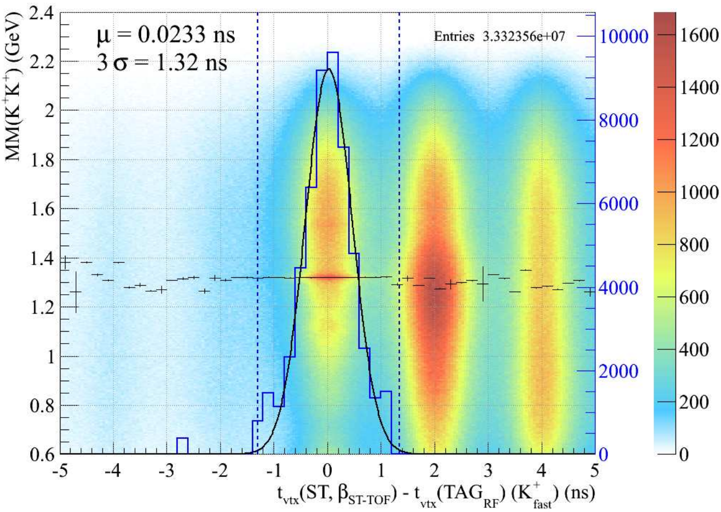

Figure 3.18: Missing mass off K^+ K^+ versus the difference in vertex time from the tagger and the vertex time from the start and time-of-flight counters for the faster K^+. See Fig. 3.14 for a detailed explanation of this plot.

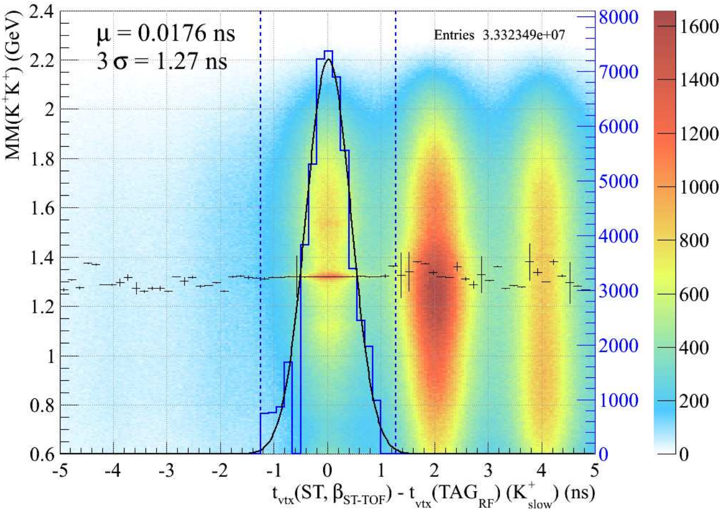

Figure 3.19: Missing mass off $K^+ K^+$ versus the difference in vertex time from the tagger and the vertex time from the start and time-of-flight counters for the slower K^+. See Fig. 3.14 for a detailed explanation of this plot.

The relative vertex time of the two K^+ tracks, after the previous timing selections, is within 1 ns, though an additional cut is made as shown in Fig. 3.20. The reconstruction program provides an estimate of the vertex position for each track which is calculated as the point of closest approach to the center of the beam-line. Using the momentum and this vertex position, the distance of closest approach (`DOCA`) and the midpoint of the shortest line connecting the two tracks are calculated, which is defined as the *intersection*. Doing this for the two K^+'s yields the data presented in Figs. 3.21–3.23. Event selections are made based on the z and radial positions of the intersection as well as the `DOCA` of the two tracks. Note that the `DOCA` is equivalent to measuring the co-planarity of the two tracks. These cuts are listed in Table 3.3.

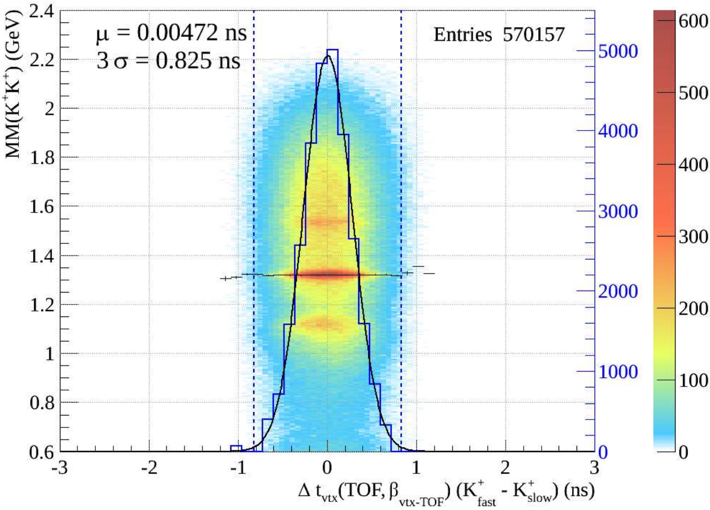

Figure 3.20: Missing mass off K^+ K^+ versus the difference in vertex time between the two kaons. See Fig. 3.14 for a detailed explanation of this plot.

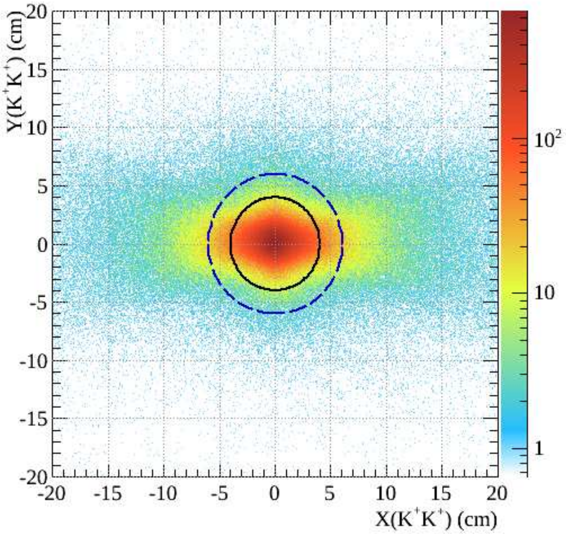

Figure 3.21: (x,y) of the intersection of the two K^+'s in reaction (3.23) on page 97. The dashed circle drawn is part of the K^+K^+ vertex position cut; the solid circle indicates the target wall. See Fig. 3.14 for a detailed explanation of this plot.

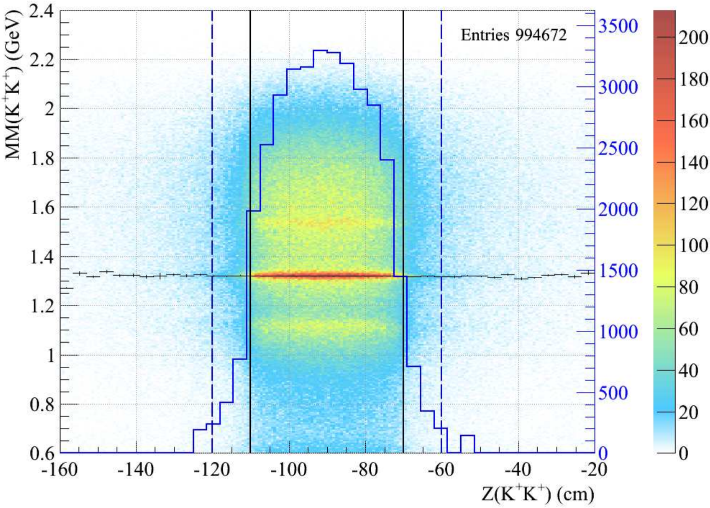

Figure 3.22: Missing mass off the K^+ K^+ versus the z-coordinate of the closest approach of the two K^+ tracks. The solid vertical lines indicate the target wall while the dashed lines are the z-position part of the vertex cuts. See Fig. 3.14 for a detailed explanation of this plot.

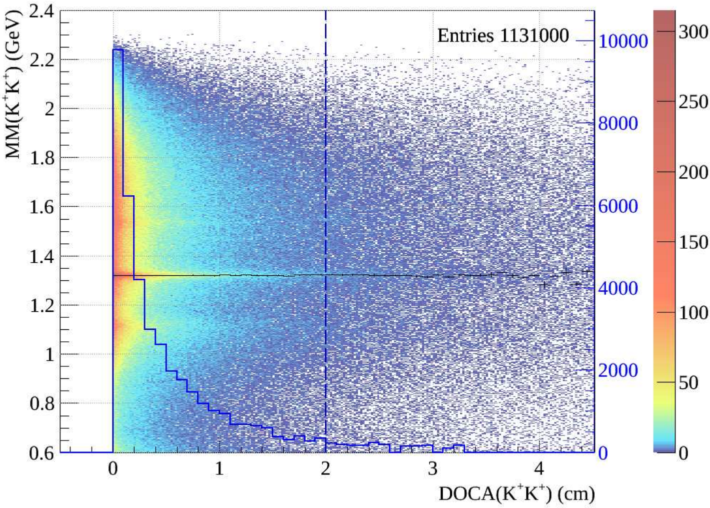

Figure 3.23: Missing mass off the K^+ K^+ versus the distance of closest approach for the two K^+ tracks. The dashed line indicates the `DOCA`(K^+K^+) cut used in this analysis. See Fig. 3.14 for a detailed explanation of this plot.

The timing of additional particles in the K^+K^+ analysis, such as an additional pion or proton, are shown in Figs. 3.24 and 3.25. The cuts made for the cascade decays are lower-bound only since the pions or protons may come from a Λ which may have traveled some measurable distance before decaying to $N\pi$.

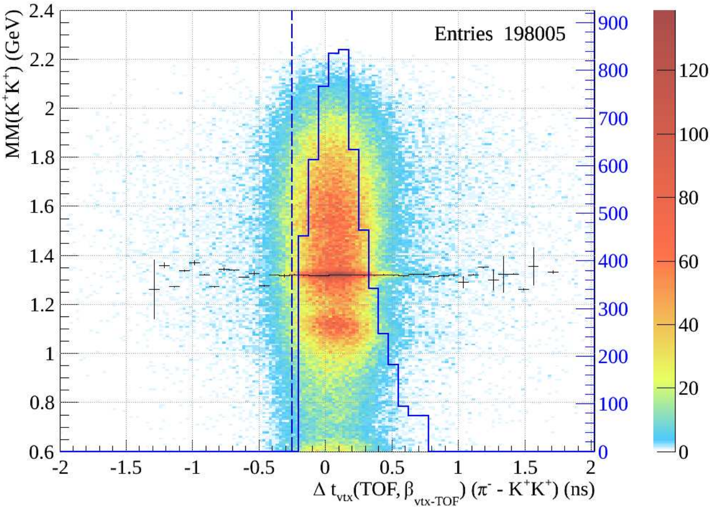

Figure 3.24: Missing mass off the K^+K^+ versus the difference in vertex time between the two kaons and the π^-. The dashed line shows the pion vertex timing cut. See Fig. 3.14 for a detailed explanation of this plot.

Table 3.3: Various cuts as described in Figs. 3.20–3.25 which are used in this analysis.

quantity	selection
$\lvert\Delta t_{\mathrm{vtx}}\rvert(\mathrm{K}^+_{\mathrm{fast}} - \mathrm{K}^+_{\mathrm{slow}})$	< 0.855 ns
$\mathtt{DOCA}(\mathrm{K}^+\mathrm{K}^+)$	< 2 cm
$\mathrm{K}^+\mathrm{K}^+$ intersect:	
$\quad (x^2 + y^2)^{\frac{1}{2}}$	< 6 cm
$\quad \lvert z + 90\rvert$	< 30 cm
Invariant Mass $(\mathrm{K}^+\mathrm{K}^+)$	> 1.005 GeV
$\mathrm{K}^+_{\mathrm{slow}}$ momentum	> 0.25 GeV
$\Delta t_{\mathrm{vtx}}(\text{proton} - \mathrm{K}^+\mathrm{K}^+)$	> -0.50 ns
$\Delta t_{\mathrm{vtx}}(\pi^- - \mathrm{K}^+\mathrm{K}^+)$	> -0.25 ns

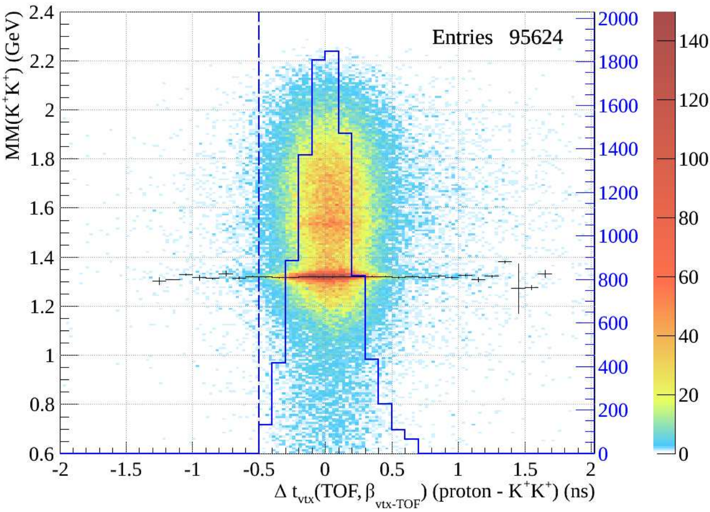

Figure 3.25: Missing mass off the K^+K^+ versus the difference in vertex time between the two kaons and the proton. The dashed line indicates the proton vertex timing cut. See Fig. 3.14 for a detailed explanation of this plot.

3.4 Beam Photon Identification

Particle identification, especially kaon-pion separation, is ambiguous in many kinematic regions of `CLAS`. When the luminosity of the beam is high enough to give more than one tagger hit in time with the identified tracks, things get even more complicated. Obtaining the correct tagger hit gives a measurement of the incident photon energy and allows missing masses to be calculated. These calculations are critical for this analysis where the acceptance for the full reaction:

$$\begin{aligned} \gamma p \to\ & \Xi^- K^+ K^+ \\ & \hookrightarrow \Lambda\pi^- \\ & \qquad \hookrightarrow p\pi^-, \end{aligned} \tag{3.22}$$

is less than 0.1%. Measuring the missing mass off the K^+K^+ provides the strangeness information for the baryon, its mass and momentum. This technique only requires two charged tracks which keeps acceptance higher at approximately 7%.

The tagger hit that triggered the event (the `MORA` or `MORB` trigger signals) is not necessarily the interacting photon. For higher luminosity runs such as *g12*, the tagger is hit many times during the `CLAS` trigger gate. The probability that there are two tagger hits within the same 2 ns beam bucket is approximately 17%. This is not to be confused with the accidental rate which makes up about two-thirds of the data taken in *g12* (see Sec. 2.2.1). **These** are real photoproduction events where the tagging of the photon is ambiguous.

Approximately 17% of the $\gamma p \to K^+K^+X^-$ events used for this analysis have more than a single photon hit in the same beam bucket as shown in Figs. 3.26 and 3.27. The yield of $\gamma p \to \Xi^-(1320)K^+K^+$ events in Figs. 3.28, 3.29 and 3.30 are summed up in Table 3.4. The fit used for these yields consisted of a 3rd order polynomial background with a Gaussian peak as discussed in Sec. 3.6. In a sample of 100k events that contained more than one tagger hit in the beam bucket associated with the tracks, 353 ± 42 ground state cascades were found using the second-highest (lower) photon energy. The highest energy photon yielded 516 ± 47 ground state cascades, and the events in this sample that contained only one tagger hit in this beam bucket had 3615 ± 118 ground state Ξ^-'s. This means that 12.5% of the Ξ events in this analysis have this tagger ambiguity. Furthermore, since the highest energy was chosen throughout the rest of this work, approximately 8.5% Ξ events were lost. To take this effect into account, tagger hits from a random sampling of data events were added to each simulated event used for the acceptance calculations.

The total photon flux for the data used in this analysis is shown in Fig. 3.31 and makes up roughly 90% of the total statistics obtained during the *g12* experiment. This is used in the excitation function calculations as described in Sec. 4.1.5. The difference in flux above and below 3.6 GeV is due to the difference in trigger bits as listed in Table 2.7. This effect of the relative trigger efficiencies was taken into account in the flux as opposed to the acceptance (see Sec. 4.1.2). This shift is model independent, however there is still an overall scaling factor

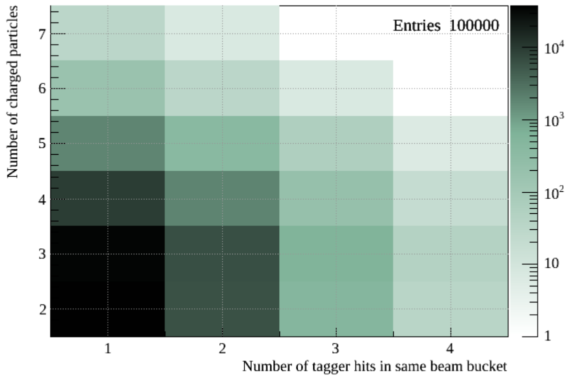

Figure 3.26: Number of charged particles detected in the drift chamber as a function of the number of tagger hits within the same beam bucket. Shown is a typical sampling of 100k events with at least two reconstructed charged tracks.

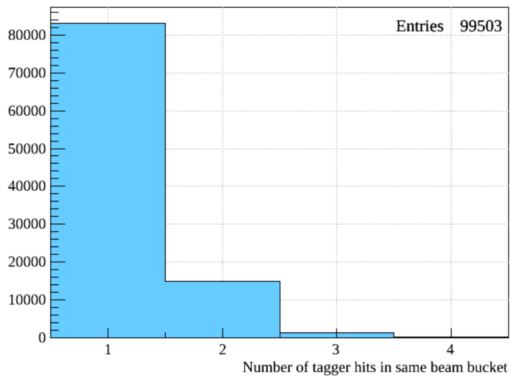

Figure 3.27: Number of tagger hits within the same beam bucket. This is the projection of Fig. 3.26 onto the x-axis.

that will be applied over the entire energy range which is discussed in Sec. 4.1.4.

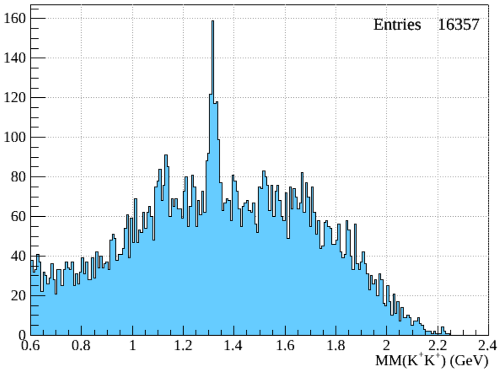

Figure 3.28: Missing mass off K^+K^+ where the event has more than one tagger hit in-time with the beam bucket associated with the tracks, and where the *lower* energy tagger hit was used (or second highest in case of more than two) to calculate the beam photon energy. This is from a sample of 100k events and the ground state $\Xi^-(1320)$ peak contains 353 ± 42 events.

Table 3.4: The yield of ground state $\Xi^-(1320)$ events in a sample of 100k K^+K^+ events with timing cuts as shown in Tables 3.2 and 3.3. The "single tagger hit" events have only one tagger hit in the beam bucket associated with the tracks. The others have more than one, and "highest" indicates the highest energy photon was used in the missing mass calculation while "lower" means the second highest was used.

	$\Xi^-(1320)$ yield per 100k events	percent of single + higher
single tagger hit:	3615 ± 118	87.5%
multiple - highest:	516 ± 47	12.5%
multiple - lower:	353 ± 42	8.5%

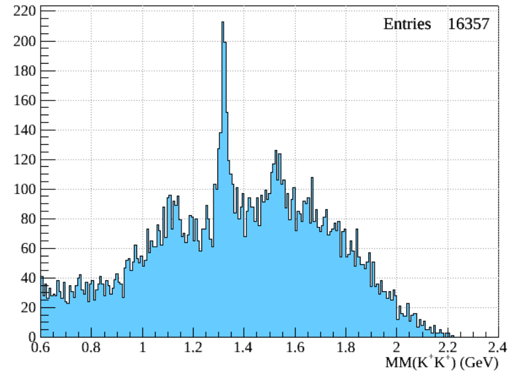

Figure 3.29: Missing mass off K^+K^+ where the event has more than one tagger hit in-time with the beam bucket associated with the tracks, and where the *highest* energy tagger hit was used to calculate the beam photon energy. This is from a sample of 100k events and the ground state $\Xi^-(1320)$ peak contains 516 ± 47 events.

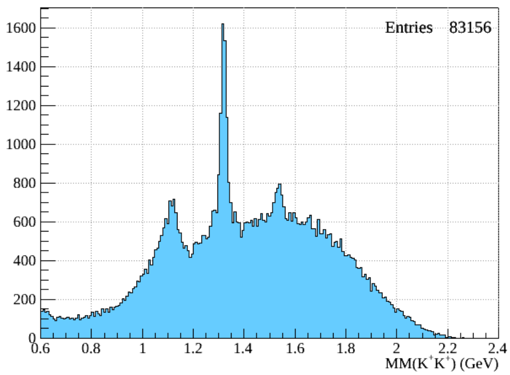

Figure 3.30: Missing mass off K^+K^+ where the event has only one tagger hit in the beam bucket associated with the tracks. This is from a sample of 100k events and the ground state $\Xi^-(1320)$ peak contains 3615 ± 118 events.

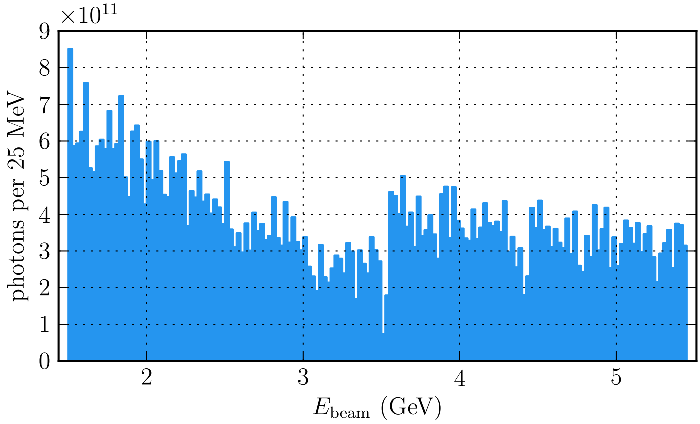

Figure 3.31: Total photon flux vs. beam energy.

3.5 TOF Energy Deposit

The time-of-flight (TOF) paddles in CLAS are all 5.08 cm (2 inches) thick. This is enough to obtain an accurate measurement of the energy deposited by the charged particles passing through it. Since heavier mass particles will deposit more energy at a given momentum, this can be used to identify particles independently from the β measurement as discussed earlier. The TOF energy deposit vs. momentum of the tracks is shown for protons, pions and kaons in Fig. 3.32. The pion and proton signals have been normalized to kaon signal in this figure to enhance the visibility of the kaons which are shown alone in Fig. 3.33.

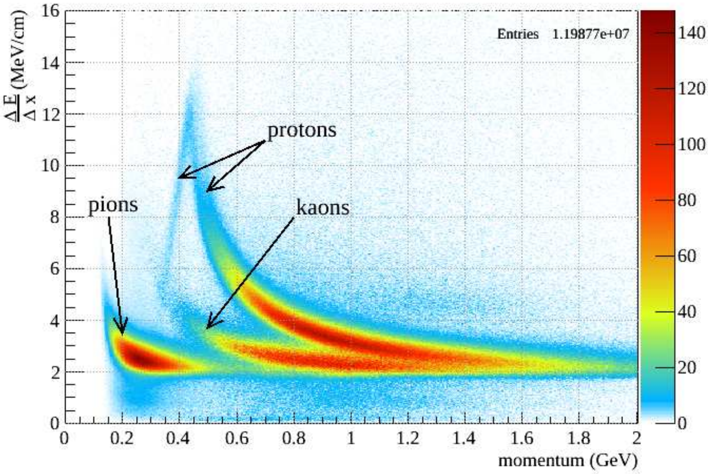

Figure 3.32: TOF energy deposit by charged pions, kaons and protons. The three histograms (protons, kaons and pions) were normalized to each other to enhance the identification of the kaon band. The pions and protons were selected from Λ events, and the kaons were selected where the missing mass off K^+K^+ is near the $\Xi^-(1320)$ mass or where the invariant mass of K^+K^- is near the $\varphi(1020)$ mass.

A summary of the time-of-flight cut used in this analysis is shown in App. B on page 139. The event selections made were done as a "consistency check" with the particle identification from the method described in Sec. 3.1. That is, tracks identified from the momentum and β calculation as protons, pions or kaons, passed the TOF energy cut if the energy deposit was consistent with this same particle identification. The values used (listed below) were experimentally determined, in order to take resolutions into account, based on the kaons in Fig. 3.33 and protons and pions in the *exclusive* reaction $\gamma p \to p\pi^-\pi^+$.

The effect of the the TOF energy deposit cut is discussed in Sec. 3.6. While the signal to background ratio is improved for the $\Xi^-(1320)$ and the $\Xi^-(1530)$ states, the statistics are reduced by 75% and therefore the evaluation of the

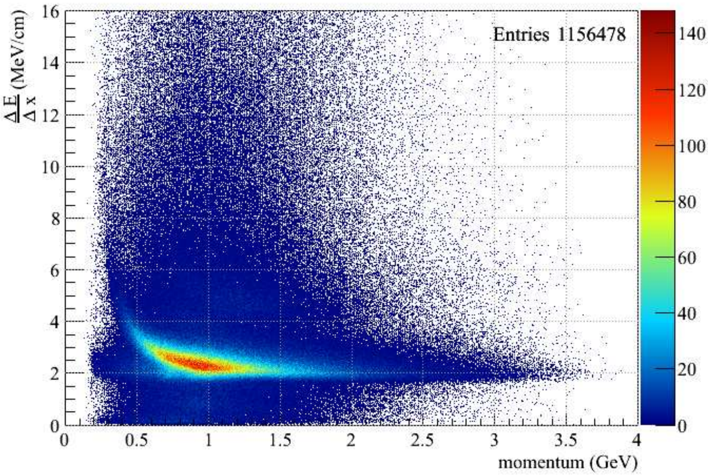

Figure 3.33: TOF energy deposit by kaons where the missing mass off K^+K^+ is near the $\Xi^-(1320)$ mass or the invariant mass of K^+K^- is near the $\phi(1020)$ mass.

excitation functions for these two were done with and without this cut.

3.6 Missing Mass Off K^+K^+

The skim of the *g12* data set used for this analysis required two charged tracks that were fully reconstructed in the DC. One of these tracks was required to be a *possible* positive or negative kaon. Here, *possible* meant all particles that had a measured mass approximating that of the kaon, all pions that had a momentum above 2 GeV and all protons that had a momentum above 3 GeV. This was done to include all kaon tracks that might be misidentified as either a pion or proton. Again, the cuts were done to minimize the effect of the pion and protons contaminating the K^+K^+ data.

In the reaction:

$$\gamma p \to K^+K^+X^-, \tag{3.23}$$

one can identify the X^- as a doubly-strange baryon (i.e. a Ξ^- resonance). The missing mass off the two K^+'s gives the mass of the cascade which could be some excited state. Since this procedure only requires identification of the incident photon (γ) and two K^+'s, the acceptance of CLAS is relatively high (about 7% as discussed in Sec. 4.1.2). This provides a good starting point for investigating the cascades produced in the *g12* experiment. This technique is sensitive to all decay channels of the "missing" state and therefore provides a straightforward method to study the *total production rates* of the cascades without the need to consider branching ratios.

To begin, the basic particle identification from the reconstruction was used, and most of the event selections were based on the yield of the ground state $\Xi^-(1320)$ as detailed in Sec. 3.3. The initial missing mass spectrum, with the minimal timing cuts listed in Table 3.2, is shown in Fig. 3.2 on page 69. From there, the additional timing and vertex selections, listed in Table 3.3, were added to produce Fig. 3.34.

The missing mass off K^+K^+ with the TOF energy deposit cut, as well as the vertex and timing cuts of Tables 3.2 and 3.3, is shown in Fig. 3.35. The signal to background ratio is improved, though the statistics are reduced by 75%. Notice the ground state Σ^- peak persists indicating misidentified pions are still present in this data.

The peak around 1.1 GeV in Fig. 3.34 indicates that there are pions which were misidentified as kaons in these plots. The reaction for these events is:

$$\begin{aligned}\gamma p \to \Sigma^-(1198)K^+\pi^+,\\ \hookrightarrow n\pi^-,\end{aligned} \tag{3.24}$$

where the neutron decay of the $\Sigma^-(1198)$ state occurs nearly 100% of the time. Requiring a proton in the K^+K^+ missing mass plot removes these misidentified pion events though not necessarily higher state Σ's or Λ's. This proton cut, along with the timing selection for the proton as listed in Table 3.3 is shown in Fig. 3.36. Just as with the TOF energy cut, the signal to background ratio is improved, however the statistics are greatly reduced. For completeness, the combination of the proton and the TOF energy cut is shown in Fig. 3.37 and a summary of the total measured yields for each of these is listed in Tables 3.5. The measured masses of the $\Xi^-(1320)$ and the $\Xi^-(1530)$ states are shown in Table 3.6 for each of the major event selections described.

All the Ξ states will have a Λ in the decay chain nearly 100% of the time and this Λ will decay to $p\pi^-$ approximately 67% of the time. An excited Σ^{*-} state on the other hand has the ground state decay $(\Sigma^-\pi^0)$ available which will decay via a neutron and therefore is less likely to produce a proton in the final state:

$$\begin{aligned} \gamma p \to \Sigma^{*-}&K^+\pi^+, \\ &\hookrightarrow \Sigma^-\pi^0 \\ &\qquad\hookrightarrow n\pi^-. \end{aligned} \tag{3.25}$$

This difference in the proton decay branching ratios of the Σ and Ξ states is used throughout this analysis as an internal check of the signal fitting procedure discussed in Sec. 4.1. The agreement in the final excitation functions with and without the proton requirement indicates that the handling of the background discussed in Sec. 4.1 is done correctly.

The proton cut does not remove all misidentified pions. Higher mass Σ's may decay to a proton and contribute to the background shape seen in Fig. 3.36.

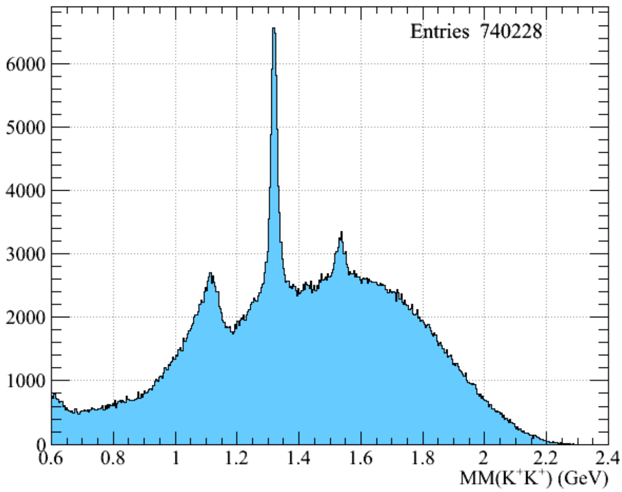

Figure 3.34: Missing mass off K^+K^+ in the reaction $\gamma p \to K^+K^+X^-$ with cuts as described in Tables 3.2 and 3.3 which include all the basic timing and vertex cuts, but not requiring a proton in the event or the `TOF` energy cut. The rise in events at 0.6 GeV corresponds to the enhancement in Fig. 3.9(d). The $\Xi^-(1320)$ and $\Xi^-(1530)$ signals peak at 1320.0 ± 0.1 and 1533.8 ± 0.7 MeV respectively.

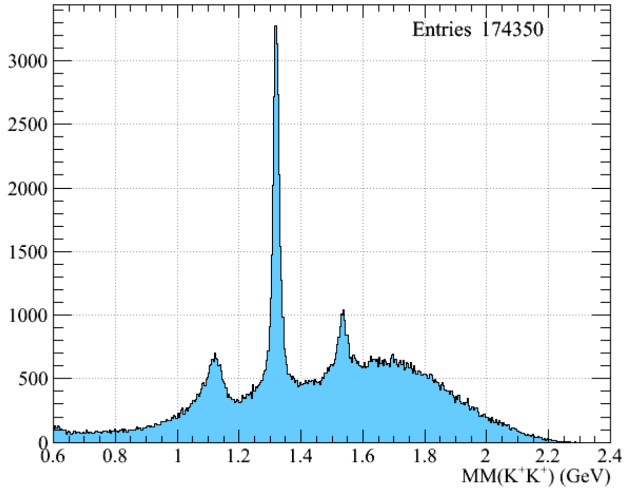

Figure 3.35: Missing mass off K^+K^+ in the reaction $\gamma p \to K^+K^+X^-$ with cuts as described in Tables 3.2 and 3.3 which include all the basic timing and vertex cuts, but not requiring a proton in the event. Here, the `TOF` energy deposit cut, as described in Sec. 3.5, was done on the two K^+'s in the final state. The $\Xi^-(1320)$ and $\Xi^-(1530)$ signals peak at 1320.3 ± 0.1 and 1534.8 ± 0.6 MeV respectively.

The influence of these states is mitigated by the fact that, for higher mass Ξ^{*-} states, the kaons will have a lower momentum (see Fig. 3.3 on page 70) and therefore are less likely to be misidentified as shown in momentum vs. β plot in Fig. 2.14 on page 64. Furthermore, these Σ^* states are generally broad (over 100 MeV) and overlap as shown in Fig. 3 on page 7. This suggests that their overall contribution to Figs. 3.34–3.35 will be smooth and can be approximated by low-order polynomial background fit used in this analysis.

Pion misidentification is not the only source of background in the missing mass off K^+K^+ distributions. As discussed in Sec. 3.4, there are typically over 20 tagger hits in each event and there is an 8.5% probability that the wrong hit was associated with the tracks. This will yield a vertex time that is off by some multiple of 2 ns and a photon energy which will be randomly determined from the distribution shown in Fig.3.31. The vertex time shift will contribute to the already existing source of noise from the particle identification scheme and is tied to the momentum and timing resolutions of the tracks. All of these contributions are reduced by the various vertex and timing cuts made, but cannot be eliminated entirely.

The background sources discussed so far stem from the inefficiencies of the detector, reconstruction algorithms and analysis techniques. There are some possible *real physics* sources where the detected particles are what they are measured to be, but where the event does not include a Ξ state. One such reaction includes the φ meson which can decay to K^+K^-:

$$\begin{aligned} \gamma p \to\ & \Lambda\varphi K^+ \\ & \quad\hookrightarrow\ K^+K^-. \end{aligned} \tag{3.26}$$

In this reaction, there are two K^+'s and possibly a proton in the final state. The beam energy threshold for this reaction is 2.9 GeV and with an additional 300 MeV to detect the two K^+'s, this process will start to interfere with the Ξ distribution at about 3.5 GeV. Because the K^+'s do not come from the same resonance, the contribution to the missing mass will be broad. Therefore, this may not affect any narrow Ξ resonance structures at the sensitivity level of this experiment and other φK^+ events can be treated in the same way.

One final contribution to the background in the missing mass off K^+K^+ distribution considered is the pion emission of the Y^* in the decay to the Ξ state:

$$\begin{aligned} \gamma p \to\ & Y^{*\prime}K^+ \\ & \hookrightarrow\ Y^*\pi^0 \\ & \qquad\hookrightarrow \Xi^{*-}K^+. \end{aligned} \tag{3.27}$$

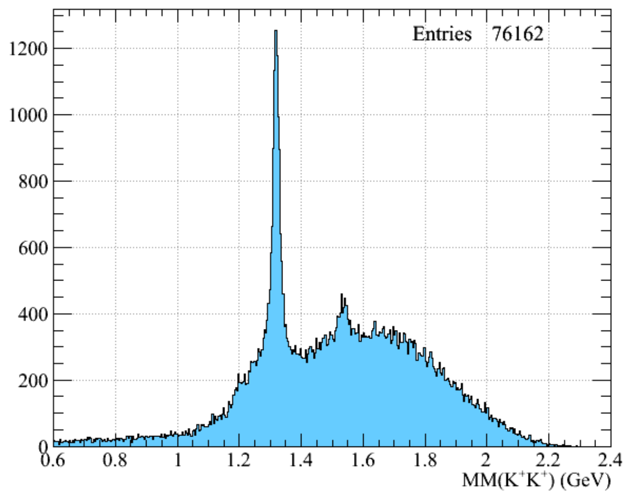

Figure 3.36: Missing mass off K^+K^+ in the reaction $\gamma p \to pK^+K^+X^{--}$ with cuts as described in Tables 3.2 and 3.3 which include all the basic timing and vertex cuts with the added requirement of a final-state proton in the event. The `TOF` energy deposit cut was not used on this data. The $\Xi^-(1320)$ and $\Xi^-(1530)$ signals peak at 1319.8 ± 0.2 and 1535.5 ± 1.2 MeV respectively.

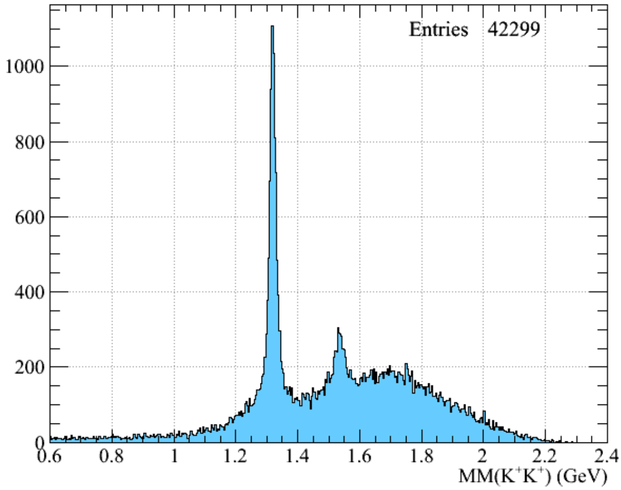

Figure 3.37: Missing mass off K^+K^+ in the reaction $\gamma p \to pK^+K^+X^{--}$ with cuts as described in Tables 3.2 and 3.3 which include all the basic timing and vertex cuts with the added requirement of a final-state proton in the event. In addition, the `TOF` energy deposit cut, as described in Sec. 3.5, was done on the two K^+'s and the proton in the final state. The $\Xi^-(1320)$ and $\Xi^-(1530)$ signals peak at 1319.9 ± 0.2 and 1536.5 ± 1.0 MeV respectively.

This reaction will contribute a broad overall shape for the same reasons as reaction (3.26). The relative contributions of all these sources of background would require significant time and effort to determine accurately and little would be gained over the technique of fitting the background to a low-order polynomial. The treatment of fitting a Gaussian signal with a 3$^{\text{rd}}$ order polynomial background shape to the data is described in Sec. 4.1.

The missing mass off $K^+K^+\pi^-$ in the reaction

$$\gamma p \to K^+K^+\pi^-X^0, \tag{3.28}$$

is shown in Fig. 3.38. The X^0 is identified as a doubly-strange neutral baryon, i.e. the $\Xi^0(1315)$ state corresponding to the peak at 1.3 GeV. The narrow peak at 1.1 GeV corresponds to the $\Lambda\pi^-$ decay of the ground-state $\Xi^-(1320)$. The broader peak just to the left, at 1.05 GeV, corresponds to the $\Lambda\pi^-$ decay of the $\Xi^0(1315)$ state where the π^- in the missing mass calculation is from the $p\pi^-$ decay of the Λ. Finally, the peak at 0.8 GeV corresponds to the same $\Sigma(1198)$ events in Figs. 3.2 and 3.11 where a π^+ was misidentified as a K^+.

The $\Xi^0(1315)$ events in Fig. 3.38 can come from either a Ξ^{*-} decay:

$$\begin{aligned} \gamma p \to\ & \Xi^{*-} K^+ K^+ \\ & \hookrightarrow \Xi^0 \pi^-, \end{aligned} \tag{3.29}$$

or the neutral kaon channel:

$$\begin{aligned} \gamma p \to\ & K^{*0} \Xi^0 K^+ \\ & \hookrightarrow \pi^+ \pi^-. \end{aligned} \tag{3.30}$$

A more thorough investigation of the K^{*0} could lead to an excitation function of the neutral $\Xi^0(1315)$ state but is beyond the scope of this analysis.

The neutral pion was seen in the data via two-γ decay where the final-state

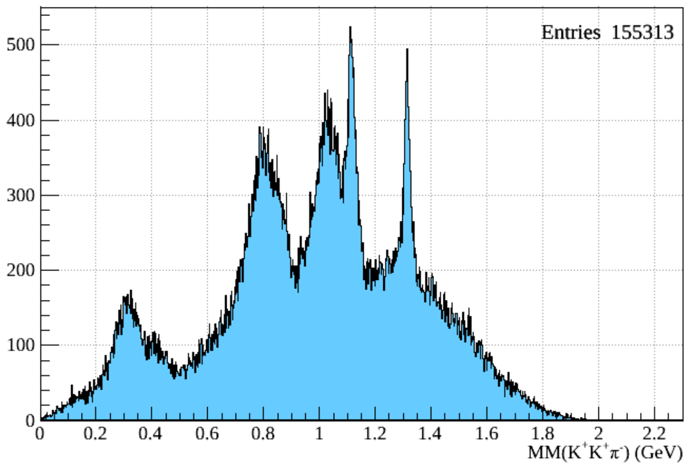

Figure 3.38: Missing mass off $K^+K^+\pi^-$ in the reaction $\gamma p \to K^+K^+\pi^- X^0$ with cuts as described in Tables 3.2 and 3.3. The peak at 300 MeV corresponds to events where both kaons were actually pions, see Fig. 3.9(d). The peak at 800 MeV corresponds to the $\Sigma(1189)$ events, see Fig. 3.9(c). The next peak at 1 GeV corresponds to Λ events where the π^- comes from the Λ decay. The narrow peak at 1.1 GeV is the $\Lambda(1115)$ with a measured mean of 1113.2 ± 0.2 MeV where the π^- came from the Ξ decay. Finally, the peak at 1.3 GeV corresponds to the neutral $\Xi^0(1315)$ with a measured mean of 1313.8 ± 0.4 MeV.

photons were detected by the EC. The two reactions:

$$\begin{aligned}\gamma p \to\ & \Xi^- K^+ K^+ \\ & \hookrightarrow \Lambda\pi^- \\ & \qquad \hookrightarrow n\pi^0 \\ & \qquad\qquad \hookrightarrow \gamma\gamma,\end{aligned} \tag{3.31}$$

$$\begin{aligned}\gamma p \to\ & \Xi^{*-} K^+ K^+ \\ & \hookrightarrow \Xi^- \pi^0 \\ & \qquad \hookrightarrow \gamma\gamma,\end{aligned} \tag{3.32}$$

show up in the missing mass off K^+K^+ (Fig. 3.39) as two peaks for the $\Xi^-(1320)$ and $\Xi^{*-}(1530)$ states. Unfortunately, the resolution of the π^0 is so poor that any invariant mass calculation is washed out, however, just requiring a π^0 in the event was effective in reducing the background around the $\Xi^-(1530)$ state. The measured masses of the two Ξ states where a π^0 was detected is listed in Table 3.6.

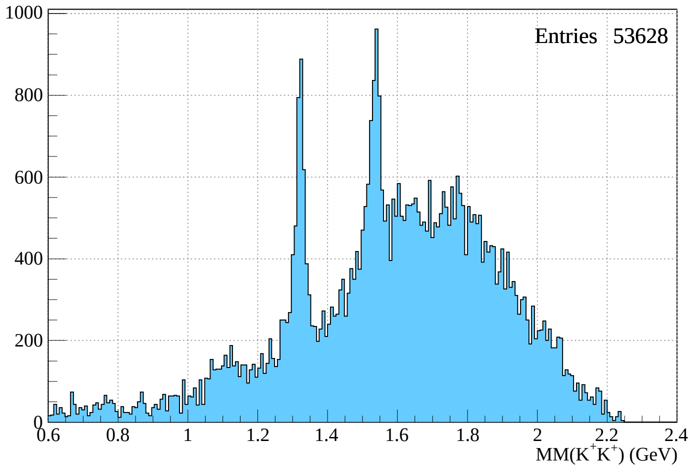

Figure 3.39: Missing mass off K^+K^+ in the reaction $\gamma p \to K^+K^+\pi^0 X^-$ with cuts as described in Tables 3.2 and 3.3. The $\Xi^-(1320)$ and $\Xi^-(1530)$ signals peak at 1320.9 ± 0.4 and 1535.3 ± 0.6 MeV.

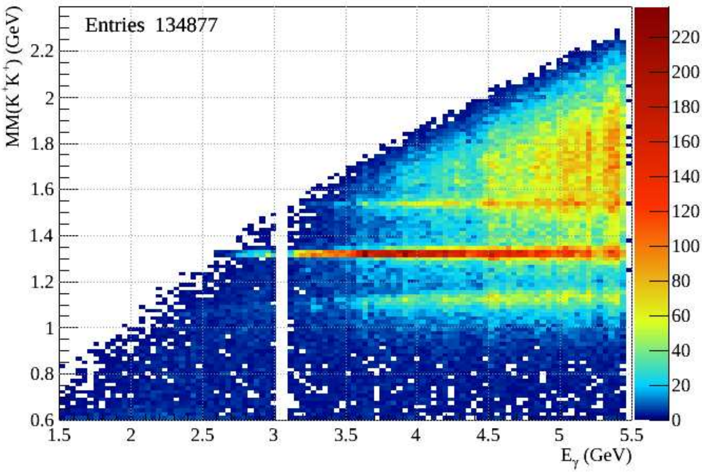

Figure 3.40: Missing mass off K^+K^+ vs. beam photon energy in the reaction $\gamma p \to K^+K^+X^-$ with cuts as described in Tables 3.2 and 3.3, and the TOF energy deposit cut.

Table 3.5: Total measured yields of the ground-state cascades, representing 90% of the total statistics collected in the *g12* experiment. Errors given are a two standard-deviation statistical error. The selections made on the data consist of those found in Tables: 3.2 and 3.3. This table shows the yields for the various cuts which include: requiring a proton in the event, the TOF energy deposit cut as described in Sec. 3.5 and requiring a π^0 in the event.

	total measured yield		
selections	$\Xi^-(1320)$	$\Xi^-(1530)$	Figure №
basic only	22690 ± 250	4330 ± 240	3.34
$E_{\mathtt{TOF}}$	15190 ± 150	3020 ± 120	3.35
proton	7557 ± 125	1310 ± 110	3.36
$E_{\mathtt{TOF}}$ & prot.	5025 ± 85	1073 ± 66	3.37
π^0	2451 ± 72	2622 ± 96	3.39

Table 3.6: Measured masses of the ground-state cascades, representing 90.0% of the total statistics collected in the *g12* experiment. Errors given are a two standard-deviation statistical error. This table shows the masses of the states for the various event selections which include: requiring a proton in the event, the TOF energy deposit cut as described in Sec. 3.5 and requiring a π^0 in the event.

	measured mass (MeV)		
selections	$\Xi^-(1320)$	$\Xi^-(1530)$	Figure №
basic only	1320.0 ± 0.1	1533.8 ± 0.7	3.34
$E_{\mathtt{TOF}}$	1320.3 ± 0.1	1534.8 ± 0.6	3.35
proton	1319.8 ± 0.2	1535.5 ± 1.2	3.36
$E_{\mathtt{TOF}}$ & prot.	1319.9 ± 0.2	1536.5 ± 1.0	3.37
π^0	1320.9 ± 0.4	1535.3 ± 0.6	3.39
average	1320.2 ± 0.2	1535.2 ± 0.8	
PDG[8]	1321.71 ± 0.07	1535.0 ± 0.6	

Chapter 4

Excitation Functions and Cross Section Upper Limits

This chapter presents the excitation function calculation for the ground state $\Xi^-(1320)$ starting with the measured yield from the missing mass off K^+K^+ in the reaction $\gamma p \to K^+K^+X^-$. This entire procedure was applied to the data with the basic timing cuts listed in Tables 3.2 and 3.3 and each combination of including a proton in the event and the time-of-flight energy deposit cut described in Sec. 3.5. The associated simulations and their contribution to the systematic error are discussed, concluding with the resultant excitation functions and comparison to previous results. The divisions in the beam energy were chosen so that percentage errors on both axes of the final excitation functions were comparable.

The same procedure, with slight modifications, was applied to obtain the excitation function of the $\Xi^-(1530)$ state as well as the cross section upper limits for the higher mass charged cascade states: $\Xi^-(1620)$, $\Xi^-(1690)$ and $\Xi^-(1820)$ and the iso-exotic candidates: Ξ^{--}, Ξ^+, Σ^{--} and Σ^{++}.

4.1 $\Xi^-(1320)$ Excitation Function Calculation

In this section, the calculations leading up to the excitation function of the $\Xi^-(1320)$ state are described in detail. These techniques are then used in the following sections, with certain modifications as discussed, to obtain the excitation function for the $\Xi^-(1530)$ state and the total cross section upper limits for the higher cascade and iso-exotic states. The process begins with the determination of the number of Ξ events seen. This "measured yield" is then divided by the photon flux. The length and material of the target are taken into account to obtain the "flux-corrected measured yield." This is presented as a detected cross section (detected σ) in units of picobarns and is the last step before applying any model to the calculation. The resonance-production model used in the simulation that produces the acceptance for each reaction introduces the largest systematic error and this is investigated in the following sections. The flux-corrected measured yield is then divided by the acceptance to obtain the final excitation function.

4.1.1 Measured Yield

The measured number of $\Xi^-(1320)$ events were determined by fitting a 3$^{\text{rd}}$ order polynomial background combined with a Gaussian distribution. For each state and beam-photon energy bin, the number of events in the peak (N) was obtained from taking the integral of the background-subtracted histogram, two standard deviations on either side of the mean. The number of background events (B) in the K^+K^+ missing mass was calculated as the integral of the polynomial part of the total fit over the same range. This played a large part in determining the statistical error of the measured yield:

$$\delta N = \sqrt{N + 2B}. \tag{4.1}$$

It is important to note that the peaks are not strictly Gaussian and the background shape does not follow a 3$^{\text{rd}}$ order polynomial perfectly. These shapes are not known on a fundamental level, however, as shown in Fig. 4.1, the estimate used here adequately fits the data. The systematic error introduced due to the fact that the peak and background shapes are unknown is small compared to the systematic error from the model used in the simulation, and as such, can be ignored.

The fit, shown in Fig. 4.1, is done for each photon energy bin in the subsequent yield and excitation function plots. Note that a sideband subtraction is inadequate here because it consistently under or over estimates the number of events depending on the sign of the 2$^{\text{nd}}$ derivative of the background shape. However, the sum of the sidebands on either side of the ground state $\Xi^-(1320)$, shown in Fig. 4.3, is used as a cross-check for the validity of the yield measurements. Since the events in the sideband are essentially random, the flux-corrected yield is expected to be smooth over the full energy range.

The measured number of $\Xi^-(1320)$ particles detected, labeled as "measured yield," is shown in Fig. 4.4. Correcting for the photon flux (F), the length of the target ($\ell = 40$ cm) and the target material (liquid hydrogen — $\ell\mathrm{H}_2$) gives the flux-corrected measured yield (Y), seen in Fig. 4.5:

$$Y = \frac{w}{\rho \ell N_A} \frac{N}{F}, \tag{4.2}$$

where w is the atomic weight of $\ell\mathrm{H}_2$ (1.00794), ρ is the density of $\ell\mathrm{H}_2$ ($0.0708\ \frac{\mathrm{g}}{\mathrm{cm}^3}$) and N_A is Avogadro's number (6.022×10^{23}). The statistical error of this yield is

$$\delta Y = Y \times \left(\frac{\delta N^2}{N^2} + \frac{1}{F} \right)^{\frac{1}{2}}, \tag{4.3}$$

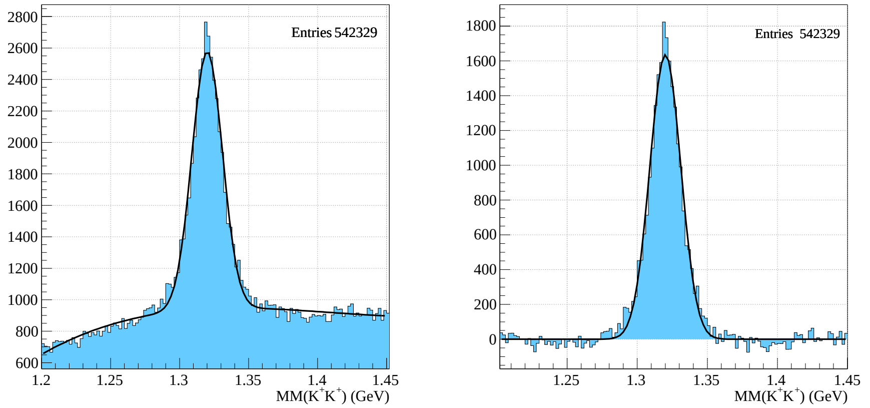

Figure 4.1: The ground state $\Xi^-(1320)$ peak from the data in Fig. 3.34 is fitted with a 3$^{\text{rd}}$ order polynomial plus a Gaussian on the range from 1.2 to 1.45 GeV. The polynomial is subtracted from the histogram on the right.

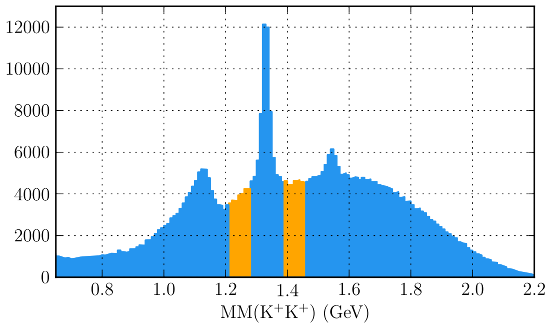

Figure 4.2: Sidebands in orange: 3σ to 6σ on either side of the ground state $\Xi^-(1320)$ from the data in Fig. 3.34. The integral of the sidebands as a function of beam energy is shown in Fig. 4.3.

where the statistical error of the flux is given by Poisson statistics:

$$\delta F = \sqrt{F}. \tag{4.4}$$

The value Y is labeled in the following figures as the "detected total cross section (σ)" since it is equal to the total cross section times the acceptance for this reaction. It is the closest result presented before any model is introduced into the calculation. As discussed in the following sections, this choice of model brings with it the largest source of systematic error but it is required to obtain the acceptance of the detector for the observed states.

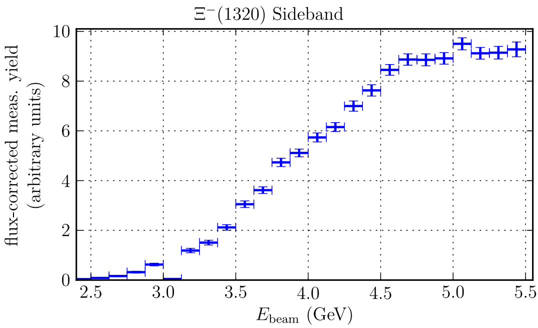

Figure 4.3: The measured sideband yield around the ground state $\Xi^-(1320)$ from the data in Fig. 3.34. The sideband range is from 3σ to 6σ on either side of the peak. These data have been divided by the photon flux and normalized to arbitrary units.

4.1.2 Acceptance

The cross sections presented in this work use an acceptance calculated from Monte Carlo (MC) simulations that include both geometry and detector response efficiency. Events were generated using an estimate of the excitation function of the state measured. These were fed into the tracking program (GSIM) which converted the generated tracks into detector element hits. These hits were then smeared to mimic the observed resolution of the detector subsystems using the program GPP. This program was also used to populate the tagger using a random sampling of events from the data. The acceptance (A) was determined for each photon energy bin as the ratio of reconstructed events (R) to generated events

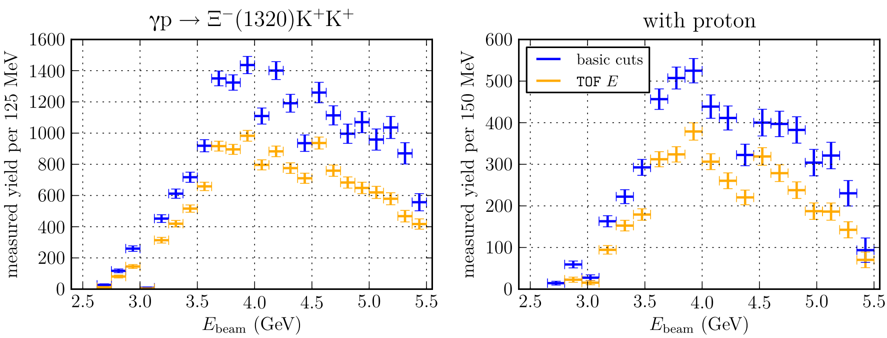

Figure 4.4: The measured yield of the ground state $\Xi^-(1320)$. Shown in both figures are the data with selections described in Tables 3.2 and 3.3 with and without the TOF energy deposit cut. The plot on the right has the added requirement of an in-time proton.

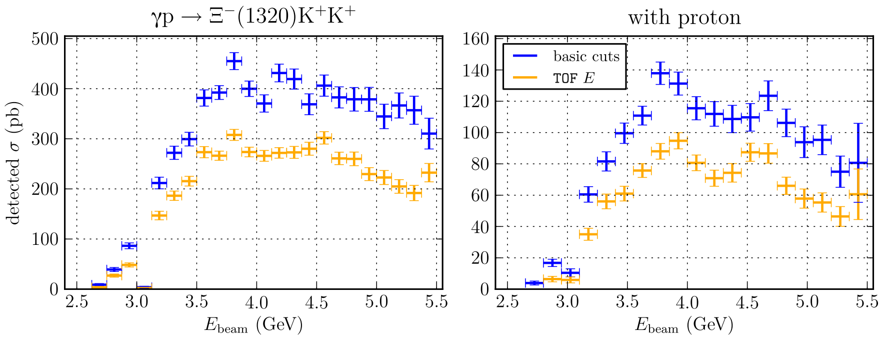

Figure 4.5: The flux-corrected measured yield (Y from Eq. 4.2) of the ground state $\Xi^-(1320)$. Shown in both figures are the data with selections described in Tables 3.2 and 3.3 with and without the `TOF` energy deposit cut. The plot on the right has the added requirement of an in-time proton.

(G):

$$A = \frac{R}{G}, \tag{4.5}$$

with a standard deviation for a binomial distribution as the statistical error:

$$\delta A = \sqrt{\frac{A(1-A)}{G-1}}. \tag{4.6}$$

The number of generated events (G) was chosen to be large enough so the statistical error in the acceptance would be much less than the error in the flux-corrected measured yield:

$$\frac{\delta A}{A} \ll \frac{\delta Y}{Y}, \tag{4.7}$$

and δA was added in quadrature to obtain the statistical error on the final results. The acceptance for the ground state $\Xi^-(1320)$ is shown in fig. 4.6. This was applied to the flux-corrected measured yield to obtain the final excitation function. An investigation into the validity of this calculation is presented in the following section.

The tracking and digitizing program is only reliable within a certain internal region of the drift chamber. At its edges, the magnetic field is not as well known, and a fiducial cut is required to prevent a significant contribution to the systematic error from events that lie along these edges. This cut, shown in Fig. 4.7, was applied to all data presented in this chapter (real and simulated) and a detailed specification is depicted in App. C.

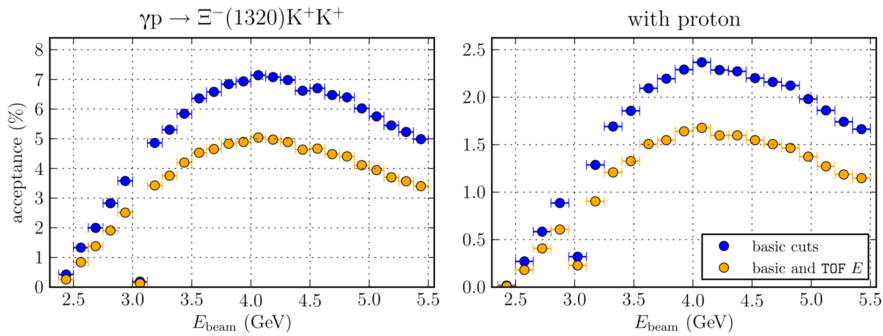

Figure 4.6: The acceptance for the ground state $\Xi^-(1320)$. Shown in both figures are the data with selections described in Tables 3.2 and 3.3 with and without the `TOF` energy deposit cut. The plot on the right has the added requirement of an in-time proton.

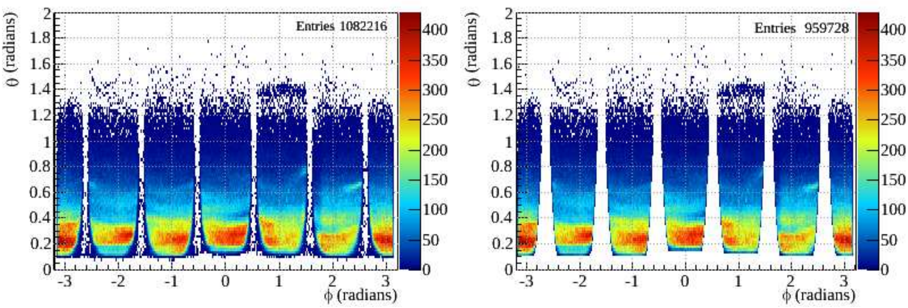

Figure 4.7: Angular distribution of the K^+ tracks showing the fiducial cut. Similar cuts were made for each type of particle.

4.1.3 Ξ Photoproduction Simulation Model

A theoretical study on the photoproduction of cascades was done in 2006[40, 41]. It was specifically concerned with the differential cross section of the ground state $\Xi^-(1320)$ as measured from the *g11* experiment. This was "a first step toward building a more complete and realistic model for describing cascade baryon photoproduction off nucleons[41]." The Ξ photoproduction total cross section calculated by Nakayama et al. is shown in Fig. 4.8. There is a scaling factor in the theoretical model which was adjusted to fit the *g11* data and good agreement was found with the shape of the total cross section. They also concluded that the dominant coupling of the baryon-hyperon-kaon vertexes (pseudovector or pseudoscalar) could be determined by measuring the target asymmetry as a function of the Ξ state angle in the center-of-mass frame.

The contributing production amplitudes to the calculations done by Nakayama et al. are shown in Fig. 4.9. Contact currents and higher mass intermediate kaon processes were also included in the calculations but are not shown here. The primary diagram used in this analysis is Fig. 4.9(a) which is a t-channel kaon exchange. As discussed in the following sections, the t-slope of the reaction and the Y^* mass and width were tuned so that the simulated kaon momentum and angular distributions matched that of the data. This could only be done for the ground and first excited Ξ states and so an estimate was made for the extrapolation through 1820 MeV for the higher mass Ξ candidates.

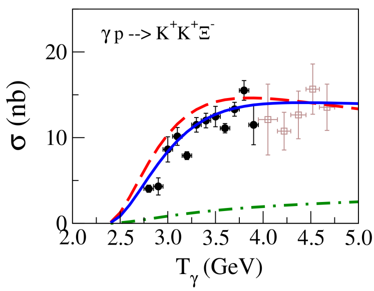

Figure 4.8: Theoretical calculation of the $\Xi^-(1320)$ excitation function calculated (shown by the solid blue line) by Nakayama et al.(Fig. 2(a) in Ref. [41]) based on *g11* results. The plot shown is for pseudovector coupling at the baryon-hadron-kaon vertex and the equivalent plot for pseudoscalar is similar in shape and magnitude.

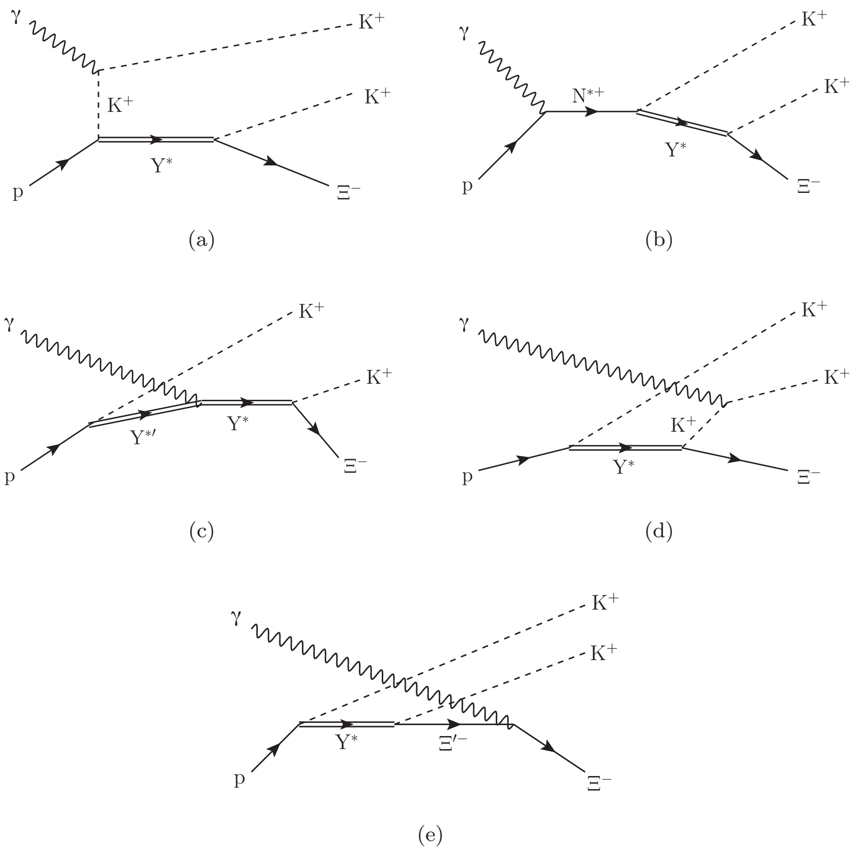

Figure 4.9: Ξ photoproduction diagrams which were used in the theoretical work by Nakayama et al.[40, 41]. There were also generalized contact currents and processes similar to (a) and (d) where the t-channel K meson was replaced by a K^*. The acceptance calculated in this work used only diagram (a) for the simulations of the ground state $\Xi^-(1320)$ where the t-slope and Y^* mass and width was tuned to produce agreement with the kaon distribution in the data as shown in Figs. 4.10 and 4.19.

4.1.4 `MC` Model Dependence and Systematic Errors

Requiring a model to generate simulated events for calculating acceptances is one of the largest sources of systematic error. A phase-space generator is insufficient to reproduce the distributions of momenta in the data. For this analysis, a t-channel production via kaon exchange and a Y^{*0} resonance was used to simulate the Ξ production, making the parameters for event generation the mass and width of the Y^{*0} and the "t-slope" of the leading K^+. The simulated reaction is:

$$\begin{aligned}\gamma p \rightarrow\ & Y^{*0}K^{+} \\ & \hookrightarrow \Xi^{-}K^{+},\end{aligned} \tag{4.8}$$

and the ground state Ξ^- is allowed to decay using GEANT3's physics processing routines. The t-slope is the exponential slope constant b in

$$-t = ae^{-bE}, \tag{4.9}$$

where E is the beam energy and t is the Mandelstam invariant corresponding to the momentum transfer to the leading K^+:

$$t = (p^{\mu}_{\text{beam}} - p^{\mu}_{K^+})^2, \tag{4.10}$$

where p^{μ}_{beam} and $p^{\mu}_{K^+}$ are the four-vector momenta of the incident photon and leading K^+ respectively. An approximation of this distribution using the higher momentum K^+ can been seen in the upper-left plot of Fig. 4.10. The values for the Y^{*0} mass, width and the t-slope were chosen to mimic the distributions in the data as shown in Fig. 4.10 and the systematic error was determined by varying them according to the features seen in the data.

The acceptance for the Ξ states is sensitive to the t-slope of the leading K^+, however, this kaon cannot be identified in the data since there are two identical K^+'s in the final state. Luckily, a reasonable approximation exists using the higher momentum K^+ as the leading meson in reaction (4.8). The t-slope for this kaon as a function of beam energy is shown in Fig. 4.11 for both the $\Xi^-(1320)$ and $\Xi^-(1530)$ states. The Y^{*0} mass and width can similarly be ascertained from the missing mass off the faster K^+. This is shown in Figs. 4.12 and 4.13. The parameters used for the acceptance calculations of the Ξ states are listed in Table 4.1.

Table 4.1: The simulation parameters used to calculated the acceptance for the various Ξ states.

	t-slope	Y^{0*} mass (GeV)	Y^{0*} width (MeV)
$\Xi^-(1320)$	1.4	1.95	500
$\Xi^-(1530)$	1.7	2.1	500
$\Xi^-(1620)$	1.7	2.25	700
$\Xi^-(1690)$	1.7	2.5	1000
$\Xi^-(1820)$	1.7	2.7	1000

The systematic error of the acceptance coming from the Y^{*0} mass, width and t-slope: $\delta A_{M(Y^*)}$, $\delta A_{\Gamma(Y^*)}$ and $\delta A_{t\text{-slope}}$ respectively, was calculated from the variance of the acceptance from events simulated using $M(Y^*) = 2.1$ GeV, $\Gamma(Y^*) = 200$ MeV and t-slope$= 2.0$ each individually and summing these in quadrature. For each of these variations, the contribution to the systematic error is given by

$$\delta A_{\rm sys}^2 = \frac{1}{N}\sum_i \left(\frac{A_i^{\rm var} - A_i}{A_i}\right)^2, \tag{4.11}$$

where the sum is over N photon energy bins, A_i is the acceptance used in the excitation function calculations, and $A_i^{\rm var}$ is the acceptance for one of the three variations above. The comparison for each is shown in Figs. 4.14 and 4.15 and the variation in the acceptance as a function of the model parameters is:

$$\begin{aligned}\frac{\delta A_{\rm M(Y^*)}}{A} &= 1.2\%,\\ \frac{\delta A_{\Gamma(\rm Y^*)}}{A} &= 1.0\%,\\ \frac{\delta A_{t\text{-slope}}}{A} &= 2.3\%.\end{aligned} \tag{4.12}$$

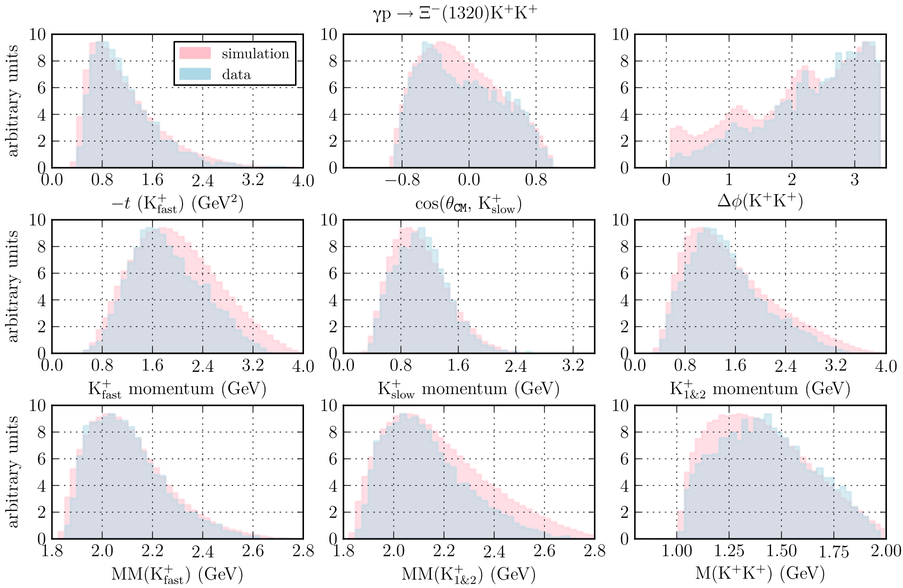

Figure 4.10: Comparison of simulation of the $\Xi^-(1320)$ to the background-subtracted data, normalized by height. From left to right, top to bottom: $-t$ from the high momentum K^+, cosine of the center-of-mass polar-angle ($\theta_{\tt CM}$) of the low momentum K^+, the azimuthal angular difference ($\Delta\phi$) between the two K^+'s, the momenta of each K^+, the missing mass off the high momentum K^+ and the invariant mass of K^+K^+. The label "$K^+_{1\&2}$" denotes the sum of the histograms for each K^+.

Adding these together gives an estimated *minimum* systematic uncertainty of 4.5% in the acceptance. Although this study was done with the ground state $\Xi^-(1320)$, it is reasonably certain to hold for each of the higher mass Ξ's and is incorporated into the final results.

There are other sources of systematic error which can be accounted for by an overall scale factor. These include the start counter inefficiency which was not included in the smearing program (`GPP`) of the simulation. This inefficiency was determined to be 6% per track with the *g11*[37] experiment which had very similar running conditions for beam current, target and start counter. An overall efficiency that was dependent on the beam intensity was also found. This scaled linearly with the current and was approximately 16% at 60 nA, or 0.26% per nA. The *g11* group also included a scaling factor due to multiple hits in the tagger within the same beam bucket. The last scaling factor was accounted for in this analysis by populating the tagger in the simulated events as discussed in Sec. 3.4 on page 90.

For the final excitation function results, a scale factor of 28% was applied to the K^+K^+ events and 34% was applied when a proton was detected in the event. These numbers are based on the findings from *g11*. Our estimate of the systematic error is 7%. Adding this to the 4.5% error above gives a minimum systematic error of 12%.

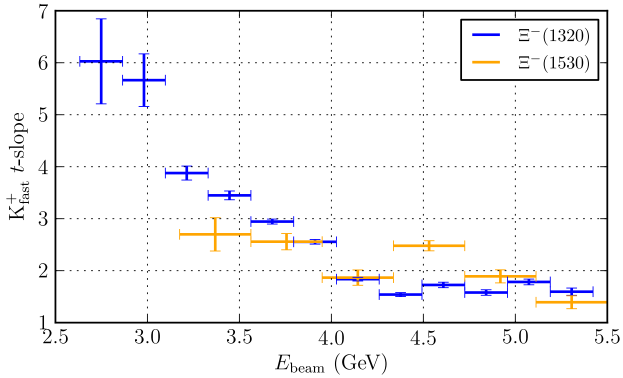

Figure 4.11: Measured t-slope from K^+_{fast} for the $\Xi^-(1320)$ and $\Xi^-(1530)$ obtained via sideband subtraction.

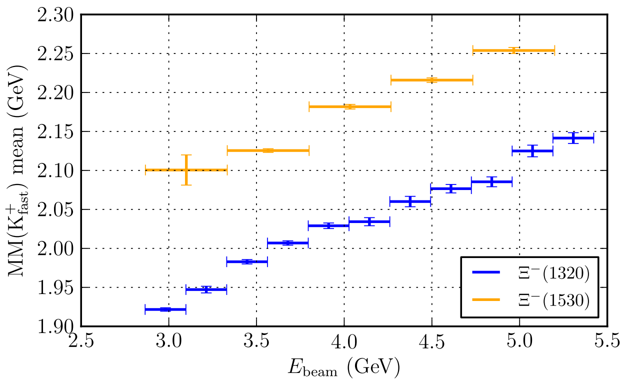

Figure 4.12: Mean of the missing mass off K^+_{fast} for the $\Xi^-(1320)$ and $\Xi^-(1530)$ obtained via sideband subtraction.

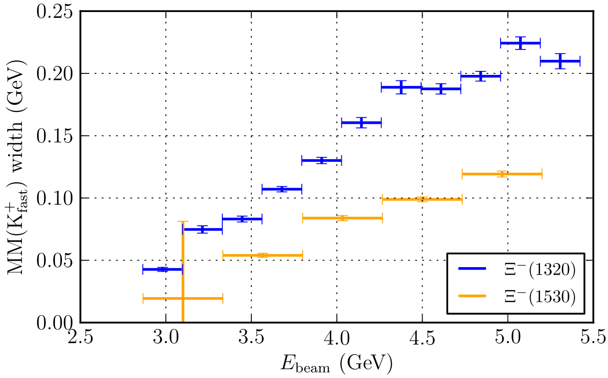

Figure 4.13: Gaussian width (σ) of the missing mass off K^+_{fast} for the $\Xi^-(1320)$ and $\Xi^-(1530)$ obtained via sideband subtraction.

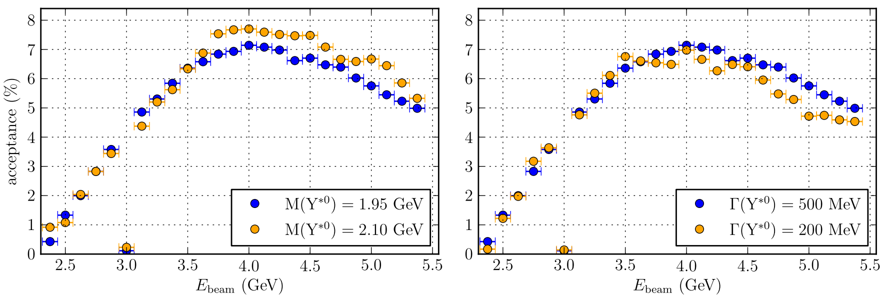

Figure 4.14: Acceptance for the ground state $\Xi^-(1320)$ showing the effect of varying the Y^{*0} mass and width.

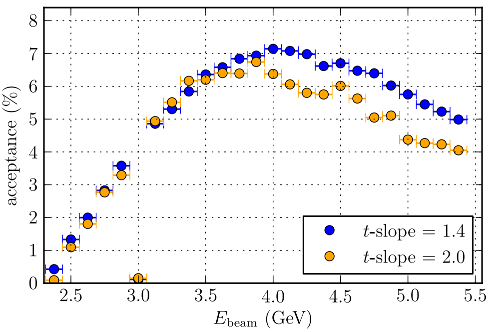

Figure 4.15: Acceptance for the ground state $\Xi^-(1320)$ showing the effect of varying the t-slope parameter.

4.1.5 Excitation Function

The flux-corrected measured yield divided by the acceptance is shown in Fig. 4.16 as the final excitation function of the ground state $\Xi^-(1320)$. The error bars indicate the statistical error only and the minimum systematic error is estimated to be 12%.

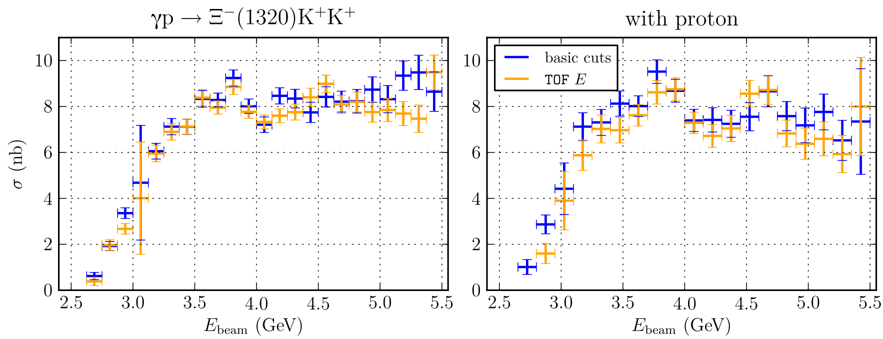

Figure 4.16: Excitation function for the $\Xi^-(1320)$. Shown in both figures are the data with selections described in Tables 3.2 and 3.3 with and without the `TOF` energy deposit cut. The plot on the right has the added requirement of an in-time proton.

4.2 $\Xi^-(1530)$ Excitation Function

The measured yield for the first excited $\Xi^-(1530)$ state is shown in Figs. 4.17 and 4.18. This resonance has two distinct decay channels:

$$\begin{aligned}\gamma p \rightarrow\; & \Xi^{*-}(1530)K^+K^+ \\ & \hookrightarrow \Xi^-(1320)\pi^0,\end{aligned} \tag{4.13}$$

$$\begin{aligned}\gamma p \rightarrow\; & \Xi^{*-}(1530)K^+K^+ \\ & \hookrightarrow \Xi^0(1315)\pi^-.\end{aligned} \tag{4.14}$$

Simulation of the $\Xi^-(1530)$ state consists of both of these decays combined according to the isospin of the decay products ($\Xi\pi$). The subsequent decay of the ground state Ξ's to a Λ, and ultimately to a proton, are all considered kinematically equivalent in this estimation. There are two cascades in each of the octet and decuplet (see Fig. 2 on page 3) and so the Ξ's have total isospin $\frac{1}{2}$. The I_3 component of the Ξ^- is $-\frac{1}{2}$ while for the Ξ^0 it is $\frac{1}{2}$. Using the notation

$|I\ I_3\rangle$:

$$\begin{aligned}\Xi^{*-}(1530) &= \left|\tfrac{1}{2}\ {}^{-}\tfrac{1}{2}\right\rangle,\\ \Xi^{-}(1320) &= \left|\tfrac{1}{2}\ {}^{-}\tfrac{1}{2}\right\rangle,\\ \Xi^{0}(1315) &= \left|\tfrac{1}{2}\ {}^{+}\tfrac{1}{2}\right\rangle,\end{aligned} \tag{4.15}$$

and the pions have isospin of 1:

$$\begin{aligned}\pi^0 &= |1\ 0\rangle,\\ \pi^- &= \left|1\ {}^{-}1\right\rangle.\end{aligned} \tag{4.16}$$

Using the Clebsch-Gordan coefficients[8] yields the relative amplitudes for each possible total isospin of the two decay modes:

$$\Xi^-\pi^0 = \left|\tfrac{1}{2}\ {}^{-}\tfrac{1}{2}\right\rangle|1\ 0\rangle = \sqrt{\frac{2}{3}}\left|\tfrac{3}{2}\ {}^{-}\tfrac{1}{2}\right\rangle + \sqrt{\frac{1}{3}}\left|\tfrac{1}{2}\ {}^{-}\tfrac{1}{2}\right\rangle, \tag{4.17}$$

$$\Xi^0\pi^- = \left|\tfrac{1}{2}\ {}^{+}\tfrac{1}{2}\right\rangle\left|1\ {}^{-}1\right\rangle = \sqrt{\frac{1}{3}}\left|\tfrac{3}{2}\ {}^{-}\tfrac{1}{2}\right\rangle - \sqrt{\frac{2}{3}}\left|\tfrac{1}{2}\ {}^{-}\tfrac{1}{2}\right\rangle. \tag{4.18}$$

Since the isospin of the $\Xi^{*-}(1530)$ state is $\left|\tfrac{1}{2}\ {}^{-}\tfrac{1}{2}\right\rangle$, the relative branching ratio to these decay channels is

$$\frac{\Gamma(\Xi^{*-} \to \Xi^-\pi^0)}{\Gamma(\Xi^{*-} \to \Xi^0\pi^-)} = \frac{1}{2}. \tag{4.19}$$

The data shown in Figs. 4.19 and 4.20 consist of both channels combined with a weighted (2 : 1) average. The comparison of the simulation to the data, via sideband subtraction of the $\Xi^-(1530)$ state, shows less agreement than with the ground state $\Xi^-(1320)$, but it is still within a systematic error of 4%. Finally, the excitation function for the $\Xi^-(1530)$ state, with and without the time-of-flight energy deposit cut and proton requirement, is shown in Fig. 4.21. This includes the scaling factors discussed in the previous sections.

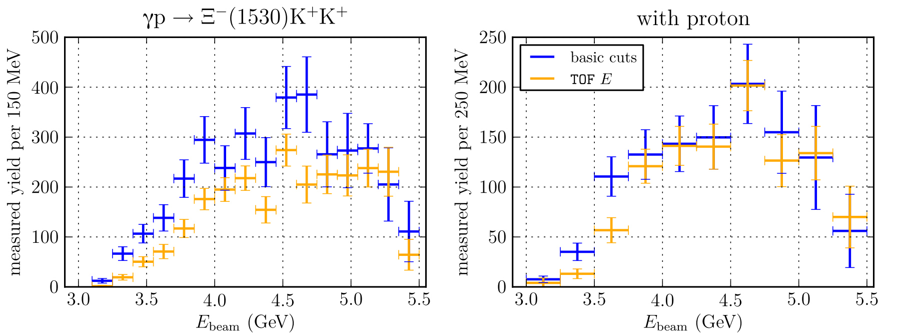

Figure 4.17: The measured yield of the $\Xi^-(1530)$. Shown in both figures are the data with selections described in Tables 3.2 and 3.3 with and without the `TOF` energy deposit cut. The plot on the right has the added requirement of an in-time proton.

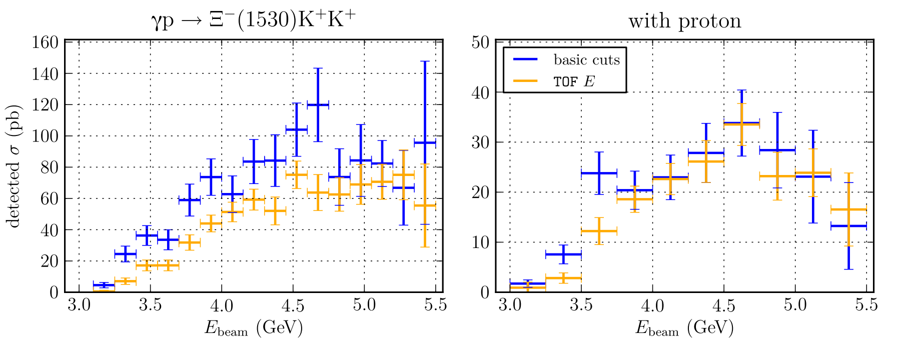

Figure 4.18: The flux-corrected measured yield (Y from Eq. 4.2) of the $\Xi^-(1530)$. Shown in both figures are the data with selections described in Tables 3.2 and 3.3 with and without the `TOF` energy deposit cut. The plot on the right has the added requirement of an in-time proton.

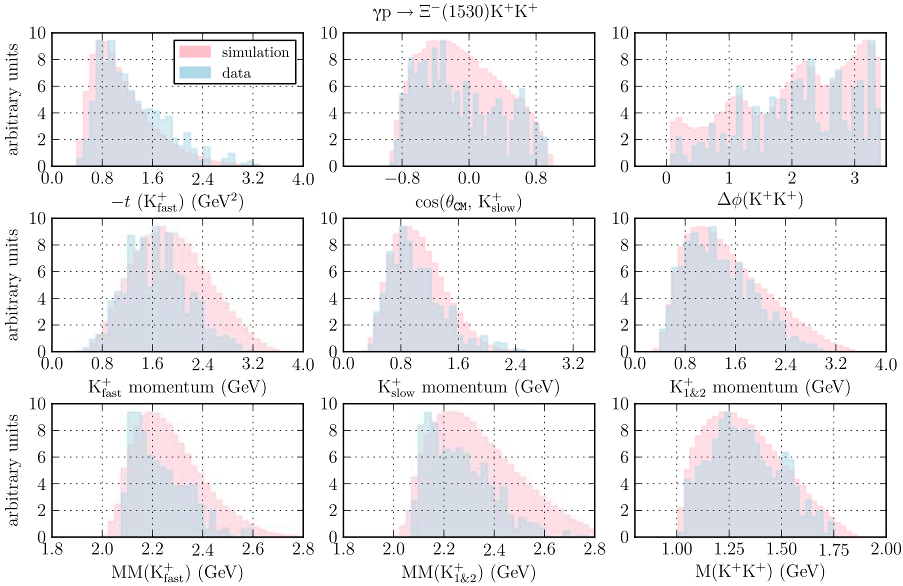

Figure 4.19: Comparison of simulation of the $\Xi^-(1530)$ to the background-subtracted data, normalized by height. From left to right, top to bottom: $-t$ from the high momentum K^+, cosine of the center-of-mass polar-angle (θ_{CM}) of the low momentum K^+, the azimuthal angular difference ($\Delta\phi$) between the two K^+'s, the momenta of each K^+, the missing mass off the high momentum K^+ and the invariant mass of K^+K^+. The label "$K^+_{1\&2}$" denotes the sum of the histograms for each K^+.

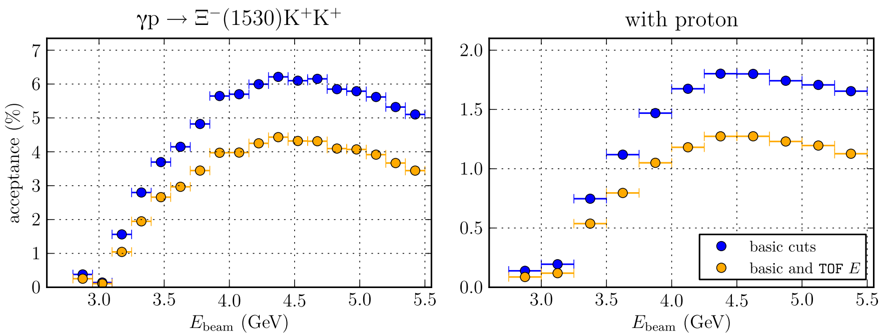

Figure 4.20: The acceptance for the $\Xi^{*-}(1530)$. Shown in both figures are the data with selections described in Tables 3.2 and 3.3 with and without the `TOF` energy deposit cut. The plot on the right has the added requirement of an in-time proton.

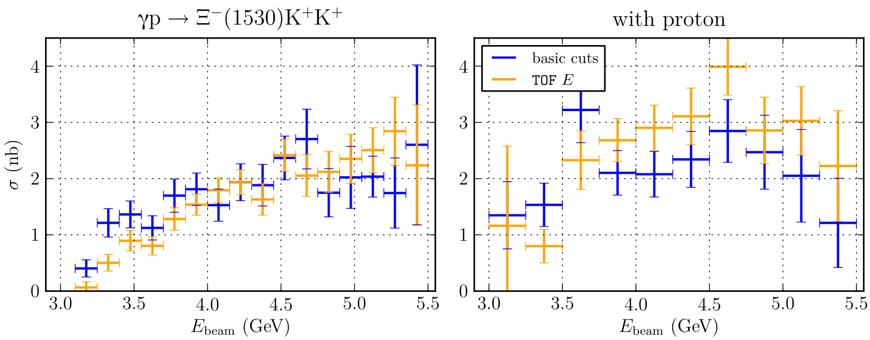

Figure 4.21: Excitation function for the $\Xi^-(1530)$. Shown in both figures are the data with selections described in Tables 3.2 and 3.3 with and without the `TOF` energy deposit cut. The plot on the right has the added requirement of an in-time proton.

4.3 Search for Higher Mass Cascades

For states that were not seen in the data, a variation on the above technique was used to determine the sensitivity of measuring a signal in a certain location — i.e. a predetermined mass and width. For each energy bin, the background shape was determined by fitting a 3$^{\mathrm{rd}}$ order polynomial at least six widths to either side of the mass. The parameters of this fit were then fixed and a Gaussian of fixed mean and width (following the values in Table 4.2) was added to the function. The only parameter allowed to vary was the height of the Gaussian peak. After this new function was fitted to the data, the integral of Gaussian, two standard deviations to each side of the mean, was calculated as the number of events "detected." The integral of the polynomial part over the same range gave the number of background events. The measured yield was verified to be consistent with zero and the two standard deviation error was taken as the upper limit of the measured yield shown in Fig. 4.22. The resulting flux-corrected yield is shown in Fig. 4.23. The acceptance, using the model described in Sec. 4.1.2 is shown in Fig. 4.24. Combining these, including the scale factor of 34%, yields the total cross section upper limits shown in Fig. 4.25. These show the results over several energy bins, each 250 MeV wide. Tables 4.3, 4.4 and 4.5 list the results integrated over the whole energy range.

Table 4.2: Masses and widths used to extract the upper limits for the Ξ candidates. The widths are estimates based on previous results and the resolution of the data.

	Mass (MeV)	Width (MeV)
$\Xi^-(1620)$	1620	25
$\Xi^-(1690)$	1690	35
$\Xi^-(1820)$	1820	30

Table 4.3: Upper limits for the measured yield and flux-corrected measured yield (detected σ) of the higher mass Ξ candidates over the entire energy range (3.5–5.5 GeV) with a confidence level of 90%.

	$< N$	$< Y$ (pb)
$\Xi^-(1620)$	274	5.88
$\Xi^-(1690)$	290	7.36
$\Xi^-(1820)$	244	7.41

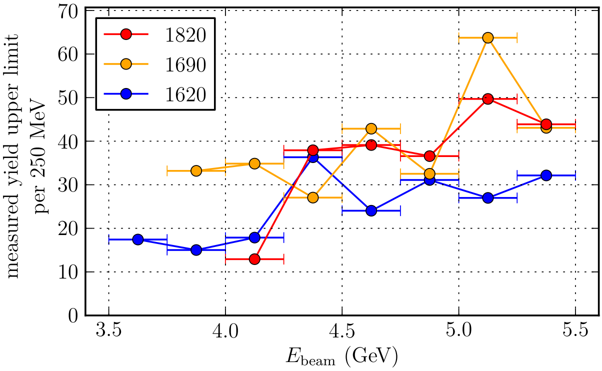

Figure 4.22: The upper limits of the measured yield of Ξ candidates at 1620, 1690 and 1820 MeV via the missing mass off K^+K^+ in the reaction $\gamma p \to pK^+K^+X^{--}$. Shown are the data with selections described in Tables 3.2 and 3.3 including the `TOF` energy deposit cut.

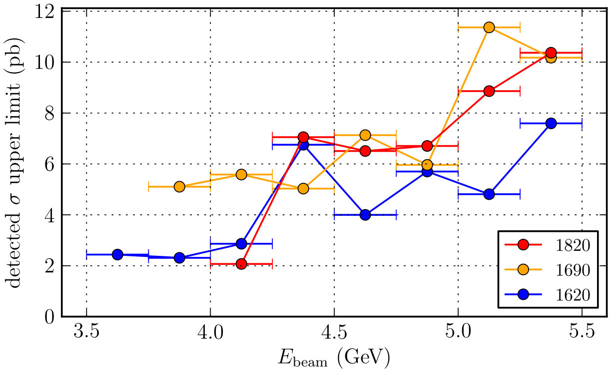

Figure 4.23: The upper limits of the flux-corrected measured yield of the Ξ candidates at 1620, 1690 and 1820 MeV via the missing mass off K^+K^+ in the reaction $\gamma p \to pK^+K^+X^{--}$. Shown are the data with selections described in Tables 3.2 and 3.3 including the `TOF` energy deposit cut.

Table 4.4: Acceptances calculated over the entire energy range (3.5–5.5 GeV) for the higher mass Ξ candidates. Shown are the number of events generated (G), reconstructed (R) and the acceptance (A) with an error given by Eq. 4.6.

	G (10^6)	R (10^3)	A (%)	δA (%)
$\Xi^-(1620)$	2.077	23.6	1.14	0.01
$\Xi^-(1690)$	2.000	22.9	1.15	0.01
$\Xi^-(1820)$	1.942	19.9	1.03	0.01

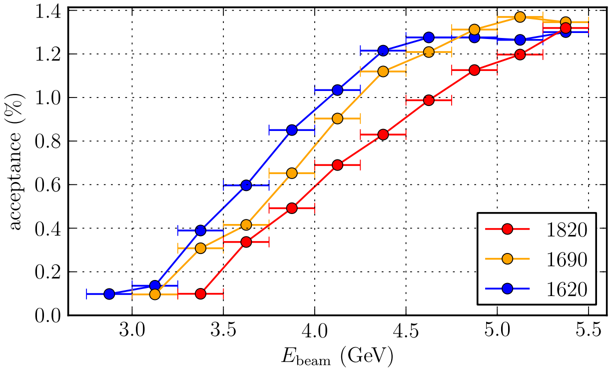

Figure 4.24: The acceptances of the Ξ^* candidates at 1620, 1690 and 1820 MeV.

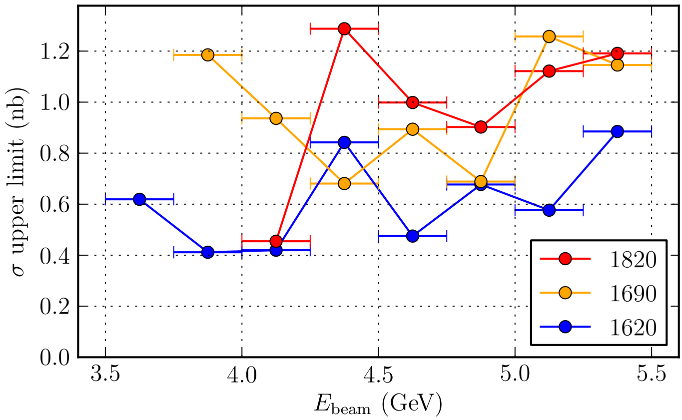

Figure 4.25: Total cross section upper limits for photoproduction of the $\Xi^-(1620)$, $\Xi^-(1690)$ and $\Xi^-(1820)$ candidates, including the scale factor of 34%.

Table 4.5: Upper limits for the total cross section of the higher mass Ξ candidates over the entire energy range (3.5–5.5 GeV) with a confidence level of 90% with and without the scale factor of 34% applied.

	no scale factor $<\sigma$ (pb)	34% scale factor $<\sigma$ (nb)
$\Xi^-(1620)$	516	0.78
$\Xi^-(1690)$	640	0.97
$\Xi^-(1820)$	720	1.09

4.4 Search for *Iso-exotic* States

The search for iso-exotic states presented here is qualitative in nature, since an accurate determination of the acceptance requires a model for the production mechanism. With the cascades, the Monte Carlo events were calibrated to the distributions of the kaons. A similar calibration was not possible with the iso-exotics because there were no analogous signals to the $\Xi^-(1320)$ and $\Xi^-(1530)$ states. Therefore, one can assume the upper limit for any state that is not seen in this data is *at most* on the order of 100 nb. Of course, this is an estimate based on the cascade states and it may easily be in the 1–10 microbarn range. In all the data shown here, basic timing cuts are applied to all particles and only the strong decays of the exotics are considered. The reasoning being that if the strong decay was suppressed somehow, these states would be narrow and would likely show up in the hadron-beam experiments discussed in Sec. 0.3.

A search was made for the Ξ^{--} state which has a strangeness and charge of -2. The state is looked for in the missing mass off $K^+K^+\pi^+$, shown in Fig. 4.26, in the reaction:

$$\gamma p \to \Xi^{--} K^+ K^+ \pi^+. \tag{4.20}$$

For an invariant mass search, only the purely-strong decays of the Ξ^{--} where all the final state particles carry electric charge were considered — there is only one, shown in Fig. 4.27:

$$\begin{aligned} \Xi^{--} &\to \Xi^- \pi^- \\ &\quad\hookrightarrow \Lambda\pi^- \\ &\qquad\hookrightarrow p\pi^-. \end{aligned} \tag{4.21}$$

This figure requires at least one K^+ in the event. Requiring two K^+ yields a total of four such events in the *g12* data set. The usual estimates for the mass of the Ξ^{--} include summing the masses of the Ξ^- state and a pion. This gives a mass of at least 1.5 GeV for the Ξ^{--} though predictions are generally higher and some go slightly above 2 GeV[39]. Notice that both Figs. 4.26 and 4.27 show no sign of a signal above the 1.5 GeV.

The next iso-exotic considered is the Ξ^+. All decay channels available to such a state must contain a neutral final state particle, most likely a $\pi^0 \to \gamma\gamma$ and therefore only the missing mass technique is used to look for this state. Fig. 4.28 shows the missing mass off $K^+\pi^+\pi^-\pi^-$ in the reaction:

$$\begin{aligned} \gamma p &\to \Xi^+ K^+ K^0 \pi^- \\ &\qquad\qquad\hookrightarrow \pi^+\pi^-. \end{aligned} \tag{4.22}$$

The peaks in this figure correspond to the proton and the $\Sigma^+(1189)$ — both where the K^+ was actually a π^+. The fits to the mean of these two peaks is listed in Table 3.1 on page 74. To verify that the peak just to the left of the proton is the proton in the event:

$$\gamma p \to pK^0\overline{K}^0 \to p\pi^+\pi^-\pi^+\pi^-, \tag{4.23}$$

the missing mass off of the $K^0\pi^+\pi^-$ where the π^+ was originally identified as a kaon plotted versus the missing mass off $K^+K^0\pi^-$ is shown in Fig. 4.29. Any Ξ^+ state higher in mass than the $\Sigma^+(1189)$, would show up as a vertical band in this plot or a peak in Fig. 4.28. No such structures are apparent in this data.

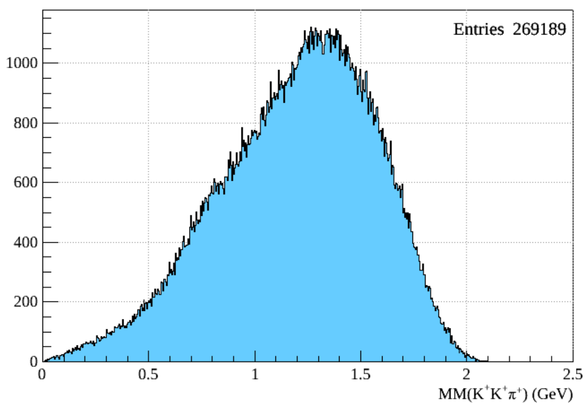

Figure 4.26: Search for Ξ^{--}: missing mass off $K^+K^+\pi^+$ in the reaction $\gamma p \to K^+K^+\pi^+X^{--}$.

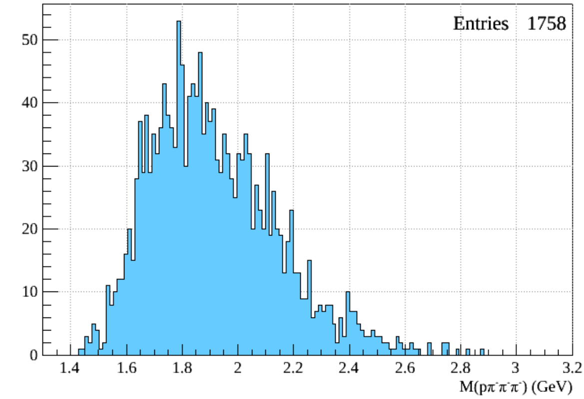

Figure 4.27: Search for Ξ^{--}: invariant mass of $p\pi^-\pi^-\pi^-$ in reaction (4.21) where the invariant mass of $p\pi^-$ is near the $\Lambda(1115)$. Requiring that this Λ and one the remaining pions is equal to the $\Xi^-(1320)$ mass reduces the statistics to less than 200 events.

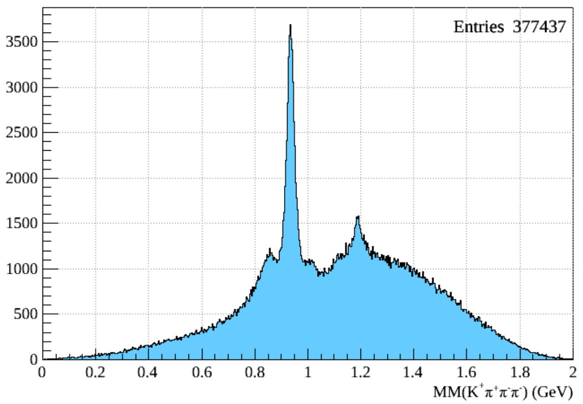

Figure 4.28: Search for Ξ^+: missing mass off $\pi^+K^0\pi^-$ in reaction (4.22) where the K^0 decayed to $\pi^+\pi^-$.

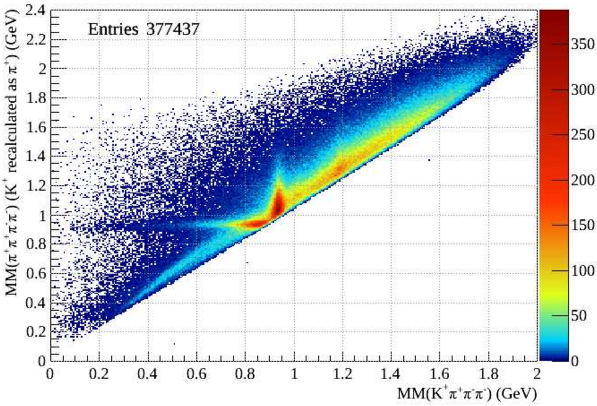

Figure 4.29: Search for Ξ^+: missing mass off $K^0\pi^+\pi^-$ where a K^+ was recalculated as a π^+ versus the missing mass off $K^+K^0\pi^-$. The horizontal band is the final-state proton in reaction (4.23) while the vertical band at 0.94 GeV is the proton in reaction (4.22). The $\Sigma^+(1189)$ can also be seen as a vertical band at 1.2 GeV.

There are two singly-strange baryon iso-exotic states that are looked for in this data. They are the doubly-charged Σ^{--} and Σ^{++} states. Like the Ξ^{--} and Ξ^{+}, these can not be made up of only three quarks in the Standard Model and are truly exotic in this theory. The Σ^{--} will always have a neutron as the final state baryon in the decays considered and therefore throwing out events with a detected proton is an effective cut. The missing mass off $K^+\pi^+\pi^+$ in these events is shown in Fig. 4.30.

The last iso-exotic state searched for in this analysis is the Σ^{++} which may decay to the Δ^{++}:

$$\begin{aligned} \Sigma^{++} \rightarrow \Delta^{++}\overline{K}^0, & \\ \Delta^{++} &\rightarrow p\pi^+, \\ \overline{K}^0 &\rightarrow \pi^+\pi^-. \end{aligned} \tag{4.24}$$

The invariant mass of the $\Delta^{++}\overline{K}^0$ in the above reaction is shown in Fig. 4.31 where there is no apparent resonance structure for a Σ^{++} state. The missing mass off $K^+\pi^-\pi^-$ in the production reaction:

$$\gamma p \rightarrow \Sigma^{++}K^+\pi^-\pi^-, \tag{4.25}$$

is shown in Fig. 4.32. The peak at 1.1 GeV can be understood as the Δ^{++} where the K^+ was really a π^+. The same data is shown in Fig. 4.33 where the K^+ was recalculated as a pion and a fit to the peak gives a mass of 1230 ± 10 MeV and a Gaussian width of 120 ± 40 MeV which identify these events as Δ^{++}. There are no other peaks in this figure which may be connected to a Σ^{++}.

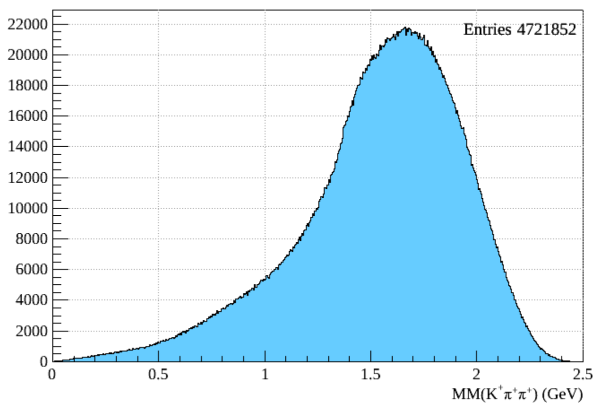

Figure 4.30: Search for Σ^{--}: missing mass off $K^+\pi^+\pi^+$ in the reaction $\gamma p \rightarrow K^+\pi^+\pi^+X^{--}$.

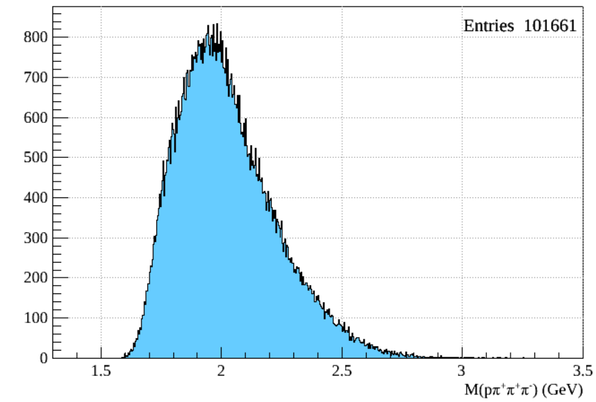

Figure 4.31: Search for Σ^{++}: invariant mass of $\Delta^{++}\overline{K}^0$ reconstructed from the final state particles: $p\pi^+\pi^+\pi^-$, in reaction (4.24).

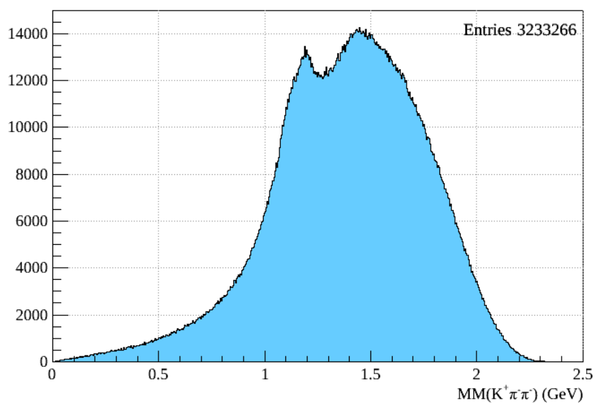

Figure 4.32: Search for Σ^{++}: missing mass off $K^+\pi^-\pi^-$ in reaction (4.25). The peak at 1.2 GeV is due to the Δ^{++} where the K^+ is actually a π^+ as shown in Fig. 4.33.

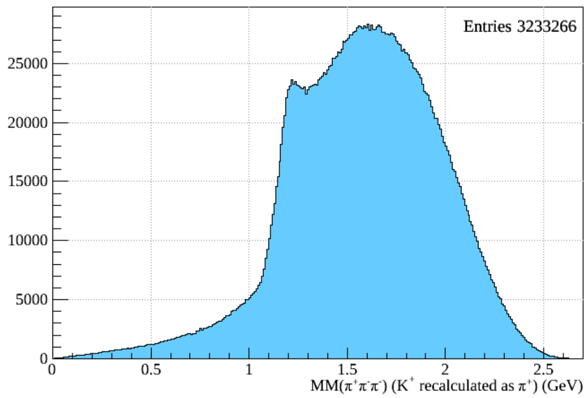

Figure 4.33: Search for Σ^{++}: missing mass off $\pi^+\pi^-\pi^-$ in reaction (4.25) where the K^+ was recalculated as a π^+. The peak at 1.2 GeV is due to the Δ^{++} resonance.

4.5 Summary of Results and Discussion for Future Work

The two sharp spikes in the missing mass off K^+K^+, shown in Fig. 4.35, in the reaction

$$\gamma p \rightarrow K^+K^+X^-, \tag{4.26}$$

are the manifestations of the ground state $\Xi^-(1320)$ and the first excited $\Xi^{*-}(1530)$ state. Figs. 4.34 and 4.36 show the excitation functions for the two lowest mass Ξ^- states. The agreement between the four selections made in the data is well within the systematic error estimated to be at least 12%. The probability of producing the ground state $\Xi^-(1320)$ rises as phase-space increases and levels off approximately 1.7 GeV above threshold. The $\Xi^-(1530)$ state exhibits the same behavior though the statistics and kinematics available in *g12* can not make this a conclusive statement.

The comparison of the $\Xi^-(1320)$ excitation function between the experiments *g12*, *g11* and *g6* (all done with `CLAS`) is shown in Fig. 4.37. In this plot, a correction factor of 50% was applied to the *g6* total cross section as a result of the systematic shift obtained for *g11* by both the `INFN` and `CMU` groups. While the agreement between these experiments is quite good, there is still a systematic error of at least 12%. The study of *g11* by the `CMU` group could be extended to get a better understanding of the overall scaling factors used which would minimize this error. A better test may involve a similar photoproduction experiment using a completely different detector, including different simulation methods and event generators. The newest incarnation of `CLAS` (`CLAS12`) which is currently being built for the 12 GeV beam at `JLAB`, may be a good candidate.

The photoproduction total cross sections for the Ξ states above 1530 MeV are much smaller than anticipated. In this region, there are no narrow peaks

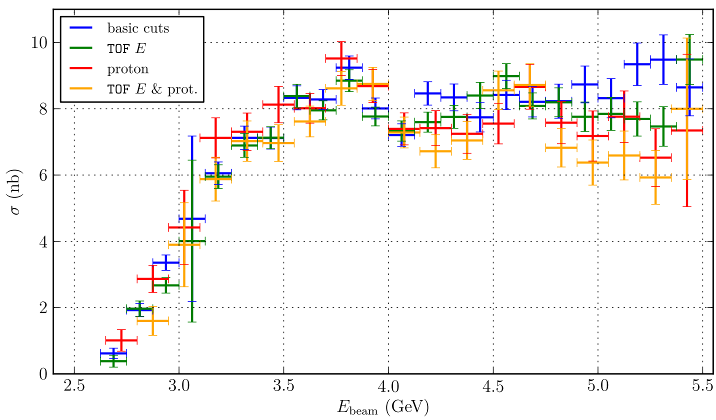

Figure 4.34: Excitation function for $\Xi^-(1320)$.

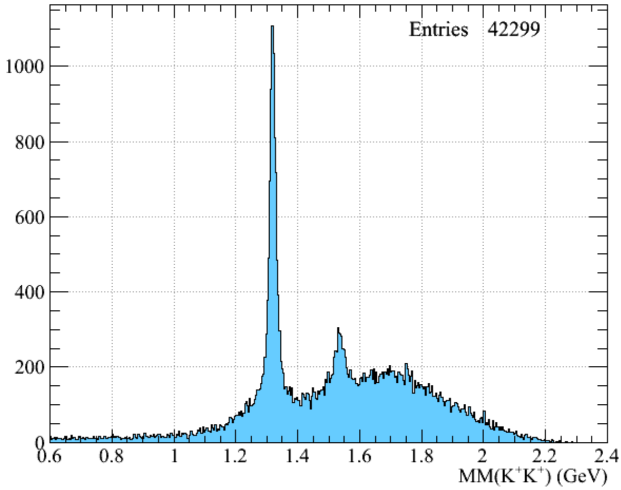

Figure 4.35: Missing mass off K^+K^+ in the reaction $\gamma p \to pK^+K^+X^{--}$. Same as Fig. 3.37 on page 101.

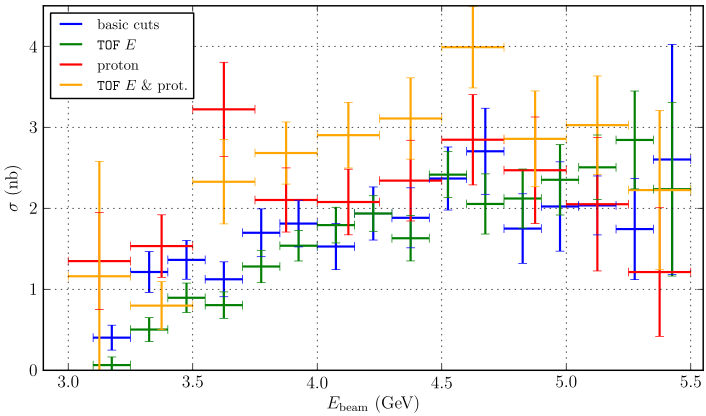

Figure 4.36: Excitation function for $\Xi^-(1530)$.

in the *g12* data. This does not rule out the existance of these states, however, the only prior evidence, seen in Fig. 19 on page 17, is effectively noise above 1530 MeV, and the total cross section of these states is no higher than 2 nb within 2 GeV from threshold. This means the electromagnetic couplings of the massive Ξ states which were seen in hadron-production is small and will require more data and possibly a more sensitive experiment. To gain further insight,

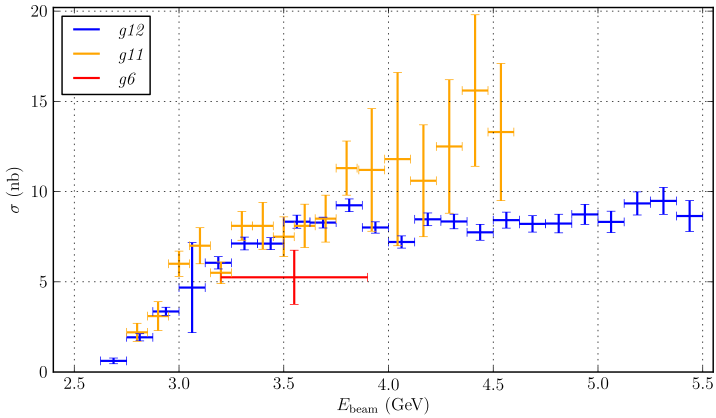

Figure 4.37: Comparison of the $\Xi^-(1320)$ excitation function between the *g12*, *g11* and *g6* experiments done with CLAS.

an order of magnitude more data is required. The CLAS12 detector could be used for this, however it would require finer timing resolution from the TOF to get better separation between pions and kaons at higher momentum.

There are several avenues of investigation that can be done with the *g12* data set. Nakayama et al. calculated the angular distributions of the cascades for pseudovector and pseudoscalar contributions to the production mechanism and found differences involving polarization asymmetries[41]. Measuring this would require a polarized beam or target that can handle a luminosity sufficient to acquire enough statistics. This would also require a simulation model that more accurately describes the data. The $\Xi^0(1315)$ state's differential and total cross section is accessible through the neutral kaon channel, though the background that is brought into the analysis through K^0 identification would need some careful study. The upper limits for the iso-exotics could be mapped out as a function of mass and width since they are unknown quantities in this search. This would be helpful for ascertaining the specific bearing on experimental results that have seen what could be iso-exotic resonances. Finally, the photoproduction of the triply-strange baryon Ω^- can be investigated via missing mass off three K^+'s or through the weak decay to ΛK^-. The photoproduction of Ω^- has never been observed and could open a whole new method for study of these unique states.

Appendix A

List of Abbreviations

a1c The reconstruction program for **CLAS** used on raw and simulated data. (page 60)

ADC Analog to digital converter.

BPM Beam position monitor (page 27).

CAMAC Computer automated measurement and control (page 41).

CC Čerenkov counter (page 35).

CEBAF The Continuous Electron Beam Accelerating Facility (page 20).

CHL Central helium liquefier (page 25)

CLAS The CEBAF Large Acceptance Spectrometer (page 21).

CODA The CEBAF On-line Data Acquisition System (page 41).

DAQ Data acquisition system (page 41).

DC Drift chamber (page 33).

DOE Department of Energy (page 26).

DVCS Deeply virtual Compton scattering (page 29).

EC Electromagnetic calorimeter (page 36).

FEL Free electron laser (page 21).

FPGA Field-programmable gate array: a highly parallel logic control microprocessor (page 41).

g6c The third data set from the *g6* CLAS experiment. This provided the physical basis for the *g12* experiment (page 17).

g12 The `CLAS` experiment on which this work is based (page 24).

`Geant3` `CERN`'s tool for simulating particles traveling through matter. This is the core of the tracking and digitizing program for `CLAS`: `GSIM`. (page 114)

`genr8` The event generator used for the t-channel production of the Ξ resonances in this work.

`GPP` The smearing program for `MC` analyses with `CLAS`. This adds detector efficiency information into the simulations (page 109).

`GSIM` The tracking and digitization program for `MC` with `CLAS` (page 109).

`HyCLAS` The name of the first proposal, of three (see `Super-G`), for the *g12* experiment (page 24).

`JLab` Jefferson Laboratory (page 20), see also `TJNAF`.

`LINAC` Linear accelerator (page 25).

`MC` Monte Carlo. Generally, a simulation based on generating events that are then accepted or cut based on some criteria.

`PMT` Photo-multiplier tube (page 27).

`ST` Start counter (page 32).

`Super-G` The name of the second proposal, of three, for the *g12* experiment (page 24).

`TAG` Photon tagger (page 29).

`TASC` Total absorption shower counter (page 27).

`TDC` Time to digital converter.

`TJNAF` Thomas Jefferson National Accelerator Facility (page 20).

`TOF` Time-of-flight counter (page 38).

Appendix B

TOF Energy Deposit Cut

Listed below is a summary of the time-of-flight energy deposit cuts where p is the momentum of the particle in GeV, and the energy deposit, $\frac{\Delta E}{\Delta x}(\texttt{TOF})$, is in units of MeV/cm. Each cut consists of a linear part applied below a certain momentum and a p^{-2} part above this momentum.

protons:

$p > 0.4$ GeV

$\frac{\Delta E}{\Delta x}(\texttt{TOF}) > 1.45 + \frac{1}{0.4(p-0.07)^2}$ MeV/cm

$\frac{\Delta E}{\Delta x}(\texttt{TOF}) < 2.70 + \frac{1}{0.9(p-0.15)^2}$ MeV/cm

$p \leq 0.4$ GeV

$\frac{\Delta E}{\Delta x}(\texttt{TOF}) > 59p - 14.5$ MeV/cm

$\frac{\Delta E}{\Delta x}(\texttt{TOF}) < 59p - 10.0$ MeV/cm

pions:

$p > 0.08$ GeV

$\frac{\Delta E}{\Delta x}(\texttt{TOF}) > 1.3 + \frac{1}{40(p+0.02)^2}$ MeV/cm

$\frac{\Delta E}{\Delta x}(\texttt{TOF}) < 2.5 + \frac{1}{8(p+0.03)^2}$ MeV/cm

$p \leq 0.08$ GeV

$\frac{\Delta E}{\Delta x}(\texttt{TOF}) > 0$ MeV/cm

kaons:

$p > 0.22$ GeV

$\frac{\Delta E}{\Delta x}(\texttt{TOF}) > 1.5 + \frac{1}{3(p+0.05)^2}$ MeV/cm

$\frac{\Delta E}{\Delta x}(\texttt{TOF}) < 2.6 + \frac{1}{4(p+0.12)^2}$ MeV/cm

$p \leq 0.22$ GeV

$\frac{\Delta E}{\Delta x}(\texttt{TOF}) > 59p - 7$ MeV/cm

$\frac{\Delta E}{\Delta x}(\texttt{TOF}) < 59p$ MeV/cm

Appendix C

Fiducial Cuts

The fiducial cut applied to all tracks in this analysis were done so that only the geometric regions where the MC is reliable were considered. The cuts were based on the charge and the momentum angles, θ and ϕ, for each track in the lab-frame. The azimuthal angle (ϕ) is the absolute value from the mid-plane of each CLAS sector. The shape of the cut, shown in Fig. C.1, consists of a minimum polar angle θ_0, a parabolic curve in (ϕ, θ) and a maximum azimuthal angle from the sector mid-plane $|\phi_1|$. The parabolic curve starts at (ϕ_0, θ_0) and ends at (ϕ_1, θ_1) as shown in the diagram. In this analysis, the values used were the following. For all particles:

$$\phi_0 = 0.29 \text{ radians}, \tag{C.1}$$

$$\phi_1 = 0.44 \text{ radians}, \tag{C.2}$$

$$\theta_1 = 1.0 \text{ radians}. \tag{C.3}$$

For negatively charged particles:

$$\theta_0 = 0.3 \text{ radians}, \tag{C.4}$$

while for positively charged particles in sectors 2–6:

$$\theta_0 = 0.11 \text{ radians}. \tag{C.5}$$

For positively charged particles in sector 1:

$$\theta_0 = 0.15 \text{ radians} \tag{C.6}$$

and finally, for positively charged particles in sector 2:

$$\theta_0 = 0.13 \text{ radians}. \tag{C.7}$$

This cut can be seen specifically for K^+ tracks in Fig. 4.7 on page 111.

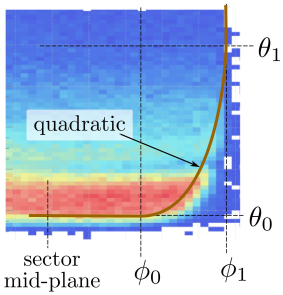

Figure C.1: Diagram of fiducial cut. This is done for each sector and is symmetric about the mid-plane.

Appendix D

Tabular Data

This section contains the numeric data shown in the plots concerning excitation functions and upper limit calculations in Chapter 4. All tables in this section present data as a function of the beam energy. The E_{beam} column gives the center of the bin and the full bin width (ΔE_{beam}) is shown at the top of each table.

D.1 Excitation Functions

The following tables contain numeric values for the plots shown in Chapter 4 leading to the excitation functions of the $\Xi^-(1320)$ and $\Xi^-(1530)$.

Table D.1: Photoproduction excitation function data for the $\Xi^-(1320)$ with "basic cuts" only which are listed in Tables 3.2 and 3.3. This is the data shown in Figs. 3.31, 4.4, 4.6 and 4.16.

$\Xi^-(1320)$, basic cuts only $\Delta E_{\text{beam}} = 125$ MeV							
E_{beam} (GeV)	F (10^{12})	N	δN	A (%)	δA	σ (nb)	$\delta\sigma$
2.6875	1.808	27	7	2.00	0.059	0.62	0.16
2.8125	1.767	117	12	2.83	0.060	1.92	0.20
2.9375	1.775	260	17	3.58	0.061	3.36	0.23
3.0625	1.333	9	5	0.11	0.010	4.68	2.50
3.1875	1.261	452	25	4.86	0.061	6.05	0.34
3.3125	1.329	612	30	5.31	0.060	7.12	0.35
3.4375	1.416	717	33	5.84	0.059	7.12	0.33
3.5625	1.424	919	39	6.36	0.059	8.33	0.36
3.6875	2.034	1350	47	6.58	0.059	8.28	0.30
3.8125	1.720	1324	49	6.84	0.058	9.24	0.35
3.9375	2.123	1436	55	6.93	0.056	8.01	0.31
4.0625	1.769	1109	52	7.14	0.056	7.21	0.34
4.1875	1.919	1401	57	7.08	0.055	8.46	0.35
4.3125	1.679	1191	57	6.98	0.054	8.34	0.40
4.4375	1.499	935	53	6.62	0.052	7.74	0.44
4.5625	1.833	1260	66	6.70	0.051	8.42	0.44
4.6875	1.720	1114	61	6.47	0.050	8.21	0.46
4.8125	1.553	996	62	6.40	0.049	8.23	0.51
4.9375	1.670	1070	68	6.02	0.047	8.73	0.56
5.0625	1.644	959	68	5.75	0.046	8.32	0.59
5.1875	1.670	1036	71	5.45	0.044	9.34	0.64
5.3125	1.441	870	68	5.23	0.043	9.48	0.75
5.4375	1.061	557	55	4.99	0.043	8.65	0.86

Table D.2: Photoproduction excitation function data for the $\Xi^-(1320)$ with the cuts listed in Tables 3.2 and 3.3 as well as the time-of-flight energy deposit cut as discussed in Sec. 3.5. This is the data shown in Figs. 3.31, 4.4, 4.6 and 4.16.

$\Xi^-(1320)$, basic and E_{TOF} cuts $\Delta E_{\mathrm{beam}} = 125$ MeV							
E_{beam} (GeV)	F (10^{12})	N	δN	A (%)	δA	σ (nb)	$\delta\sigma$
2.6875	1.808	12	5	1.38	0.050	0.38	0.18
2.8125	1.767	81	9	1.91	0.050	1.97	0.23
2.9375	1.775	145	12	2.51	0.052	2.67	0.23
3.0625	1.333	5	3	0.08	0.008	4.01	2.44
3.1875	1.261	313	18	3.43	0.051	5.95	0.36
3.3125	1.329	419	21	3.76	0.051	6.89	0.36
3.4375	1.416	516	23	4.20	0.051	7.13	0.33
3.5625	1.424	658	27	4.53	0.051	8.38	0.36
3.6875	2.034	917	32	4.65	0.050	7.95	0.29
3.8125	1.720	896	32	4.83	0.049	8.85	0.33
3.9375	2.123	983	35	4.89	0.048	7.77	0.28
4.0625	1.769	796	32	5.04	0.048	7.33	0.31
4.1875	1.919	883	34	4.97	0.047	7.60	0.30
4.3125	1.679	775	34	4.89	0.045	7.76	0.35
4.4375	1.499	711	33	4.63	0.044	8.40	0.39
4.5625	1.833	936	38	4.67	0.043	8.99	0.38
4.6875	1.720	759	36	4.48	0.042	8.09	0.39
4.8125	1.553	683	36	4.41	0.041	8.20	0.44
4.9375	1.670	649	37	4.11	0.039	7.76	0.44
5.0625	1.644	620	39	3.94	0.038	7.85	0.50
5.1875	1.670	579	38	3.70	0.037	7.69	0.52
5.3125	1.441	468	37	3.57	0.036	7.47	0.60
5.4375	1.061	417	33	3.40	0.036	9.49	0.75

Table D.3: Photoproduction excitation function data for the $\Xi^-(1320)$ with the cuts listed in Tables 3.2 and 3.3, requiring a proton in the event. This is the data shown in Figs. 3.31, 4.4, 4.6 and 4.16.

$\Xi^-(1320)$, basic cuts, requiring a proton $\Delta E_{\text{beam}} = 150$ MeV							
E_{beam} (GeV)	F (10^{12})	N	δN	A (%)	δA	σ (nb)	$\delta\sigma$
2.775	2.180	14	5	0.58	0.028	1.01	0.33
2.925	2.090	59	8	0.89	0.030	2.87	0.41
3.075	1.562	28	7	0.36	0.017	4.42	1.12
3.225	1.593	163	13	1.29	0.029	7.12	0.61
3.375	1.610	222	17	1.69	0.031	7.31	0.57
3.525	1.737	293	19	1.86	0.031	8.13	0.55
3.675	2.435	457	25	2.09	0.031	8.02	0.45
3.825	2.175	507	26	2.19	0.031	9.52	0.51
3.975	2.363	525	29	2.29	0.030	8.68	0.50
4.125	2.244	439	28	2.37	0.030	7.39	0.48
4.275	2.173	411	29	2.29	0.029	7.42	0.53
4.425	1.754	322	26	2.27	0.028	7.25	0.59
4.575	2.156	400	32	2.20	0.028	7.55	0.61
4.725	1.900	397	31	2.16	0.027	8.66	0.67
4.875	2.130	383	32	2.12	0.026	7.58	0.63
5.025	1.915	304	32	1.98	0.025	7.18	0.76
5.175	1.990	321	32	1.86	0.024	7.76	0.78
5.325	1.815	230	31	1.74	0.023	6.52	0.87
5.475	0.686	94	29	1.66	0.023	7.35	2.30

Table D.4: Photoproduction excitation function data for the $\Xi^-(1320)$ with the cuts listed in Tables 3.2 and 3.3, requiring a proton in the event, and the time-of-flight energy deposit cut as discussed in Sec. 3.5. This is the data shown in Figs. 3.31, 4.4, 4.6 and 4.16.

$\Xi^-(1320)$, basic and E_{TOF} cuts, requiring a proton $\Delta E_{\mathrm{beam}} = 150$ MeV							
E_{beam} (GeV)	F (10^{12})	N	δN	A (%)	δA	σ (nb)	$\delta\sigma$
2.775	2.180	14	5	0.58	0.028	1.01	0.33
2.925	2.090	59	8	0.89	0.030	2.87	0.41
3.075	1.562	28	7	0.36	0.017	4.42	1.12
3.225	1.593	163	13	1.29	0.029	7.12	0.61
3.375	1.610	222	17	1.69	0.031	7.31	0.57
3.525	1.737	293	19	1.86	0.031	8.13	0.55
3.675	2.435	457	25	2.09	0.031	8.02	0.45
3.825	2.175	507	26	2.19	0.031	9.52	0.51
3.975	2.363	525	29	2.29	0.030	8.68	0.50
4.125	2.244	439	28	2.37	0.030	7.39	0.48
4.275	2.173	411	29	2.29	0.029	7.42	0.53
4.425	1.754	322	26	2.27	0.028	7.25	0.59
4.575	2.156	400	32	2.20	0.028	7.55	0.61
4.725	1.900	397	31	2.16	0.027	8.66	0.67
4.875	2.130	383	32	2.12	0.026	7.58	0.63
5.025	1.915	304	32	1.98	0.025	7.18	0.76
5.175	1.990	321	32	1.86	0.024	7.76	0.78
5.325	1.815	230	31	1.74	0.023	6.52	0.87
5.475	0.686	94	29	1.66	0.023	7.35	2.30

Table D.5: Photoproduction excitation function data for the $\Xi^-(1530)$ with "basic cuts" only which are listed in Tables 3.2 and 3.3. This is the data shown in Figs. 3.31, 4.17, 4.20 and 4.21.

$\Xi^-(1530)$, basic cuts only $\Delta E_{\text{beam}} = 150$ MeV							
E_{beam} (GeV)	F (10^{12})	N	δN	A (%)	δA	σ (nb)	$\delta\sigma$
3.225	1.593	12	5	1.56	0.069	0.40	0.15
3.375	1.610	67	14	2.80	0.074	1.21	0.25
3.525	1.737	107	19	3.70	0.073	1.36	0.24
3.675	2.435	138	26	4.15	0.068	1.12	0.22
3.825	2.175	217	38	4.82	0.068	1.70	0.30
3.975	2.363	294	47	5.65	0.068	1.81	0.29
4.125	2.244	238	44	5.70	0.065	1.53	0.29
4.275	2.173	307	52	6.00	0.064	1.94	0.33
4.425	1.754	250	49	6.21	0.062	1.88	0.37
4.575	2.156	379	62	6.10	0.060	2.37	0.39
4.725	1.900	385	76	6.15	0.058	2.70	0.53
4.875	2.130	266	65	5.85	0.056	1.75	0.43
5.025	1.915	273	74	5.79	0.055	2.02	0.55
5.175	1.990	277	49	5.62	0.053	2.04	0.36
5.325	1.815	205	73	5.32	0.051	1.74	0.62
5.475	0.686	111	61	5.10	0.049	2.60	1.42

Table D.6: Photoproduction excitation function data for the $\Xi^-(1530)$ with the cuts listed in Tables 3.2 and 3.3 as well as the time-of-flight energy deposit cut as discussed in Sec. 3.5. This is the data shown in Figs. 3.31, 4.17, 4.20 and 4.21.

$\Xi^-(1530)$, basic and E_{TOF} cuts $\Delta E_{\mathrm{beam}} = 150$ MeV							
E_{beam} (GeV)	F (10^{12})	N	δN	A (%)	δA	σ (nb)	$\delta\sigma$
3.225	1.593	1	2	1.04	0.057	0.06	0.10
3.375	1.610	19	6	1.95	0.062	0.50	0.15
3.525	1.737	50	10	2.66	0.062	0.90	0.18
3.675	2.435	71	14	2.97	0.058	0.80	0.16
3.825	2.175	117	18	3.45	0.058	1.28	0.20
3.975	2.363	176	21	3.97	0.058	1.54	0.19
4.125	2.244	195	24	3.98	0.055	1.79	0.22
4.275	2.173	218	25	4.25	0.054	1.94	0.22
4.425	1.754	154	26	4.43	0.053	1.63	0.28
4.575	2.156	274	32	4.32	0.051	2.42	0.28
4.725	1.900	205	37	4.31	0.049	2.05	0.37
4.875	2.130	225	39	4.10	0.047	2.12	0.36
5.025	1.915	223	41	4.07	0.046	2.35	0.43
5.175	1.990	238	38	3.92	0.044	2.51	0.40
5.325	1.815	231	49	3.67	0.042	2.84	0.60
5.475	0.686	64	31	3.44	0.041	2.24	1.07

Table D.7: Photoproduction excitation function data for the $\Xi^-(1530)$ with the cuts listed in Tables 3.2 and 3.3, requiring a proton in the event. This is the data shown in Figs. 3.31, 4.17, 4.20 and 4.21.

$\Xi^-(1530)$, basic cuts, requiring a proton $\Delta E_{\mathrm{beam}} = 250$ MeV							
E_{beam} (GeV)	F (10^{12})	N	δN	A (%)	δA	σ (nb)	$\delta\sigma$
3.125	2.595	8	3	0.19	0.021	1.35	0.60
3.375	2.745	35	9	0.75	0.028	1.53	0.39
3.625	2.746	111	20	1.12	0.028	3.22	0.58
3.875	3.842	133	25	1.47	0.028	2.10	0.40
4.125	3.689	143	28	1.67	0.027	2.08	0.40
4.375	3.178	150	32	1.80	0.027	2.34	0.50
4.625	3.553	203	40	1.80	0.025	2.85	0.56
4.875	3.223	155	41	1.74	0.024	2.47	0.66
5.125	3.314	130	52	1.71	0.023	2.05	0.82
5.375	2.501	56	37	1.65	0.023	1.21	0.79

Table D.8: Photoproduction excitation function data for the $\Xi^-(1530)$ with the cuts listed in Tables 3.2 and 3.3, requiring a proton in the event, and the time-of-flight energy deposit cut as discussed in Sec. 3.5. This is the data shown in Figs. 3.31, 4.17, 4.20 and 4.21.

$\Xi^-(1530)$, basic and E_{TOF} cuts, requiring a proton $\Delta E_{\mathrm{beam}} = 250$ MeV							
E_{beam} (GeV)	F (10^{12})	N	δN	A (%)	δA	σ (nb)	$\delta\sigma$
3.125	2.595	4	5	0.12	0.016	1.16	1.42
3.375	2.745	13	5	0.54	0.024	0.80	0.30
3.625	2.746	57	13	0.80	0.024	2.33	0.52
3.875	3.842	121	17	1.05	0.024	2.68	0.38
4.125	3.689	141	20	1.18	0.023	2.90	0.41
4.375	3.178	140	23	1.27	0.022	3.11	0.50
4.625	3.553	202	25	1.27	0.021	3.99	0.50
4.875	3.223	127	26	1.23	0.020	2.86	0.59
5.125	3.314	134	27	1.20	0.019	3.03	0.61
5.375	2.501	70	31	1.13	0.019	2.22	0.98

D.2 Higher Mass Ξ Upper Limits

The following tables contain numeric values for the plots shown in Sec. 4.3 leading to the upper limit calculations for Ξ^{*-} candidate states at 1620, 1690 and 1820 MeV.

Table D.9: Excitation function data of the $\Xi^-(1620)$ as shown in Figs 4.22, 4.24 and 4.25. The last two columns show the upper limit of the total cross section with and with the scaling factor of 35% which is discussed in Sec.4.1.4 on page 113.

$\Xi^-(1620)$ Upper Limit, CL$=90\%$ $\Delta E_{\text{beam}} = 250$ MeV					
E_{beam} (GeV)	F (10^{12})	$< N$	A (%)	no scaling $< \sigma$ (pb)	35% s.f. $< \sigma$ (pb)
3.625	2.746	17.4	0.597	409	629
3.875	3.842	15.0	0.851	272	418
4.125	3.689	17.9	1.03	277	426
4.375	3.178	36.3	1.22	556	855
4.625	3.553	24.0	1.28	313	482
4.875	3.223	31.1	1.28	447	688
5.125	3.314	27.0	1.26	380	585
5.375	2.501	32.1	1.30	584	899
average (with scaling factor): $\sigma < 623$ pb					

Table D.10: Excitation function data of the $\Xi^-(1690)$ as shown in Figs 4.22, 4.24 and 4.25. The last two columns show the upper limit of the total cross section with and with the scaling factor of 35% which is discussed in Sec.4.1.4 on page 113.

$\Xi^-(1690)$ Upper Limit, CL$=90\%$ $\Delta E_{\text{beam}} = 250$ MeV					
E_{beam} (GeV)	F (10^{12})	$< N$	A (%)	no scaling $< \sigma$ (pb)	35% s.f. $< \sigma$ (nb)
3.875	3.842	33.2	0.653	782	1.20
4.125	3.689	34.8	0.903	618	0.951
4.375	3.178	27.0	1.12	449	0.691
4.625	3.553	42.9	1.21	590	0.908
4.875	3.223	32.5	1.31	454	0.699
5.125	3.314	63.7	1.37	830	1.28
5.375	2.501	43.1	1.35	756	1.16
average (with scaling factor): $\sigma < 1.00$ nb					

Table D.11: Excitation function data of the $\Xi^-(1820)$ as shown in Figs 4.22, 4.24 and 4.25. The last two columns show the upper limit of the total cross section with and with the scaling factor of 35% which is discussed in Sec.4.1.4 on page 113.

$\Xi^-(1820)$ Upper Limit, CL= 90% $\Delta E_{\text{beam}} = 250$ MeV					
				no scaling	35% s.f.
E_{beam} (GeV)	F (10^{12})	$< N$	A (%)	$< \sigma$ (pb)	$< \sigma$ (nb)
4.125	3.689	12.9	0.690	300	0.462
4.375	3.178	37.9	0.830	850	1.31
4.625	3.553	39.1	0.987	659	1.01
4.875	3.223	36.6	1.13	596	0.916
5.125	3.314	49.7	1.20	740	1.14
5.375	2.501	43.9	1.32	786	1.21
average (with scaling factor): $\sigma < 1.01$ nb					

D.3 K^+_{fast} t-slope and Missing Mass Trends

The following tables contain numeric values for the plots shown in Sec. 4.1.4 concerning the trends of the input parameters for the simulations that are observed in the data.

Table D.12: t-slope and missing mass off K^+_{fast} parameters as a function of beam energy for the $\Xi^-(1320)$ state. This data corresponds to Figs. 4.11, 4.12 and 4.13

$\Xi^-(1320)$ $\Delta E_{\text{beam}} = 233$ MeV						
E_{beam} (GeV)	t-slope	err	MM(K^+_{fast}) mean (GeV)	err	MM(K^+_{fast}) width (MeV)	err
2.749	6.03	0.82	–	–	–	–
2.981	5.67	0.51	1.9217	0.0022	42.7	1.6
3.214	3.88	0.13	1.9472	0.0043	74.8	3.0
3.446	3.449	0.084	1.9829	0.0028	83.1	2.4
3.679	2.944	0.048	2.0069	0.0028	107	2.2
3.911	2.555	0.044	2.0290	0.0036	130	2.5
4.144	1.837	0.035	2.0343	0.0052	160	4.2
4.376	1.540	0.038	2.0601	0.0067	189	5.3
4.609	1.725	0.052	2.0766	0.0054	188	4.2
4.841	1.579	0.054	2.0854	0.0063	198	3.9
5.074	1.783	0.055	2.1250	0.0075	224	5.1
5.306	1.595	0.070	2.1415	0.0069	210	6.1

Table D.13: t-slope of the K^+_{fast} as a function of beam energy for the $\Xi^-(1530)$ state. This data corresponds to Fig. 4.11.

$\Xi^-(1530)$ $\Delta E_{\text{beam}} = 388$ MeV		
E_{beam}	t-slope	err
3.369	2.70	0.32
3.756	2.56	0.16
4.144	1.87	0.15
4.531	2.48	0.10
4.919	1.89	0.13
5.306	1.39	0.12

Table D.14: Parameters from the missing mass off the K^+_{fast} as a function of beam energy for the $\Xi^-(1530)$ state. This data corresponds to Figs. 4.12 and 4.13.

$\Xi^-(1530)$ $\Delta E_{\text{beam}} = 467$ MeV				
E_{beam} (GeV)	$\text{MM}(K^+_{\text{fast}})$ mean (GeV)	err	$\text{MM}(K^+_{\text{fast}})$ width (MeV)	err
3.100	2.1005	0.019	19.4	62
3.567	2.1255	0.0024	54.0	1.6
4.033	2.1817	0.0030	83.9	2.0
4.500	2.2158	0.0029	98.9	1.9
4.967	2.2538	0.0039	119	2.4

Bibliography

[1] E. Rutherford. The scattering of α and β particles by matter and the structure of the atom. *Phil. Mag.*, 21:669–688, may 1911.

[2] J. Chadwick. Possible existence of a neutron. *Nature*, page 312, feb 1932.

[3] I. Estermann, O. C. Simpson, and O. Stern. The magnetic moment of the proton. *Phys. Rev.*, 52(6):535–545, Sep 1937.

[4] V. E. Barnes et al. Observation of a hyperon with strangeness number three. *Phys. Rev. Lett.*, 12(8):204, 1964.

[5] D. DeCamp et al. Determination of the number of light neutrino species. *Physics Letters B*, 231(4):519 – 529, 1989.

[6] Alain Blondel. The number of neutrinos and the Z line shape. *Comptes Rendus Physique*, 3(9):1155 – 1164, 2002.

[7] S. Hassani. *Mathematical Physics.* Springer-Verlag, New York, 2000.

[8] C. Amsler et al. The review of particle physics. *Phys. Lett.*, B667(1), 2008. (Particle Data Group) 2009 partial update for the 2010 edition.

[9] Simon Capstick and Nathan Isgur. Baryons in a relativized quark model with chromodynamics. *Phys. Rev. D*, 34(9):2809–2835, Nov 1986.

[10] Kuang-Ta Chao, Nathan Isgur, and Gabriel Karl. Strangeness −2 and −3 baryons in a quark model with chromodynamics. *Phys. Rev. D*, 23(1):155–162, Jan 1981.

[11] L.Ỹa. Glozman and D.Õ. Riska. The spectrum of the nucleons and the strange hyperons and chiral dynamics. *Phys. Rep.*, (268):263–303, 1996.

[12] R. Bijker, F. Iachello, and A. Leviatan. Algebraic models of hadron structure: Ii. strange baryons. *Annals of Physics*, 284(1):89 – 133, 2000.

[13] S. Capstick and W. Roberts. Quark models of baryon masses and decays. *Progress in Particle and Nuclear Physics*, 45(Supplement 2):S241 – S331, 2000.

[14] R. T. Ross, T. Buran, J. L. Lloyd, J. H. Mulvey, and D. Radojicic. Xi pi resonance with mass 1606 MeV/c-squared. *Phys. Lett.*, B38:177–180, 1972.

[15] E. Briefel et al. Search for Xi* Production in K- p Interactions at 2.87-GeV/*c*. *Phys. Rev.*, D16:2706, 1977.

[16] S. F. Biagi et al. Production of hyperons and hyperon resonances in Xi- N interactions at 102-GeV/c and 135-GeV/*c*. *Zeit. Phys.*, C9:305, 1981.

[17] C. Dionisi et al. An enhancement at the Sigma anti-K threshold 1680-MeV observed in K- p reactions at 4.2-GeV/*c*. *Phys. Lett.*, B80:145, 1978.

[18] S. F. Biagi et al. Xi* resonances in Xi- be interactions. 1. diffractive production in the Lambda K- and Xi- pi+ pi- channels. *Z. Phys.*, C34:15, 1987.

[19] M. I. Adamovich et al. First observation of the Xi- pi+ decay mode of the Xi0(1690) hyperon. *Eur. Phys. J.*, C5:621–624, 1998.

[20] B. Aubert et al. Measurement of the spin of the $\Xi(1530)$ resonance. *Phys. Rev. D*, 78(3):034008, Aug 2008.

[21] B. A. Mecking et al. The `CEBAF` Large Acceptance Spectrometer (`CLAS`). *Nucl. Instr. and Meth. A*, 503:513, 2003.

[22] Christoph Leemann, David Douglas, and Geoffrey Krafft. The Continuous Electron Beam Accelerator Facility: `CEBAF` at the Jefferson Laboratory. *Annu. Rev. Nucl. Part. Sci.*, 51:413–450, 2001.

[23] Jefferson lab picture exchange. http://www.jlab.org. website.

[24] P. Eugenio et al. Search for new forms of hadronic matter in photoproduction. Technical report, `CLAS` Analysis Proposal `PR04-005`, 2003.

[25] D. Weygand et al. Study of pentaquark states in photoproduction off protons. Technical report, `CLAS` Analysis Proposal `PR04-017`, 2004.

[26] W. Chen et al. The $\gamma p \to \pi^+ n$ single charged pion photoproduction. Technical report, `CLAS` Analysis Proposal `PR08-003`, 2008.

[27] Allison Lung. Jefferson Lab starts its 12 GeV physics upgrade. *CERN Courier*, 49:15–18, 2009.

[28] Sober D. I. et al. The bremsstrahlung tagged photon beam in Hall `B` at JLab. *Nucl. Instr. and Meth. A*, 440:263–284, 2000.

[29] J. Li. The new tagger calibration program. JLab, March 2003.

[30] Bosted P. Burkert V. D. Elouadrhiri L. Avakian, H. et al. Measurement of single and double spin asymmetries in deep inelastic pion electroproduction with a longitudinally polarized target. *Phys. Rev. Lett.*, 2010. submitted.

[31] Y. G. Sharabian et al. A new highly segmented start counter for the `CLAS` detector. *Nucl. Instr. and Meth. A*, 556:246–258, 2006.

[32] Bryan M^{c}Kinnon. *Search for the* Θ^+ *Pentaquark in the Reaction* $\gamma d \rightarrow pK^+K^-n$ *with `CLAS`*. PhD thesis, University of Glasgow, 2006.

[33] M. Mestayer et al. The clas drift chamber system. *Nucl. Instr. and Meth. A*, 449:81–111, 2000.

[34] M. Amarian et al. The CLAS forward electromagnetic calorimeter. *Nucl. Instr. and Meth. A*, 460, 2001.

[35] E. S. Smith et al. The time-of-flight system for `CLAS`. *Nucl. Instr. and Meth. A*, 432:265–298, 1999.

[36] V. Kubarovsky and B. Raydo. personal correspondance.

[37] Mike Williams. *Measurement of Differential Cross Sections and Spin Density Matrix Elements along with a Partial Wave Analysis for* $\gamma p \rightarrow p\omega$ *using `CLAS` at Jefferson Lab*. PhD thesis, Carnegie Mellon University, 2007.

[38] David Lawrence and Mac Mestayer. `CLAS` Drift Chamber Calibration: Software and Procedures. CLAS-NOTE 1999-018, 1999.

[39] H. Egiyan et al. `CLAS` Analysis Note 2009-104, in process for publication.

[40] K. Nakayama, Yongseok Oh, and H. Haberzettl. Photoproduction of Ξ off nucleons. *Phys. Rev. C*, page 035205, 2006.

[41] K. Nakayama, Yongseok Oh, and H. Haberzettl. Cascade baryon production in photon-induced reactions. *J. Phys.: Conf. Ser.*, page 012023, 2007.

[42] K. Abe et al. Inclusive photoproduction of strange baryons at 20 GeV. *Phys. Rev. D*, 32(11):2869, 1985.

[43] D. Aston et al. A study of inclusive photoproduction of hyperons and antihyperons in the range of 20 to 70 GeV. *Nucl. Phys. B*, 198:189–208, 1982.

[44] J. T. Goetz et al. Using controlled magnetic perturbations to study the plasma confinement in a spheromak. *Bull. Am. Phys. Soc.*, 48:150, 2003. Poster at APS meeting.

[45] J. W. Price et al. Exclusive photoproduction of the cascade (Ξ) hyperons. *Phys. Rev. C*, 71:058201, 2005.

[46] L. Morand, M. Garçon, et al. Deeply virtual and exclusive electroproduction of ω mesons. *Eur. Phys. J. A*, 24:445, 2005.

[47] K. Joo, L. C. Smith, et al. Measurement of the polarized structure function $\sigma_{LT'}$ for pion electroproduction in the roper resonance region. *Phys. Rev. C*, 72:058202, 2005.

[48] M. Osipenko et al. Measurement of the deuteron structure function F_2 in the resonance region and evaluation of its moments. *Phys. Rev. C*, 73:045205, 2006.

[49] S. Strauch et al. Beam-helicity asymmetries in double-charged-pion photoproduction on the proton. *Phys. Rev. Lett.*, 95:162003, 2006.

[50] A. Klimenko, S. Kuhn, et al. Electron electron scattering from high-momentum neutrons in deuterium. *Phys. Rev. C*, 73:035212, 2006.

[51] K. Egiyan et al. Measurement of 2- and 3-nucleon short range correlation probabilities in nuclei. *Phys. Rev. Lett.*, 96:082501, 2006.

[52] M. Battaglieri, R. De Vita, V. Kubarovsky, et al. Search for $\Theta^+(1540)$ pentaquark in high statistics measurement of $\gamma p \rightarrow \overline{K}^0 K^+ n$ at clas. *Phys. Rev. Lett.*, 96:042001, 2006.

[53] M. Dugger, B. Ritchie, et al. η' photoproduction on the proton for photon energies from 1.527 to 2.227 GeV. *Phys. Rev. Lett.*, 96:062001, 2006.

[54] R. Bradford, R. Schumacher, et al. Differential cross sections for γ p $\rightarrow K^+$ Y for Λ and Σ^0 hyperons. *Phys. Rev. C*, 73:035202, 2006.

[55] H. Egiyan, V. Burkert, et al. Single π^+ electroproduction on the proton in the first and second resonance regions at 0.25 $GeV^2 < Q^2 <$ 0.65 GeV^2 using `CLAS`. *Phys. Rev. C*, 73:025204, 2006.

[56] B. McKinnon, K. Hicks, et al. Search for the Θ^+ pentaquark in the reaction $\gamma d \rightarrow pK^-K^+n$. *Pys. Rev. Lett.*, 96:212001, 2006.

[57] S. Niccolai, M. Mirazita, P. Rossi, et al. Search for the Θ^+ pentaquark in the $\gamma d \rightarrow \Lambda n K^+$ reaction measured with CLAS. *Pys. Rev. Lett.*, 97:032001, 2006.

[58] V. Kubarovsky, P. Stoler, et al. Search for Θ^{++} pentaquarks in the exclusive reaction $\gamma p \rightarrow K^+K^-p$. *Pys. Rev. Lett.*, 97:102001, 2006.

[59] S. Chen, H. Avakian, V. Burkert, P. Eugenio, et al. Measurement of deeply virtual compton scattering with a polarized proton target. *Phys. Rev. Lett.*, 97:072002, 2006.

[60] K. V. Dharmawardane, P. Bosted, S. E. Kuhn, Y. Prok, et al. Measurement of the x- and Q^2-dependence of the spin asymmetry A1 of the nucleon. *Phys. Lett. B*, 641:11, 2006.

[61] M. Ungaro, P. Stoler, et al. Measurement of the N to $\Delta(1232)$ transition at high momentum transfer by π^0 electroproduction. *Phys. Rev. Lett.*, 97:112003, 2006.

[62] R. De Vita, M. Battaglieri, V. Kubarovski, et al. Search for the Θ^+ pentaquark in the reactions $\gamma p \to \overline{K}^0 K^+ n$ and $\gamma p \to \overline{K}^0 K^0 p$. *Phys. Rev. D*, 74:032001, 2006.

[63] P. E. Bosted, K. V. Dharmawardane, G. E. Dodge, T. A. Forest, S. E. Kuhn, Y. Prok, et al. Quark-hadron duality in spin structure functions g1p and g1d. *Phys. Rev. C*, 75:035203, 2007.

[64] P. Ambrozewicz, D. S. Carman, R. Feuerbach, M. D. Mestayer, B. A. Raue, R. Schumacher, A. Tkabladze, et al. Separated structure functions for the exclusive electroproduction of $K^+\Lambda$ and $K^+\Sigma^0$ final states. *Phys. Rev. C*, 75:045203, 2007.

[65] R. Bradford, R. Schumacher, et al. First measurement of beam-recoil observables C_X and C_Z in hyperon photoproduction. *Phys. Rev. C*, 75:035205, 2007.

[66] K. Sh. Egiyan, G. A. Asryan, N. B. Dashyan, N. G. Gevorgyan, J.-M. Laget, K. Griffioen, S. Kuhn, et al. Study of exclusive d(e,e'p)n reaction mechanism at high Q^2. *Phys. Rev. Lett.*, 98:262502, 2007.

[67] I. Hleiqawi, K. Hicks, D. Carman, T. Mibe, G. Niculescu, A. Tkabladze, et al. Cross sections for the $\gamma p \to K^{*\circ}\Sigma^+$ reaction at $E(\gamma) = 1.7 - 3.0$ GeV. *Phys. Rev. C*, 75:042201, 2007.

[68] L. Guo, D. P. Weygand, M. Battaglieri, R. De Vita, V. Kubarov sky, P. Stoler, et al. Cascade production in the reaction $\gamma p \to K^+K^+X$ and $\gamma p \to K^+K^+\pi^-X$. *Phys. Rev. C*, 76:025208, 2007.

[69] H. Denizli, S. Dytman, J. Mueller, et al. Q^2 dependence of the $S_{11}(1535)$ photocoupling and evidence for a P-wave resonance in η electroproduction. *Phys. Rev. C*, 76:015204, 2007.

[70] K. Park et al. Cross sections and beam asymmetries for $\vec{e}p \to en\pi^+$ in the nucleon resonance region for $1.7 \leq q^2 \leq 4.5(\mathrm{GeV})^2$.

[71] D. G. Ireland et al. Bayesian analysis of pentaquark signals from CLAS data. *Phys. Rev. Lett.*, 100(5):052001, Feb 2008.

[72] A. S. Biselli et al. First measurement of target and double spin asymmetries for $\vec{e}\vec{p} \to ep\pi^0$ in the nucleon resonance region above the $\Delta(1232)$. *Phys. Rev. C*, 78(4):045204, Oct 2008.

[73] I. G. Aznauryan et al. Electroexcitation of the roper resonance for $1.7 < q^2 < 4.5$ GeV^2 in $\vec{e}p \to en\pi^+$. *Phys. Rev. C*, 78(4):045209, Oct 2008.

[74] J. P. Santoro et al. Electroproduction of $\varphi(1020)$ mesons at $1.4 \leq q^2 \leq 3.8$ GeV^2 measured with the CLAS spectrometer. *Phys. Rev. C*, 78:025210, Aug 2008.

[75] M. H. Wood et al. Light vector mesons in the nuclear medium. *Phys. Rev. C*, 78(1):015201, Jul 2008.

[76] R. Nasseripour et al. Polarized structure function $\sigma_{LT'}$ for ^{1}He$\acute{e}$K$^+\Lambda$ in the nucleon resonance region. *Phys. Rev. C*, 77(6):065208, Jun 2008.

[77] P. E. Bosted et al. Ratios of ^{15}N/^{12}C and ^{4}He/^{12}C inclusive electroproduction cross sections in the nucleon resonance region. *Phys. Rev. C*, 78(1):015202, Jul 2008.

[78] R. De Masi et al. Measurement of ep $\rightarrow$ epπ^0 beam spin asymmetries above the resonance region. *Phys. Rev. C*, 77(4):042201, Apr 2008.

[79] F. X. Girod et al. Measurement of deeply virtual compton scattering beam-spin asymmetries. *Phys. Rev. Lett.*, 100(16):162002, Apr 2008.

[80] I. G. Aznauryan et al. Electroexcitation of nucleon resonances from CLAS data on single pion electroproduction. *Phys. Rev. C*, 80(5):055203, Nov 2009.

[81] M. Battaglieri et al. Photoproduction of $\pi^+\pi^-$ meson pairs on the proton. *Phys. Rev. D*, 80(7):072005, Oct 2009.

[82] X. Qian et al. The extraction of ϕ-N total cross section from d(γ,pK$^+$K$^-$)n. *Physics Letters B*, 680(5):417 – 422, 2009.

[83] R. Nasseripour et al. Photodisintegration of ^{4}He into p + t. *Phys. Rev. C*, 80(4):044603, Oct 2009.

[84] G. Gavalian et al. Beam spin asymmetries in deeply virtual compton scattering (DVCS) with CLAS at 4.8 GeV. *Phys. Rev. C*, 80(3):035206, Sep 2009.

[85] M. Battaglieri et al. Measurement of direct $f_0(980)$ photoproduction on the proton. *Phys. Rev. Lett.*, 102(10):102001, Mar 2009.

[86] J. Lachniet et al. Precise measurement of the neutron magnetic form factor g_M^n in the few-GeV^2 region. *Phys. Rev. Lett.*, 102(19):192001, May 2009.

[87] G. V. Fedotov et al. Electroproduction of p$\pi^+\pi^-$ off protons at $0.2 < q^2 < 0.6$ GeV^2 and $1.3 < w < 1.57$ GeV with the CLAS detector. *Phys. Rev. C*, 79(1):015204, Jan 2009.

[88] M. Osipenko et al. Measurement of semi-inclusive π^+ electroproduction off the proton. *Phys. Rev. D*, 80(3):032004, Aug 2009.

[89] Y. Prok et al. Moments of the spin structure functions and for $0.05 < q2 < 3.0$ GeV^2. *Physics Letters B*, 672(1):12 – 16, 2009.

[90] S. Morrow et al. Exclusive ρ^0 electroproduction on the proton at CLAS. *Euro. Phys. J. A*, 39:5–31, 2009.

[91] M. Nozar et al. Search for the photoexcitation of exotic mesons in the $\pi^+\pi^+\pi^-$ system. *Phys. Rev. Lett.*, 102(10):102002, Mar 2009.

[92] Y. Ilieva et al. Evidence for a backward peak in the $\gamma d \rightarrow \pi^0 d$ cross section near the η threshold. *The European Physical Journal A - Hadrons and Nuclei*, 43:261–267, 2010. 10.1140/epja/i2010-10918-x.

[93] M. E. McCracken et al. Differential cross section and recoil polarization measurements for the $\gamma p \rightarrow K^+\Lambda$ reaction using CLAS at jefferson lab. *Phys. Rev. C*, 81(2):025201, Feb 2010.

[94] S. Anefalos Pereira et al. Differential cross section of $\gamma n \rightarrow K^+\Sigma^-$ on bound neutrons with incident photons from 1.1 to 3.6 GeV. *Physics Letters B*, 688(4-5):289 – 293, 2010.

[95] S. Apsell et al. Ξ resonances in $K^- p \rightarrow \Xi\pi K$ at 2.87 GeV/c.

[96] J. Alitti et al. Strangeness s=-2 baryon resonance. *Phys. Rev. Lett.*, 22:79–82, 1969.

[97] S. F. Biagi et al. Xi* Resonances in Xi- Be Interactions. 2. Properties of Xi (1820) and Xi (1960) in the Lambda anti-K0 and Sigma-0 anti-K0 Channels. *Z. Phys.*, C34:175, 1987.

[98] Charles M. Jenkins et al. Existence of Xi resonances above 2-GeV. *Phys. Rev. Lett.*, 51:951–954, 1983.